

**Design and Synthesis of Covalent Organic
Frameworks for Molecular Adsorption and
Separation**

Wang Ping

Doctor of Philosophy

**Department of Structural Molecular Science
School of Physical Sciences
The Graduate University for Advanced Studies**

September 2017

Tables of Contents

Chapter 1. General Introduction	1
1.1 Covalent Organic Frameworks	2
1.1.1 Design Principles	3
1.1.2 Synthesis Methods	4
1.1.3 Structural Diversity and Control	8
1.2 Hierarchical Design	11
1.2.1 Pore Design	11
1.2.2 Design of the Skeleton	16
1.2.3 Complementary Design of Pores and Skeletons	23
1.3 Scope of This Thesis	27
1.4 References	29
Chapter 2. Design and Synthesis of Microporous Dual-pore Covalent Organic Frameworks bearing Triangular Topology	45
2.1 Introduction	47
2.2 Results and Discussion	48
2.2.1 Triangular COF Design	48
2.2.2 Synthesis and Characterization	49
2.2.3 CO ₂ Uptake	56
2.3 Conclusion	57
2.4 Experimental Sections	57
2.4.1 Methods	57
2.4.2 Synthetic Procedures	58
2.5 References	60
Chapter 3. Sub-angstrom Molecular Discrimination in Crystalline Microporous Covalent Organic Frameworks	65
3.1 Introduction	67
3.2 Results	69
3.2.1 Design and Synthesis	69

3.2.2 Crystallinity and Porosity	72
3.2.3 Selective Adsorption in Solution	75
3.2.4 Column Chromatographic Separation.....	77
3.3 Discussion	78
3.4. Conclusion	83
3.5 Experimental Sections	84
3.5.1 Methods.....	84
3.5.2 Synthetic Procedures.....	87
3.6 References.....	88
Chapter 4. Iodine Capture in Stable, Crystalline, Mesoporous Covalent Organic Frameworks.....	93
4.1 Introduction.....	95
4.2 Results and Discussion	99
4.2.1 COF Synthesis and Characterization	99
4.2.2 Iodine Vapor Capture	103
4.2.3 Cycle Performance.....	106
4.2.4 Iodine Capture from Iodine-Hexane Solution.....	109
4.3 Conclusion	112
4.4 Experimental Sections	112
4.4.1 Methods.....	112
4.4.2 Synthetic Procedures.....	114
4.5 References.....	116
Chapter 5. Ionic Covalent Organic Frameworks: Design of Charged Interface Aligned on 1D Channel Walls and Its Unusual Electric Functions.....	125
5.1 Introduction.....	127
5.2 Results and Discussion	127
5.2.1 COF Synthesis and Characterization	127
5.2.2 CO ₂ Capture	133
5.2.3 Ionic Pollutants Capture.....	135
5.3 Conclusion	139

5.4 Experimental Sections	139
5.4.1 Methods.....	139
5.4.2 Synthetic Procedures.....	142
5.5 References.....	145
Chapter 6. Summary and Perspectives.....	149
List of Publications	153
Acknowledgements	155

Chapter 1. General Introduction

*Covalent Organic Frameworks: A Materials Platform for Structural and
Functional Designs*

Nat. Rev. Mat. 2016, **1**, 16068

Ning Huang, Ping Wang, and Donglin Jiang*

1.1 Covalent Organic Frameworks

The instinct nano-porosity endows porous materials with specific porosities that can barely be provided by non-porous materials. The evolution of material development progress results plentiful porous materials classes, including inorganic, coordinated and pure organic compounds; porous media bearing rigid skeleton and soft dynamic formation; and 2D frameworks and 3D networks.¹⁻⁴ Covalent organic frameworks (COFs) are a class of pure organic polymers constructed by the precise alignments of covalently linked building blocks and the uniform porosity resulted from the skeleton extension.⁵ The robust covalent linkage, ordered skeleton and discrete pore structure make COFs distinct from porous carbons, porous organic polymers, zeolites and metal-organic frameworks and hybrid coordinated or pure organic cages.

Benefited from the reticular chemistry, it is reasonable to design and synthesis COFs of desired pore property and skeleton order according to the topology diagram (Box 1.1). The periodic extension instinct and topology diagrams allow COFs being designed on both primary-order and high-order structure. As a consequence, the deliberate selection of building block geometry and dimension can basically determines the final COF structure, which is usually impossible to be realized by amorphous materials. The topology diagrams characterize reticular chemistry. Basing on these diagrams, building blocks of specific geometry can be precisely interweaved into extended COF lattices by anchoring them as vertices and edges into the crystalline frameworks.

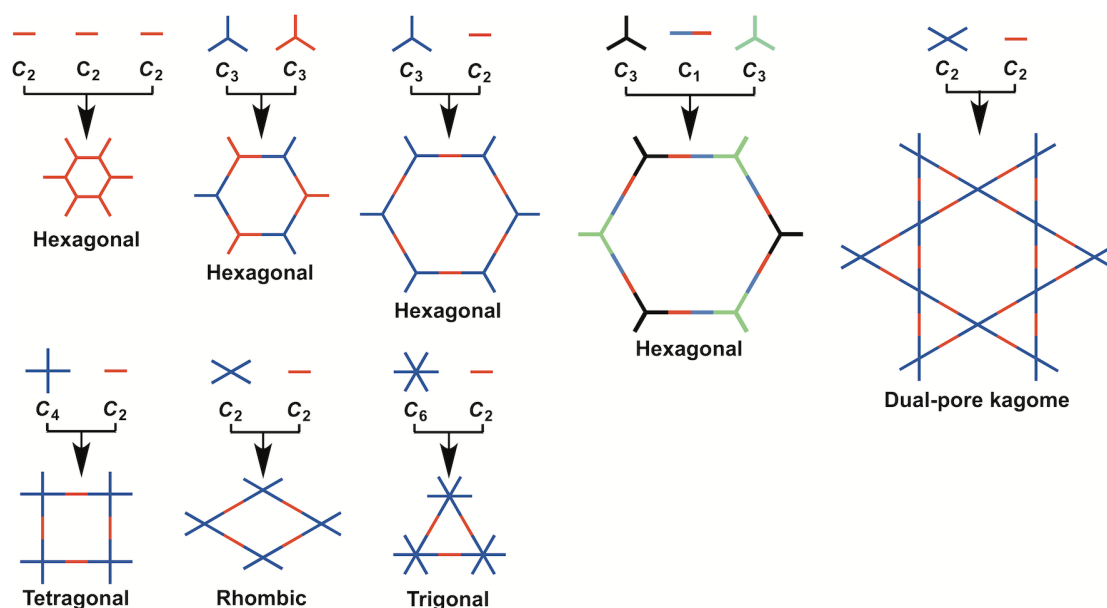
The research of COF is of both chemical interest and physical value. The precise skeleton designability makes COFs pretty attractive to chemistry study. For physical research, the well-organized frameworks offer the opportunity to observe fancy behaviors of excitations, electrons and holes which are induced in the confined space, the specific performance of the confined ions and molecules and the properties of the extended π -systems. As a new material platform, the design of COF can be realized by three approaches: the pore, the skeleton and their syndication. By far, various matter-of-fact applications have been realized by COFs, such as semiconduction,⁷⁻²¹

carbon capture,²²⁻²⁴ proton conduction,²⁵⁻²⁸ luminescence,²⁹⁻³¹ heterogeneous catalysis,³²⁻³⁷ energy storage,³⁸⁻⁴⁰ and energy conversion.⁴¹⁻⁴³ In this chapter, I will specify the structure design strategy of COFs and demonstrate their application achievements.

1.1.1 Design Principles

The reticular chemistry guarantees the building blocks connecting according to the geometry preference and forming specific polygons as showing in the topology diagrams (Box 1.1). Vertices and linkages are basic composites of the polygons; the symmetry of vertices determines the polygon shape and the dimensions of both the vertices and linkages decide the pore size.

Box 1.1 2D COF topology diagrams.¹



According to the symmetry character, vertices can be classified into four groups, namely, C_2 , C_3 , C_4 and C_6 while the linkages are usually of C_2 symmetry. Hexagon built by C_3 -symmetric knots and C_2 -symmetric linkers is the first appeared and most common COF topology.⁴⁴⁻⁶⁵ The hexagonal geometry can also be realized by the self-condensation of C_2 -symmetric building blocks,^{5,8,66,67} or the $C_3 + C_3$ topology scheme.^{45, 68-71} There are no linkers in the $C_3 + C_3$ topology diagram; the C_3 -symmetric unites alternatively occupy the vertex sites.

The rectangular pore geometry is created by the $C_4 + C_2$ topology scheme. The 90° angle between the two vertex arms leads the linkers extending along the x and y axes.⁷²⁻⁷⁸ The rectangular topology is well applied for π -conjugated skeleton formation which hexagonal geometry can barely realize. Because, in comparison with rectangular COFs, the π -cloud delocalization of hexagonal analogues is much smaller. C_2 -symmetric vertices are relatively interesting—when C_2 vertices undergo reaction with C_2 linking units, rhombic^{29, 79, 80} and kagome^{31, 81} topologies are both possible to be yield. Other topology diagrams have no yet reported this phenomenon by far. It is believed that it is the π -structure of the vertical units that determines the final polygon preference.

COFs of large π -density is highly desired but the synthesis remains a challenge. The obstacle has been overcome by the successful development of COFs bearing $C_6 + C_2$ match.^{20, 82, 83} Furthermore, the trigonal topology resulted from the $C_6 + C_2$ combination offers an easy approach to microporous COF synthesis. Currently, COFs of heterogeneous pores are on highly interest. One strategy for multi-pore COFs is introducing one kind vertex and two different kinds linkers together into COF skeletons.⁸⁴ In this way, COFs of three different pores are created. Another approach is the application of asymmetry vertical building blocks.⁸⁵ Basing on this method, dual-pore hexagonal COFs are constructed. Therefore, with the help of topology diagrams, COFs of various pore geometry, pore dimension and skeleton conjugation degree have been constructed by precise molecular design. It is the molecule-level design ability that makes COFs attractive platforms for versatile applications.

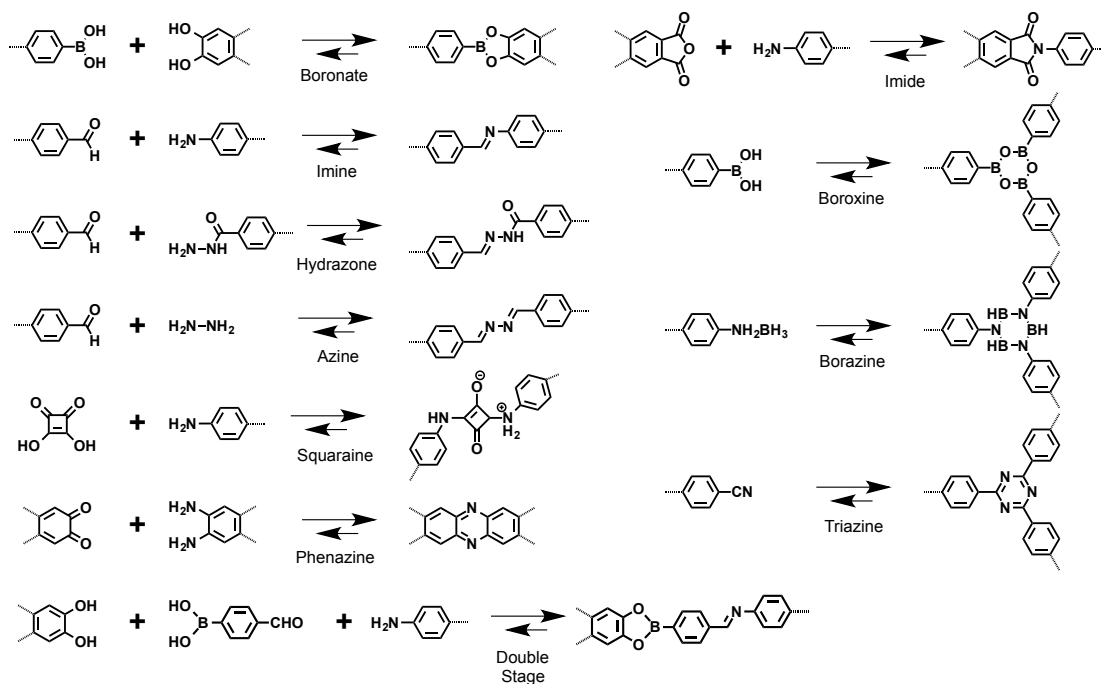
1.1.2 Synthesis Methods

COFs are porous frameworks of primary and high-level skeleton orders. They are synthesized by the condensation reaction between building blocks. The crystallinity requires the condensation reaction with a certain level of reversibility. It is the reversibility that allows the material correcting the structural defects in the polymerization process, resulting the final crystallinity of COFs.

The first-type COFs are constructed by the reversible reaction between boronic acids and catechols and the self-condensation of boronic acids (Box 1.2).^{5, 72, 86} Good

reversibility endows these boronate ester and boroxine linked COFs with usually very high crystallinity; however, all these boron containing COFs suffer a lot from their instability in the appearance of moisture, acids and alcohols.

Box 1.2 Diversity of linkages for the formation of COFs.¹



Condensation between amine and aldehyde in the presence of acetic acid catalyst yields imine-linked COFs.⁸⁷ The imine linkage endows this class of COFs with greatly enhanced chemical stability, making imine COFs stable in water, acids and alcohols. But the lower reversibility results the imine linked COFs much lower crystallinity when compared with that of boronate ester COFs. Replacing amine by hydrazine, COFs bearing hydrazone linkage can be constructed.⁸⁸ It is believed that the hydrogen bonding interaction between the oxygen from alkoxy groups and hydrogen from hydrazone linkages makes contribution to the COF stability. Double-stage strategy combining imine and boronate ester or imine and boroxine linkages in one COF skeleton has been realized by COFs of various topologies.^{89, 90}

Table 1.1 Porosity and stability features of typical COFs.

Linkages	COF	Pore shape	Stability in aqueous solutions			Ref.
			Water	Acid	Basic	
Imine	TpPa-1	Hexagonal	Stable	Stable	Unstable	130
	Tp-Azo COF	Hexagonal	Stable	Stable	Unknown	25
	CTV-COF-1	Hexagonal	Stable	Unknown	Unknown	55
	TpBDH COF	Hexagonal	Stable	Stable	Unknown	56
	TPB-DMTP-COF	Hexagonal	Stable	Stable	Stable	36
	TpPa-Py	Hexagonal	Stable	Stable	Unknown	28
	COF-LZU8	Hexagonal	Stable	Stable	Stable	30
	EB-COF:Br	Hexagonal	Stable	Stable	Unknown	27
	DhaTph COF	Tetragonal	Stable	Stable	Unknown	128
	CuP-TFPh50 COF	Tetragonal	Stable	Stable	Unknown	127
	Py-DHPh COF	Rhombic	Stable	Stable	Unknown	79
	Py-2,2'-BPyPh	Rhombic	Stable	Stable	Unknown	79
	Py-An COF	Rhombic	Stable	Unknown	Unknown	80
HPB-COF	Triangular	Stable	Stable	Stable	20	
Triazine	CTF-1	Hexagonal	Stable	Stable	Stable	66
Phenazine	CS-COF	Hexagonal	Stable	Stable	Stable	13
Imide	PI-COF-2	Hexagonal	Stable	Stable	Stable	54
	PI-COF-3	Hexagonal	Stable	Stable	Stable	54
Hydrazone	TFPT-COF	Hexagonal	Stable	Unknown	Unknown	39
Azine	ACOF-1	Hexagonal	Stable	Unknown	Unknown	22
	COF-JLU 2	Hexagonal	Stable	Unknown	Unknown	142
	N ₃ -COFs	Hexagonal	Stable	Unknown	Unknown	40
	Py-Azine COF	Rhombic	Stable	Stable	Stable	29

Azine-linked COFs are resulted from the reaction between aldehyde and hydrazine. They usually yield microporous COFs with high stability in water, acid and base (Box 1.2 and Table 1.1).²⁹ Phenazine-linked COFs is highlighted by their high π -conjugation and robust stability.¹³ The ring-fusing reaction in acid environment happens between quinones and amines, forming the phenazine linkages. The highly porous imide-linked COFs are synthesized in solvothermal under temperature of 200°C.⁵⁴ At temperature as high as 400°C resulting from molten salts, the self-condensation of aromatic nitriles can be realized and crystalline covalent triazine frameworks (CTFs) are obtained.⁶⁶

A class of squaraine-linked COFs are developed by the reaction between squaric acids and amines (Box 1.2).^{33, 91} The squaraine-linked COFs show unique interlayer structures because of the zwitterions. Ionic COFs are reported as spiroborate-linked ionic COFs and azodioxy linked ionic COFs. The spiroborate linkage is formed by the condensation between diols and trialkyl borates catalyzed by base. In the resulting structure, the negatively charged boron ions locate on the pore walls with lithium or dimethyl ammonium cations as counterions.⁹² The azodioxy linkages are constructed through the self-condensation of protected hydroxylamine and this process requires tetrabutylammonium fluoride working as catalyst.⁹³ Several process intensification methods have been applied for COF synthesis. Zinc chloride salt bath is used to create high temperature for CTF synthesis.^{66, 94, 95} Microwave has been used to improve the COF synthesis efficiency and the quick synthesis approaches of boronate ester, imine and triazine-linked COFs have been realized.⁹⁶⁻⁹⁹

Mechanochemistry approach has been created to produce imine-linked COFs by grinding aldehyde and amine mixture at room temperature in air.¹⁰⁰⁻¹⁰² In comparison with solvothermal protocol, the mechanochemistry is more efficiency but lacks the descent control on system heterogeneity and reaction rate. Reaction rate is the vital parameter to determine the final product porosity and crystallinity. Inspired by the application potential in fields including solar cell, plenty endeavors have been made for single- or multi-layer COF film synthesis. By far, films have been grown on substrates including various kinds of metal,¹⁰³⁻¹⁰⁸ graphene,¹⁰⁹⁻¹¹⁴ indium titanium

oxide (ITO),^{115,116} and silicon⁶⁹ via in situ solution or vapor-phase reactions.^{117, 118} The main challenge of COF film fabrication is the control over the domain structure and surface roughness.

1.1.3 Structural Diversity and Control

The structure diversity of COFs depends not only on the topology diagrams (Box 1.1) and synthetic reactions (Box 1.2), but also on the variedness of the building block. Organic building blocks of different symmetries (C_2 , C_3 , C_4 and C_6), sizes and functions have been explored for COF construction (Figure 1.1). For boronate ester-linked COFs, catechols (Figure 1.1a, blue) and boronic acids (Figure 1.1a, red) of various geometries have been developed. Similarly, more and more aldehydes (Figure 1.1b, purple) and amines (Figure 1.1b, black) with different features are being created to prepare imine-based COFs. The extension of COF skeleton mainly depends on the stretching direction of the vertical units. Therefore, despite the monomer diversity, a certain level of structural rigidity is the basic principle for COF building block design. Various rigid π -units have been introduced into COF skeletons, ranging from simple arenes, heterocyclic molecules to large macrocycle. The development of multi-compound strategy further increases COF structural diversity. By integrating more than two kinds of building blocks into COF lattices, not only the structural complexity is enriched, it is also possible to endow the pores with more complicated environment, making COFs versatile application platforms.

By far, 2D COFs of various topologies have been reported (Box 1.1). Hexagon and tetragon are the most common topologies. The rapid development of building blocks and synthetic strategy makes COFs with rhombic pores, trigonal pores, dual- and triple-pore kagome structures gradually created. On the contrast, the development of 3D COFs remains sluggish. The progress of 3D COF development is largely hindered by the limited tetrahedron-type building blocks. Additionally, the difficulty of crystallinity maintain by pure covalent stretching also contributes to the 3D COF synthesis travail.^{6,87,119-126} Because unlike coordination bonds, covalent bonds are not strictly sterically pinpointed and possess inferior reaction reversibility. Besides, most 3D COFs suffer from low porosity and the shortcoming is mainly resulted from the

complex multifold interdigitation. The descent settlement of complicated interdigitation may promote the 3D COF development.

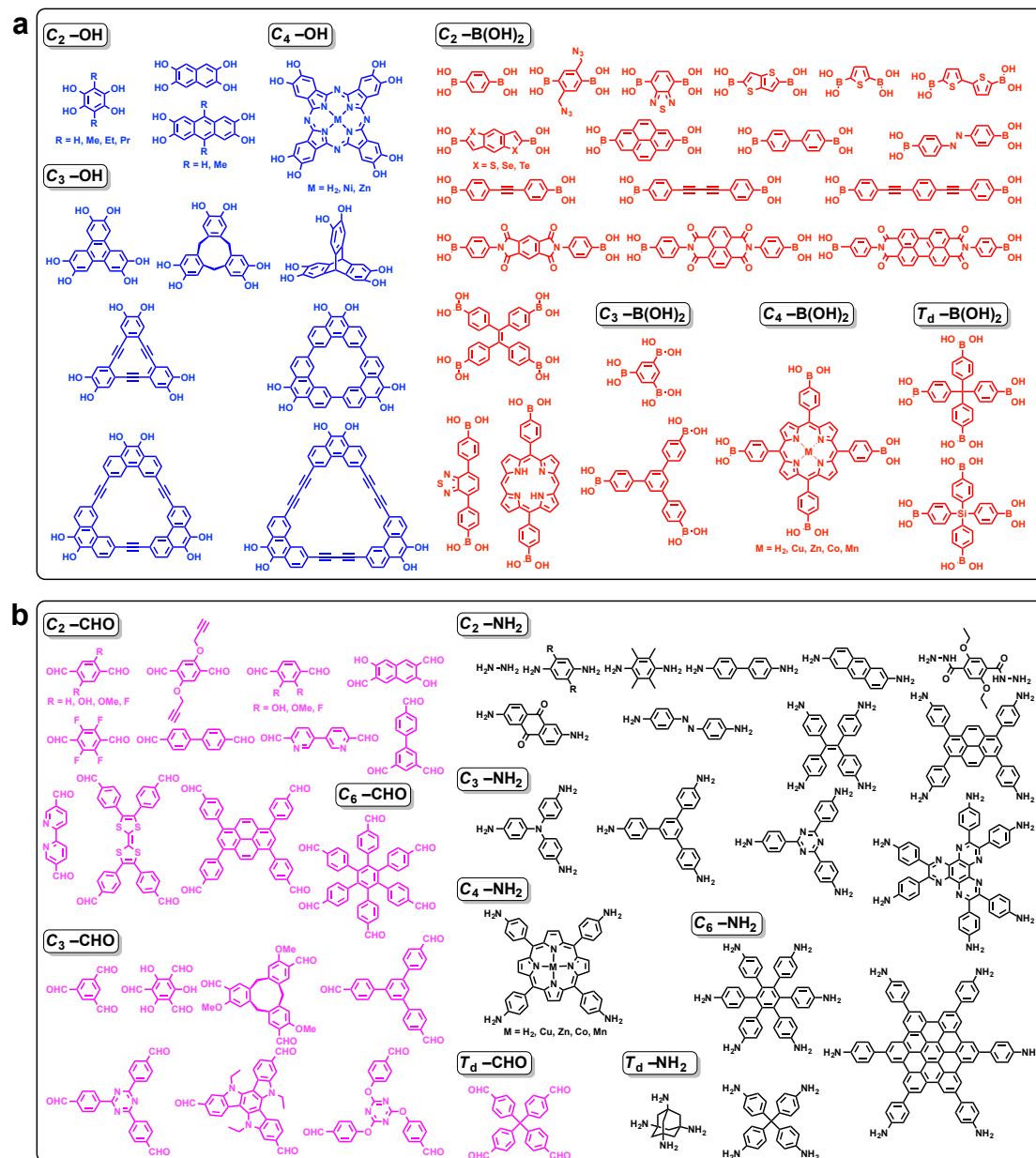


Figure 1.1 Typical building blocks categorized into different symmetries for COFs.¹ (a) Collections of building blocks bearing boronic acid (red) and catechol (blue) moieties to synthesize boronate ester and boroxine-linked COFs. (b) Collections of building blocks bearing aldehyde (purple) and amine (black) units used to form imine-, hydrazone-, azine-, squaraine- and phenazine-linked COFs.

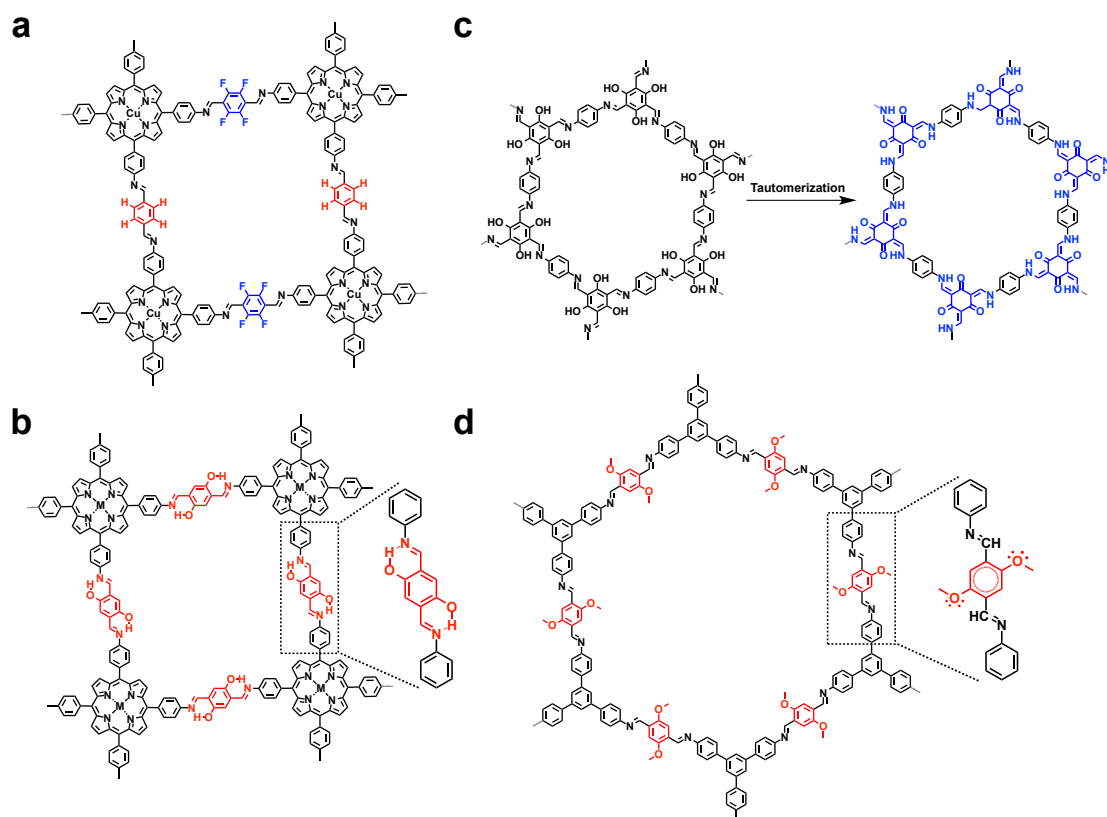


Figure 1.2 Methods to control stability and crystallinity.¹ The quality of COFs including their crystallinity, porosity and stability can be tuned by adjusting the intra- and interlayer interactions. (a) Interlayer complementary π -interactions in CuP-TFPh50% COF.¹²⁷ (b) Intralayer hydrogen-bonding interaction in DhaTph COF (M = H₂) and MP-DHPH COF (M = H₂, Cu and Ni).^{128,129} (c) Tautomerization of enol-to-keto forms in TpPa-1 COF.¹³⁰ (d) Resonance effect in TPB-DMTP-COF.³⁶

The control of COF crystallinity, porosity and stability remains an obstacle to COF synthesis and a fundamental issue of COF study. Researches on this purpose have been widely conducted by introducing supramolecular interactions within or between COF layers (Figure 1.2). It has been proved the crystallinity, porosity and stability of COFs can be improved by integrating complementary π -interactions into the edge units between layers (Figure 1.2a).¹²⁷ Furthermore, the introduction of intralayer hydrogen bonds is also a powerful tool for the enhancement of imine-linked COF qualities including crystallinity, porosity and π -conjugation (Figure 1.2b).^{128,129} The first interlayer approach for COF stability improvement is the enol-to-keto

transition (Figure 1.2c).¹³⁰ Recently the resonance effect to the imine linkages is discovered as a more significant method. It is reported able to soften the linkage polarization and greatly enhance the crystallinity of the resulting COF (Figure 1.2d).³⁶ In comparison of undecorated COFs, the porosity of resonance COF is improved to the theoretical value. Moreover, the resonance COFs are stable against various organic solvents, boiling water, strong base like 14-M aqueous NaOH solution and strong acid including concentrated HCl. The interlayer docking effects is supposed able to enhance the crystallinity of kagome-type COFs.¹³¹ According to the report, the perturbation occurred among layers and within single layer exerts great influence to the COF formation, leading to the crystallinity difference. I summarized the porosities and stabilities of representative COFs in Table 1.1.

1.2 Hierarchical Design

Distinct from other porous materials, the control of building blocks over the aspects including geometry, dimension and function can determine the primary and high level-order of the COF skeleton. COFs are characterized by the regularly aligned π arrays and open nanochannels. The functionalization of COFs can just be fulfilled by the delicate skeleton and pore design. According to functionalization approaches, COF design can be achieved hierarchically on three aspects, namely, pore design, design of the skeleton and complementary design between pore and skeleton.

1.2.1 Pore Design

The pore design strategy can be fully realized by the polygonal shape selection and pore size control. The pore shape can be selected from hexagon, tetragon, trigon, rhomb and kagome while the available pore size covers a wide range from micropore to mesopore. At present, the smallest hexagonal pore is 0.94 nm provided by the azine-linked ACOF-1 (A, azine) whose Brunauer-Emmett-Teller surface area (S_{BET}) is $1176 \text{ m}^2 \text{ g}^{-1}$ (REF.22). The largest mesoporous COFs are the 5.8 nm imine-linked PC-COF (REF. 132; PC = polycationic), 5.3 nm imide-linked PI-COF-3 (REF. 54; PI = polyimide) and 5.3 nm boronate-linked DTP-ANDI-COF (REF. 133), respectively. COFs offering both micropore and mesopore are created by the dual-pore kagome COFs.^{31, 81} Basically, the surface area of 2D COFs ranges from hundreds to 2400 m^2

g^{-1} . The highly porosity makes them promising adsorbents to CO_2 , H_2 , CH_4 and NH_3 (REFS 134-136).

Small pores are preferred for CO_2 capture and adsorption because of the intensive interaction between the pore walls and guest molecules. Researches have proved COFs as promising carbon capture media by reasonable pore size design.^{22-24, 70,82,99,137-144} The azine-linked ACOF-1 (Figure 1.3a; $S_{\text{BET}} = 1176 \text{ m}^2 \text{ g}^{-1}$, pore size = 0.94 nm),²² COF-JLU-2 (Figure 1.3b; $S_{\text{BET}} = 410 \text{ m}^2 \text{ g}^{-1}$, pore size = 0.96 nm),¹⁴² microwave-synthesized TpPa-COF ($S_{\text{BET}} = 725 \text{ m}^2 \text{ g}^{-1}$, pore size = 1.3 nm; Tp = 1,3,5-triformylphloroglucinol, Pa = 4-phenylenediamine)⁹⁹ and HEX-COF-1 (Figure 1.3c; $S_{\text{BET}} = 1200 \text{ m}^2 \text{ g}^{-1}$, pore size = 1.1 nm; HEX = 1,2,3,4,5,6-hexa-(4-formylphenyl)-benzene)⁸² show CO_2 uptake of 17.7, 21.7, 21.8, and 20.0 wt.%, respectively, at 273 K and 1 bar. The small pore confined CO_2 can well interact with the basic azine and amine sites and thus high CO_2 capacities are endowed to these COFs. Similar mechanism is responsible to the outstanding CO_2 capture capability of the fully fluorinated FCTF-1. The polarization induces affinity between the fluorinated frameworks and CO_2 . Thus the CO_2 adsorption capacity of CTF-1 increases from 10.9 wt. % to 24.6 wt. % for the perfluorinated FCTF-1 at 273 K and 1 bar.¹³⁷ Though COFs are supposed as promising carbon capture media, their current performance is rather inferior to that of MOFs. For example, under 1 bar, Ni/DOBDC (DOBDC = 2,5-dioxido-1,4-benzenedicarboxylate) and Mg-MOF-74 exhibit a capacity of 20.5 wt.% and 30.1 wt.% at 298 K, respectively, and $\text{Mg}_2(\text{doppdc})$ (doppdc = 4,4'-dioxido-3,3'-biphenyldicarboxylate) has a capacity of 23.8 wt.% at 313 K (REFS. 145-147). Under high pressure, UiO(bpdc) (UiO, University of Oslo; bpdc = 2,2'-bipyridine-5,5'-dicarboxylate) has a CO_2 uptake capacity of 72.5 wt.% at 20 bar and 303 K (REF. 148). For microporous COFs, effort to enhance the porosity is still on keen desire for the CO_2 uptake capacity improvement. Besides, high-pressure adsorption which has yet been explore by COF adsorbents is worthy of further exploration.

For COFs whose pore size is much beyond the dimension of CO_2 molecules, decorating the pore surface with functional groups of high CO_2 affinity is a practical

method. The control introduction of desirable groups to pore wall with desirable density can be easily realized via pore surface engineering.¹⁴⁹ Through the introduction of reactive azide or ethynyl groups into COF skeletons, the click reactions can be well processed within COF pores and thus functional groups are directly anchored on the COF walls. Further more, decorating COF channels with various specific functional groups via click reaction is also a powerful tool to increase COF diversity. By anchoring alkyl chains, ester, π -moieties, acidic groups and basic units on COF walls, at 273 K and 1bar, the CO₂ capacity of acetic acid-, ethanol-, and ethylamine-functionalized [AcOH]₅₀-H₂P-COF, [EtOH]₅₀-H₂P-COF and [EtNH₂]₅₀-H₂P-COF show enhanced capacities of 11.7, 12.4 and 15.7 wt.%, respectively (Figure 1.3d).²³ As for the non-functionalized porphyrin-based H₂P-COF, its CO₂ capacity is only 6.3 wt.% under same conditions. Notably, pore wall directly functionalization product [COOH]_{100%}-H₂P-COF demonstrates an enhanced CO₂ capacity from 6.3 to 17.4 wt.% at 273 K and 1 bar (Figure 1.3e).²⁴ The significance of carboxyl acid groups is further justified by the perfect cycle performance—it can be cycled more than 10 times without any capacity decay.

COF-LZU-8 (LZU: Lanzhou University) is constructed via functionalization COF channel surface with thioethers. COF-LZU-8 is capable to remove Hg²⁺ selectively from water with uptake capability of 23.6 wt. % (Figure 1.3f).³⁰ The COF-LZU-8 can else be used as Hg²⁺ sensor because its fluorescence will be quenched while the metal ions chelating with thioethers. For catalytic application, COF nanochannels are used as confine space by encapsulating Au and Pd nanoparticles inside (Figure 1.3g).^{34, 150} These metal sites show enhanced catalytic activity in various organic reaction process including Sonogashira reaction, Heck reaction, and C–H bond activation. Catalytic metal ions are also can be loaded within pores facilitated by the selective coordination between ions and bipyridine linkers. Ions loading imine-linked COFs containing ions of Mn and Pd, or Pd and Rh have been reported. Moreover, bimetallic COFs can be yield in this method and have exhibited improved catalytic performance in Heck-epoxidation reaction and addition-oxidation reaction.^{151, 152}

Engineering catalytic sites on pore surface is a creative approach to heterogeneous COF catalyst synthesis. Catalytic COFs synthesized in this method are of well-controlled active site density and structure robustness. The first catalytic COFs produced basing on this approach are the chiral [Pyr]_X-H₂P-COFs (X = 25, 50, 75 and 100%; pyr = pyrrolidine). The COFs are integrated by different ratio of chiral organocatalytic pyrrolidines and serve as heterogeneous catalysts for Michael addition reactions.¹⁵³ The best performed sample is the [Pyr]₂₅-H₂P-COF which completes the reaction within 1 h, demonstrating the importance of the catalytic site density. Further related research is conducted within the large-pore hexagonal COF platform by generating chiral [(S)-Py]_X-TPB-DMTP-COFs (Figure 1.3h; X = 17, 34 and 50%; TPB = 1,3,5-triphenylbenzene; DMTP = dimethoxyterephthaldehyde).³⁶ Benefiting from the high porosity and large pore size, [(S)-Py]_X-TPB-DMTP-COFs show high catalytic performance in asymmetric Michael addition reactions with 100% conversion in 12 h. In this reaction process, an enantiomeric excess as high as 92% is accomplished in water at room temperature. The heterogeneous catalysts demonstrate their generality by the broad range of substrates. By far, [(S)-Py]_X-TPB-DMTP-COFs are the best-performed heterogeneous catalytic COFs by taking activity and enantioselectivity into consideration.

Pore-surface engineering is also a realistic tool for redox-active COF construction. Redox active [TEMPO]_X-NiP-COFs are constructed by anchoring organic radical species 2,2,6,6-tetramethyl-1-piperidinyloxy (TEMPO) on the pore walls of NiP-COFs (Figure 3i; X = 50% and 100%).⁴³ Benefiting from the redox reactions of TEMPO radicals, the redox inactive NiP-COFs are transformed to redox active [TEMPO]₁₀₀-NiP-COF and [TEMPO]₅₀-NiP-COF. At the current density of 100 mA g⁻¹, [TEMPO]₁₀₀-NiP-COF and [TEMPO]₅₀-NiP-COF demonstrate capacitance of 167 and 124 F g⁻¹, separately. Both radical decorated COFs present excellent stable cycle performance by working for 100 cycles showing no capacitance loss. The [TEMPO]_X-NiP-COFs pioneer the exploration of porous radical materials and their performance as energy storage material is superior to those of metal ion-based redox active MOF.¹⁵⁴⁻¹⁵⁷

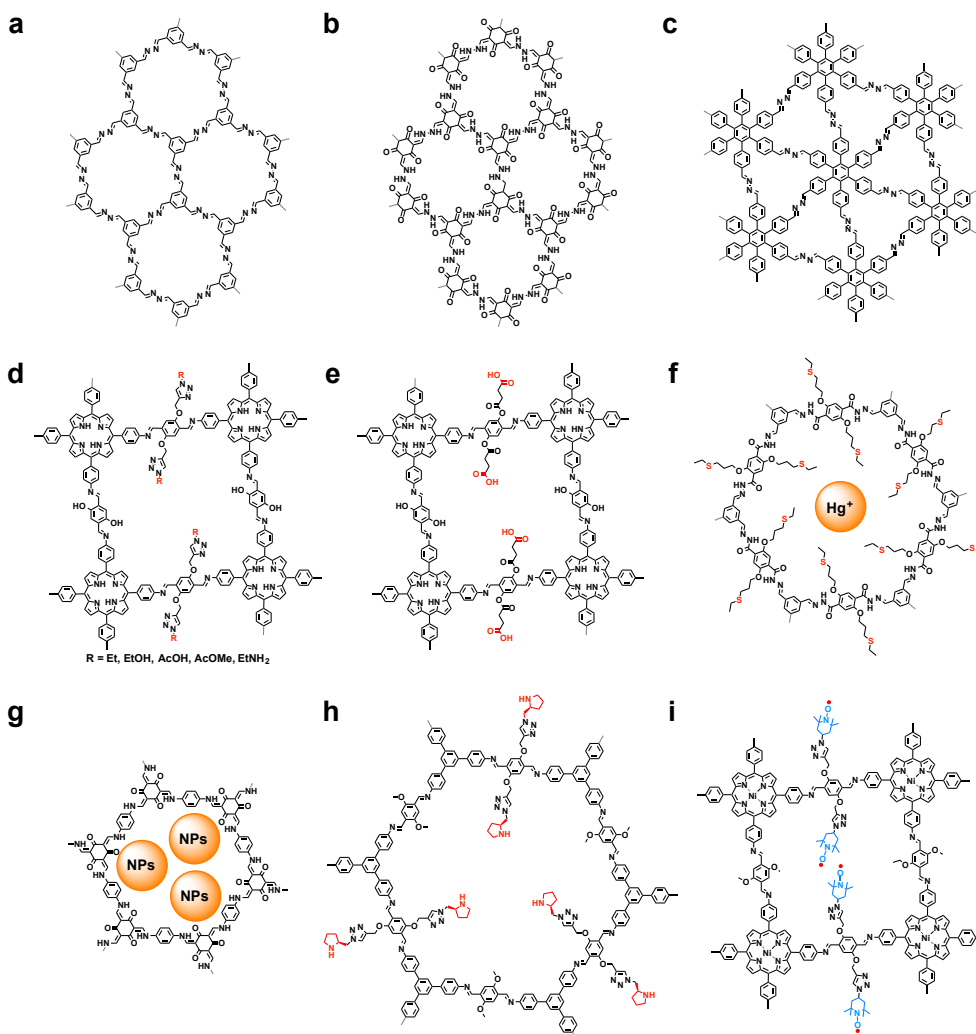


Figure 1.3 Pore design in COFs.¹ (a) Carbon dioxide capture by ACOF.²² (b) Carbon dioxide capture by COF-JUL-2.¹⁴² (c) Carbon dioxide capture by HEX-COF.⁸² (d) Carbon dioxide capture by [R]_x-H₂P-COFs (R = Et, EtOH, AcOH, AcOMe, and EtNH₂; X = 25, 50, 75 and 100%) based on surface engineering with different functional groups.²³ (e) Carbon dioxide capture by [COOH]_x-H₂P-COFs (X = 25, 50, 75 and 100%) via direct channel-wall functionalization with carboxylic acid units.²⁴ (f) Selective Hg²⁺ detection and facile removal by thioether-decorated COF-LZU8.³⁰ (g) Heterogeneous catalysis by using TpPa-1 COF encapsulated with metal (Au or Pd) nanoparticle.³⁴ (h) Asymmetric heterogeneous catalyst using chiral [(S)-Py]_x-TPB-DMTP-COFs (X = 17, 34 and 50%) upon pore-surface engineering with (S)-pyrrolidine active sites.³⁶ (i) Capacitive energy storage using radical [TEMPO]_x-NiP-COFs (X= 50 and 100%) through surface engineering with organic radicals.⁴³

Attempts of using COFs as platforms of lithium–sulfur batteries have been made. Sulfur is impregnated into CTF-1 nanochannels and the final sulfur loading content of the hybrid is determined as 34%.¹⁵⁸ During the electrochemical reaction process, S₈ is efficiently trapped within COF pores and both the capacity and cycle performance are thus improved. At current density of 0.1C, the hybrid is capable to give capacity of 762 mAh g⁻¹ even after 50 charge-discharge cycles. Similar endeavor is performed within the mesoporous Azo-COF. The sulfur content of Azo-COF–sulfur systems is a little higher as 39 wt.% and better cycle performance of keeping a stable capacitance as high as 741 mAh g⁻¹ after 100 cycles is reported.¹⁵⁹ Basing on the survey of different sulfur-lithium battery electrode materials, the capacity of porous carbon and graphene at the same current rate ranges from 124 to 840 mAh g⁻¹.¹⁶⁰ Therefore, on the aspect of capacity, the COF-sulfur systems rank the top level among the various research systems.

1.2.2 Design of the Skeleton

Skeleton design is another well-developed approach for COF functionalization. The precise arranged building blocks within COF skeletons are separated by periodic pore space. Units of different functions including luminescence, π -clouds, catalytic and redox activates have been integrated into COFs. The order and periodic space provided by COF endow these functional fragments with unique characters. The diverse functions and enhanced performance clearly demonstrate that COFs are attractive chemical platforms for new functional material design. Since the π – π stacked layer structure usually results quickly excitation energy dissipation, COFs built upon luminescent units and π -systems basically cannot guarantee luminescent COFs, making the synthesis of luminescent COFs an obstacle. The boronate ester-linked TP-COF (Figure 1.4a)⁷ and boroxine-linked PPy-COF (Figure 1.4b)⁸ are the first two luminescent COFs. Upon excitation of the stacking pyrene units, both TP-COF and PPy-COF exhibit strong blue emission. The azine-linked pyrene-based Py-Azine-COF (Figure 1.4c; Py = pyrene), is another luminescent COFs which giving off yellow emission at 520 nm.²⁹ Facilitated by the lone pairs of electrons of azine units, the Py-Azine-COF can be used as sensor to a series of explosives by the

formation of hydrogen-bond between the azine linkers and guest molecules. The fluorescence of COFs can be efficiently quenched in the appearance of 2,4,6-trinitrophenol and analogues for the sake of photo induced electron transfer.

The precise stacking mood of COFs usually causes the luminescence quenching and makes the development of highly emissive COFs construction difficult. Actually, the stacking between layers results COFs ideal platform for aggregation-induced emission (AIE). AIE materials are freshly discovered and on keen research for highly luminescent material production. Tetraphenylethene (TPE) is a typical AIE-active molecule adopting C_2 symmetry. The condensation between the C_2 -symmetric TPE vertices and C_2 -symmetric linkers yields a TPE-based boronate ester-linked COF (TPE-Ph-COF) (Figure 1.4d).³¹ The TPE-Ph-COF consists of high density of TPE in a kagome-type dual-pore 2D skeleton. The π - π interactions among layers are able to suppress the rotation of the four TPE phenyl arms, resulting strong blue luminescence at 500 nm upon excitation at 390 nm. By taking advantage of the complex formation of the boronate ester linkages and ammonia via Lewis acid–base interaction, the TPE-Ph-COF works as a fluorescence turn-off sensor for ammonia detection. The luminescent TPE-Ph-COF shows high sensitivity by quenching at sub-ppm ammonia level.

The construction of semiconductive COFs keeps an attractive topic when the molecular level ordered structure of COF is considered. The well stacked π -arrays provide pre-organized pathways for high-rate charge-carrier transport.⁷⁻¹² Semiconductive COFs displaying holes,^{9, 74, 75} electrons,¹⁰ and ambipolar charges^{11, 12} transporting properties have been intensively studied for physical research. Moreover, *p*-type semiconductive tetrathiafulvalene (TTF)-based TTF-Ph-COFs (Figure 1.4e) are reported to present conductivity enhancement by a factor of 10^5 after fully iodine doping, displaying final conductivity of 10^{-5} S cm^{-1} . (REFs. 15 and 16) The fabricated TTF-COF films show conductivity of 0.28 S m^{-1} after fully doped by iodine.¹⁷ This value is almost two orders of magnitude higher than that of TTF fibers whose conductivity is 3×10^{-3} S m^{-1} . (REF. 161) PolyTB-based COF (polyTB is the fully conjugated 2D COF based on tpa and bdta, tpa =

2,6-dicabdehyde-4,8-dioctyloxybenzo [1,2-b:3,4-b']dithiophene, bdta = tris (4-aminophenyl) amine) films are fabricated and used as central composite of field-effect transistors. Measurement demonstrates, the mobility of PolyTB-based COF containing transistor is $3 \times 10^{-6} \text{ cm}^2 \text{ V}^{-1} \text{ s}^{-1}$. (REF.21) However, this mobility is much smaller than that of the practical organic transistors ($<10 \text{ cm}^2 \text{ V}^{-1} \text{ s}^{-1}$). (REF.162)

Calculation basing on geometry characters suggests trigonal COFs provide the highest π -unit density compared that with the hexagonal and tetragonal analogues. Experimental studies of COF containing C_6 -symmetric hexabenzene coronene (HBC) and hexaphenylbenzene (HPB) have been conducted.²⁰ The experimental π -unit density of HBC-COF and HPB-COF is 0.13 and 0.25 nm^{-2} , respectively. Facilitated by the high crystallinity and π -unit density, HBC-COF displays a carrier mobility as high as $0.7 \text{ cm}^2 \text{ V}^{-1} \text{ s}^{-1}$ (Figure 1.4f).²⁰ This mobility is comparable to that of HBC-based supramolecular columns.¹⁶³

Donor–acceptor heterojunctions are of highly desired for the development of organic optoelectronics that now suffer a lot from the limited charge separation efficiency. The ordered stacking mode and of building block periodic separation endow COFs with great potential as highly aligned donor–acceptor heterojunctions. This concept is firstly realized by the electron donor–acceptor DCuPc-ADI-COF using phthalocyanines as electron donors and imide as the acceptor counterparts (Figure 1.4g).^{164, 165} In this way, the donor and acceptor units are orderly arranged into COF skeletons via covalent bonds and the eclipsed stacking mood ensures these units segregated as independent bicontinuous columns.¹⁶⁴ Therefore, there are mainly two advantages of the donor- and acceptor-based COFs. First, an exceptional large donor–acceptor interface is provided by the heterojunction COFs. The large interface makes for the rapid transfer and separation of the induced electrons and holes. Second, the periodic separation of π -unit columns enables the efficient charge collection of both holes and electrons and enhanced separation efficiency can be expected. The above two features can hardly be acquired by any another materials. Benefited from the unique structure, the DCuPc-ADI-COF accomplishes the light adsorption, electron

transfer and charge separation within only 1.4 ps.¹⁶⁴ The outstanding separation efficiency makes the donor-acceptor COFs ideal candidates as photo-energy conversion media. Additionally, the delocalized cation and anion can be well preserved along the donor and acceptor columns, resulting the lifetime of the charge-separation states of DCuPc-ADI-COF as long as 33 μ s at 230 K. (REF. 165) The lifetime of DCuPc-ADI-COF is much longer than that of phthalocyanine-diimide assemblies whose typical lifetime of charge-separation state of limits only within several ns.¹⁶⁶ To better understand the design principle of donor-acceptor COFs, more detailed researches are made using large-pore DTP-ANDI-COF (Figure 1.4h) and DTP-APyDI-COF. The research results demonstrate the suitable matching between the highest occupied molecular orbital (HOMO) of electron donor and lowest unoccupied molecular orbital (LUMO) of acceptor are vital to the electron transfer quality of the final COFs.¹³³ Notably, the TP-Por-COF (Figure 1.4i) consisting of triphenylene vertices and porphyrin edges is firstly used as photo-active layers in solar cells.¹⁶⁷ Upon radiation, TP-Por-COF can generate radical species by realizing electron transformation from triphenylenes to porphyrins. However, the external quantum efficiency of the TP-Por-COF containing solar cell is less than 1%. The poor practical efficiency is believed resulting from the inferior device configuration.

There is not doubt that integrating catalytic sites directly into COFs skeletons during synthesis process is an efficient approach to create catalytic COF. This design strategy is firstly realized by the 2,3-DhaTph COF (Figure 1.4j; Dha = dihydroxyterephthalaldehyde, Tph = 5,10,15,20-tetrakis(4-aminophenyl)-21H,23H-porphine).³⁵ The catechols act as acidic active sites and porphyrins as the basic sites. The co-existence of both acid and base catalytic units makes the 2,3-DhaTph COF efficient heterogeneous catalyst of cascade reaction, transforming acetal to aldehyde and finally to malononitrile in a one-pot process. The one-pot reaction shows amazing convention of 96% yield within 90 minutes. Another instinct catalytic COF is the Py-An-COF bearing anthracene units on the edges.⁸⁰ The C–H alignment along the 2.4-nm-diameter 1D channels promote Diels–Alder reactions at room temperature by creating C–H \cdots π interactions between

the anthracene building blocks and in-pore reactants. In the appearance of the Py-An-COF, the final conversion can be achieved as 91% in 48 h. The catalytic performance of Py-An-COF is superior to the MOF-1 catalyst which is used for the same reaction.¹⁶⁸ The imine-linked COF-367-Co (Figure 1.4k) bearing porphyrin vertices shows profound catalytic capability in the electrochemical reduction process from CO₂ to CO (REF. 37). With the optimum Co (II) porphyrin content, the COF-367-Co catalyst displays the Faradaic efficiency of 90%, the turnover number as high as 290,000, and the initial turnover frequency of 9,400 h⁻¹ in aqueous phosphate buffer (pH = 7). The data demonstrate the performance of COF-367-Co ranks it as one of the most efficient electrochemical carbon dioxide reduction catalysts.^{169, 170}

COFs are of obvious advantages as energy storage media on the aspect of diffusion intensification, which makes the creation of redox-active COFs extremely attractive. A high quality redox COF can ensure all the active sites aligned in precise order on pore walls. This distribution pattern facilitates the accessibility between the active units and ions from the electrolyte, making for the energy storage capacity and rate performance. The most famous redox-active COF is the DAAQ-TFP COF (Figure 1.4l, TFP = 1,3,5-triformylphloroglucinol) consisting of redox active 2,6-diamioanthraquinone (DAAQ) units. DAAQs undergo reduction and oxidation in sulfuric acid electrolyte at different potential, giving the DAAQ-TFP COF capacitance of $40 \pm 9 \text{ F g}^{-1}$ and cycle stability of 5000 cycles.⁴¹ The redox inactive counterpart, DAB-TFP COF (DAB = 4-diaminobenzene) displays much smaller capacitance of only $15 \pm 6 \text{ F g}^{-1}$ under same conditions. The DAAQ-TFP COF is further fabricated as thin films on gold substrate. The enhanced conductivity resulted from gold substrate endows the DAAQ-TFP COF thin film electrode with capacitance of 3.0 mF cm^{-2} at a current density of 150 mA cm^{-2} while the performance of the COF power electrode is only 0.4 mF cm^{-2} under same conditions (REF. 117). The other example of redox active COF is the DTP-ANDI-COF formed by the boronate ester-linked naphthalene diimides. The two-electron redox reaction of the diimides in the presence of lithium ions offers the COF a capacity of 42 mAh g^{-1} at a current density of 200 mA g^{-1} .⁴² Basing on the measured capacity, the utilization efficiency of

diimides within the DTP-ANDI-COF is about 48%. To enhance electron conductivity, the redox active DTP-ANDI-COF is grown on the surface of carbon nanotubes. At a current density of 200 mA g^{-1} , the hybrid material presents an improved capacity of 67 mAh g^{-1} and an increased active site utilization of 82%. The rate performance of the DTP-ANDI-COF cathode is also promoted by the enhanced electron conductivity after combining with conductive substrates. In comparison with other counterparts including carbon nanotubes hybrid (102 mAh g^{-1} at 0.8 C)¹⁷² and graphene hybrid (120 mAh g^{-1} at 2C)¹⁷³, the COF hybrid offers superior redox site utilization efficiency, cycle stability and high-rate performance. For the hybrid material, the ion transport is facilitated by COF nanochannels and the carbon nanotube wires guarantee the electron conductivity. The synergistic effects originated from both composites offer the hybrid outstanding energy storage performance. In addition, the structural designability also makes for the application of COFs as next-generation energy storage media.

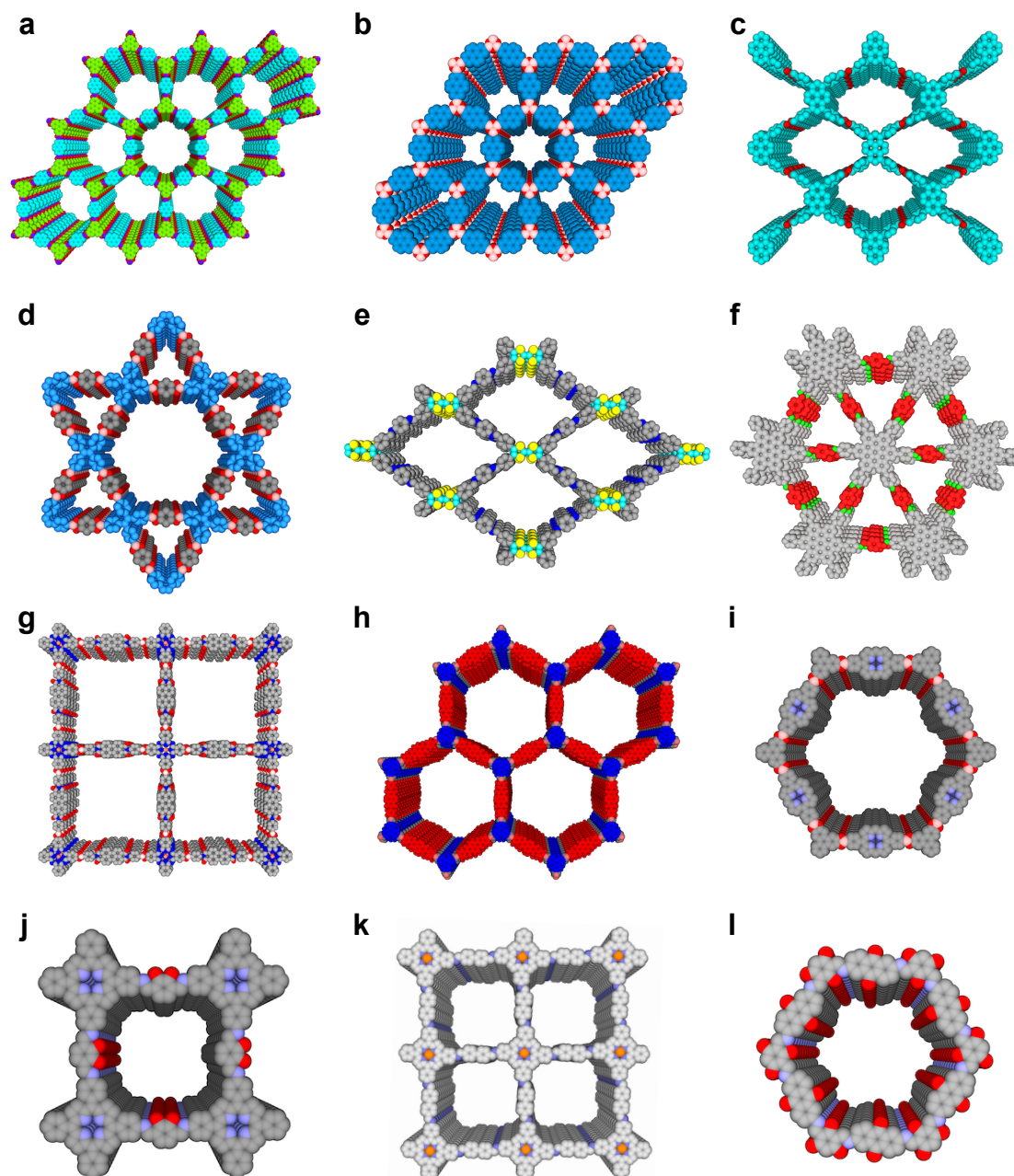


Figure 1.4 Functional exploration of skeletons in COFs.¹ (a) Fluorescent TP-COF.⁷ (b) Fluorescent PPy-COF.⁸ (c) Fluorescent Py-Azine-COF.²⁹ (d) Fluorescent TPE-Ph-COF.³¹ (e) Conductive TTF-Ph-COF.¹⁵⁻¹⁷ (f) Conductive HBC-COF.²⁰ (g) Charge-separated DCuPc-ADI-COF.^{164,165} (h) Charge separated DTP-ANDI-COF.¹³³ (i) Charge-separated TP-Por-COF.¹⁶⁷ (j) Organocatalytic 2,3-DhaTph-COF.³⁵ (k) Electrocatalytic COF-367-Co. (REF.37) (l) Redox-active DAAQ-TEP-COF.⁴¹

1.2.3 Complementary Design of Pores and Skeletons

The synergistic design involving both the latticed π -skeletons and ordered 1D channels provides a bright new strategy for COF functionalization. Recently, COFs have presented application potentials on the aspects including photoenergy conversion, energy storage and proton conduction. All the above applications are realized basing on the suitable combination between COF skeleton and confined pore space.

Other than direct synthesis approach, integrating electron acceptors fullerene into COF pore space proves another method to construct donor-accepter COF system. The hybrid system $[C_{60}]_y$ -ZnPc-COFs ($y = 30, 40$ and 50%) built by anchoring fullerene derivatives into ZnPc-COFs through click reaction is a typical example.¹⁸ Photo induced electron transfer occurs from ZnPc to fullerene once radiated. The efficient charge separation with $[C_{60}]_{30\%}$ -ZnPc-COF is justified by the long charge-separation lifetime as long as 2.66 ms. The lifetime of dyads of zinc phthalocyanine and C_{60} combination is reported as only several ns.¹⁷⁵ Detailed data demonstrates there is a up-going tendency of the radical specie content along with the C_{60} content increases from 30 to 50%. The result suggests the importance of high acceptor density requirement in the hybrid system. Efforts have also been made by uncovalently capture fullerene into COF pores. The first try is conducted via the solution diffusion method between the *p*-type TT-COF (Figure 1.5a) and [6,6]-phenyl- C_{61} -butyric acid methyl ester acceptors.¹⁴ The donor COF is consisted of triphenylene vertices and thieno[3,2-*b*]thiophene edges and the final encapsulation content of [6,6]-phenyl- C_{61} -butyric acid methyl ester is determined as 45 wt.%. 200-nm-thick thin films of the donor-accepter hybrid are fabricated and a charge-separation lifetime of 1070 ps is obtained. Though further measurements related to photovoltaic activity are performed to the films, a power conversion efficiency of 0.053% is far from satisfaction. Similar approach has also been applied to BDT-COF of triphenylene vertices and benzo[1,2-*b*:4,5-*b'*]dithiophene edges. In this COF system, the hole-polaron decay time is determined as 178 ± 4 ps by femtosecond pump-probe transient adsorption measurements.¹¹⁵ After impregnate 25 wt.% fullerenes into phenazine-linked CS-COF (Figure 1.5b) by vacuum sublimation, films of

CS-COF \supset C₆₀ are obtained.¹³ The CS-COF \supset C₆₀ film is introduced as photoactive layer into real solar cells with the composition of Al/poly(methyl methacrylate [PMMA; as a glue]:CS-COF \supset C₆₀/Au. A power conversion efficiency of 0.9% is detected. All the solar cell related results of current researches are far below the performance of conjugated polymer-based solar cells whose efficiency is commonly about 11%. The low current density related to the rough COF partial boundaries is supposed responsible to the poor efficiency of COF systems.¹⁷⁶

The hydrogen evolution performance of COF has been expatiated by the research of hydrazone-linked TFPT-COF (Figure 1.5c)³⁹ and azine-linked N_X-COF (Figure 1.5d; X = 0, 1, 2 and 3)⁴⁰. In the evolution process, the coordination between the platinum nanoparticles and COFs is required in the appearance of sacrificial electron donor triethanolamine. Continuous and stable hydrogen off-giving is observed in both COF systems upon irradiation and the releasing rate is 230 $\mu\text{mol h}^{-1} \text{g}^{-1}$ for TFPT-COF and 1703 $\mu\text{mol h}^{-1} \text{g}^{-1}$ for N_X-COF. The performance of N_X-COF is beyond the rate of 720 $\mu\text{mol h}^{-1} \text{g}^{-1}$ for Pt-modified amorphous melon,¹⁷⁷ 840 $\mu\text{mol h}^{-1} \text{g}^{-1}$ for g-C₃N₄,¹⁷⁸ or 864 $\mu\text{mol h}^{-1} \text{g}^{-1}$ for crystalline poly(triazine imide).¹⁷⁷

As the essential part of fuel cells, proton-conduction materials keeps under keen research. The uniform 1D channels are supposed as ideal containers of proton carriers. As a typical proton carrier, phosphoric acid has been introduced into COFs containing azo, pyridine and bipyridine units. The proton transport ability within these COF systems is believed enhanced by the hydrogen bonds between phosphoric acid and COF skeletons. Guided by this strategy, system of Tp-Azo COF (Figure 1.5e) consisted of 1,3,5-triformylphloroglucinol (Tp) and 4,4'-azodianiline (Azo) with 5.4 wt.% phosphoric acid loading is constructed, exhibiting proton conductivities of 9.9×10^{-4} and $6.7 \times 10^{-5} \text{ S cm}^{-1}$ at 60 °C under 98% relative humidity and anhydrous conditions, respectively.²⁵ These performance is inferior in comparison to that of MOF systems whose conductivity is the $5 \times 10^{-2} \text{ S cm}^{-1}$ for Fe-CAT-5 (REF.179) and $4.2 \times 10^{-2} \text{ S cm}^{-1}$ for $([(\text{DMA})_3(\text{SO}_4)_2[\text{Zn}_2(\text{ox})_3])]$ ¹⁸⁰ at 80 °C and 98% relative humidity.

Recently, a better performance is achieved by the phosphoric acid loaded

TpBpy-COF.¹⁷⁴ The TpBpy-COF is constructed by Tp vertices and 2,2'-bipyridine-diamine (Bpy) linkers through mechanochemical synthesis approach. The proton conductivity of TpBpy-COF is 1.4×10^{-2} S cm⁻¹ at 50 °C under anhydrous conditions. Ionic EB-COF:Br (EB = ethidium bromide) with bromide counter ions aligning along channels shows a proton conductivity of 2.82×10^{-6} S cm⁻¹ at 97% relative humidity at room temperature. Replacing bromide counter ions by polyoxometalate H₃PW₁₂O₄₀·nH₂O results a proton conductivity improvement by 1000 times, achieving the final conductivity as high as of 3.32×10^{-3} S cm⁻¹ under the same conditions.²⁷

Previously, mesoporous materials are believed unable to support proton carriers without leaking and are not suitable for practical proton conduction. The belief is challenged by the successful development of a highly stable TPB-DMTP-COF (Figure 1.5f) as proton conductive medium.²⁶ The large porosity of TPB-DMTP-COF allows the encapsulation of organic proton carriers imidazole (im) and triazole (trz) on extremely high level: the loading contents are 155 and 164 wt.% for im and trz, respectively. The proton conductivity of im@TPB-DMTP-COF (@ means loaded in the pores) is 4.37×10^{-3} S cm⁻¹ and of trz@TPB-DMTP-COF is 1.1×10^{-3} S cm⁻¹ at 130 °C, respectively. The proton conductive abilities are 2–4 orders of magnitude of the (((im@(μ_2 -Al₂-OH)(1,4-d.c.))_n MOF (2.2×10^{-5} S cm⁻¹ at 120 °C),¹⁸¹ trz@~~PC~~PCMOF ($2, 3 \times 10^{-4}$ S cm⁻¹ at 130 °C),¹⁸² and nonporous polymers. The outstanding performance originates from the intrinsic high quality of the COF. The large porosity guarantees a high-content loading of proton carriers and the hydrogen-bonding networks within pores facilitate the superior proton conduction.

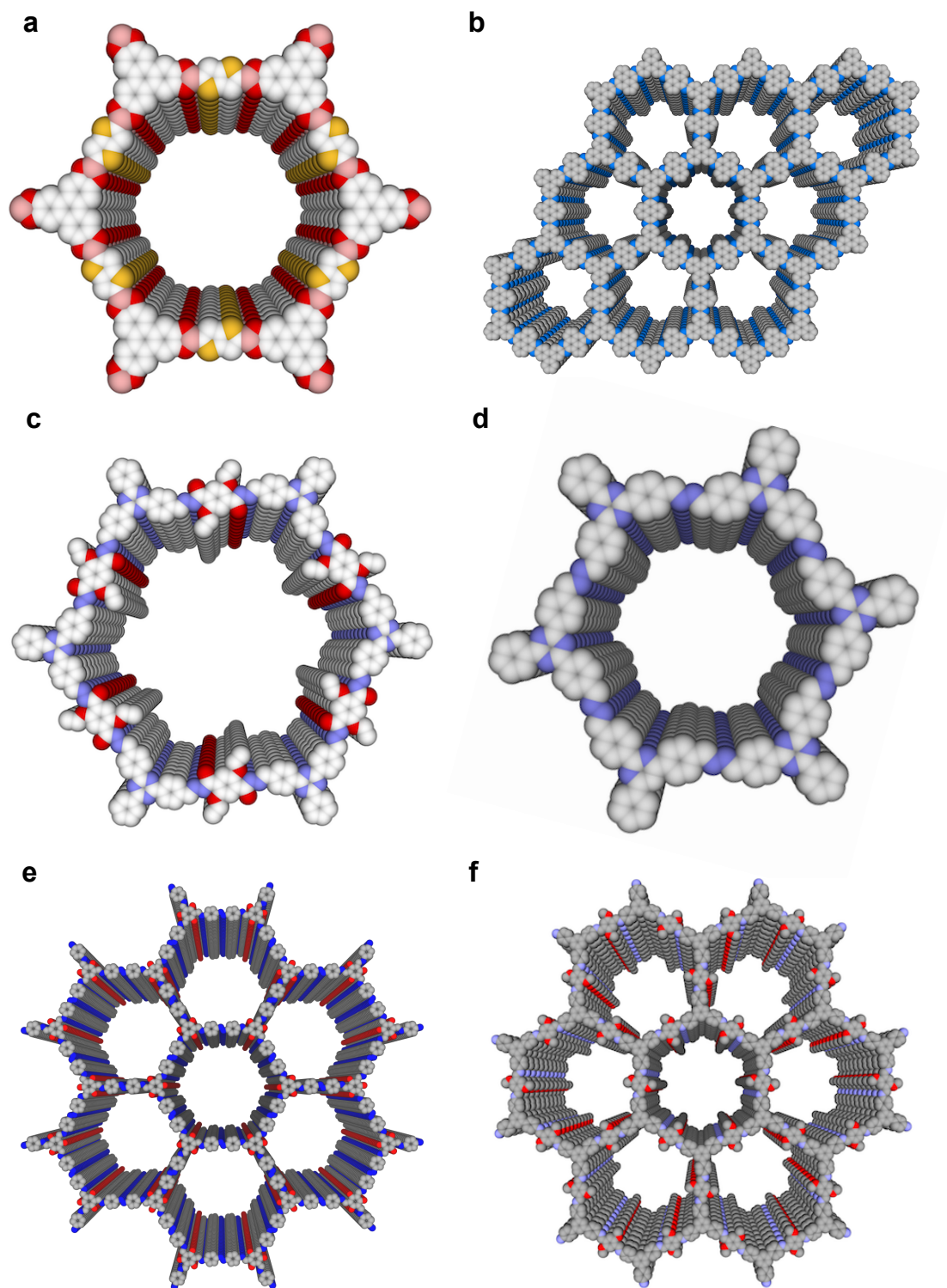


Figure 1.5 Complementary design of pores and skeletons in COFs.¹ (a) Photoconductive TT-COF.¹⁴ (b) Photoconductive CS-COF.¹³ (c) Photocatalytic TFPT-COF.³⁹ (d) Photocatalytic N₃-COF.⁴⁰ (e) Proton-conductive Tp-Azo COF. (f) Proton-conductive TPB-DMTP-COF.²⁶

1.3 Scope of This Thesis

COFs, as novel porous materials, exhibit considerable potential for many applications. However, as a typical highly porous material, COFs have barely been explored as adsorptive separation media. Actually, the discrete pore character, which is impossible to be realized by the commercial amorphous adsorbents, makes COFs ideal platforms as dimension designable adsorbents. The building block alignment, which allows the precise pore environment decoration, facilitates the control on interaction between the COF skeletons and separation compounds. The 1D nanochannels provide space to capture guest compounds and the large interface between COF skeletons and the in-pore foreign molecules, endowing COFs large adsorption capacity and efficiency. In addition, the instinct chemical stability deriving from covalent linkages ensures COFs robust separation media working under various conditions. All these features drive the author to explore the application potential of COFs as designable adsorptive separation media.

This thesis consists of the design, synthesis and separating functional exploration of novel covalent organic frameworks. In Chapter 2, the author described a protocol for the synthesis a series of microporous crystalline COFs using triphenylene derivate aldehyde (HTP-CHO) as a building block and a class of triangular topology COFs were constructed. In Chapter 3, the author described the functionalization of a representative triangular COF as exclusive adsorbent for bulky neutral molecular mixtures. The COF was selected basing on the size match between the pore size and the probe molecule dimension. The COF realized discrimination at sub-angstrom level by including molecules with size of 15.0 Å into the 15.6 Å triangular channels but exclude the counterpart with size of 15.5 Å. The size exclusive adsorption behavior was confirmed by single compound adsorption experiment and energy calculation; the guest molecule accommodation within COF channels was affirmed by gas sorption measurements. In the Chapter 4, the author developed mesoporous materials as a novel porous media for iodine removal and demonstrated the exceptional capture of iodine with crystalline mesoporous COFs. The COFs were designed to have stable imine-linked skeletons, hold mesopores and exhibit large pore

volumes of 1.0 and 1.3 cm³ g⁻¹. Notably, the mesopores were entirely accessible to iodine, leading to a full accommodation of iodine within the nanochannels. Consequently, the COFs exhibited exceptional capacity as high as 6.26 g g⁻¹, which was far superior to the state-of-the-art microporous materials. Moreover, the COFs enabled rapid uptake of iodine with a rate constant of one order of magnitude higher than those of microporous materials.

In the Chapter 5, the author designed and synthesized ionic crystalline porous COFs with positively charged walls that enabled the creation of well aligned yet spatially confined ionic interface. The unconventional reversed AA-stacking mode alternately orientated the cationic centers to both sides of the walls; the ionic interface endowed COFs with unusual electric functions. Because all of the walls were decorated with electric dipoles, the uptake of CO₂ was enhanced by three fold compared to that of the neutral analogue. By virtue of sufficient open space between cations, the ionic interface exhibited exceptional accessibility, efficiency and selectivity in ion exchange to trap anionic pollutants. These findings suggested that construction of ionic interface of COFs offered a new way to the structural and functional designs. In the sixth chapter, the author summarized the work and showed the perspectives.

1.4 References

1. This chapter is from my review paper: Ning Huang, Ping Wang, and Donglin Jiang, Covalent Organic Frameworks: A Materials Platform for Structural and Functional Designs, *Nat. Rev. Mater.* **1**, 16068 (2016).
2. Feng, X., Ding, X. & Jiang, D. Covalent organic frameworks. *Chem. Soc. Rev.* **41**, 6010-6022 (2012).
3. Dogru, M. & Bein, T. On the road towards electroactive covalent organic frameworks. *Chem. Commun.* **50**, 5531-5546 (2014).
4. Waller, P. J., Gándara, F. & Yaghi, O. M. Chemistry of covalent organic frameworks. *Acc. Chem. Res.* **48**, 3053-3063 (2015).
5. Côté, A. P. *et al.* Porous, crystalline, covalent organic frameworks. *Science* **310**, 1166-1170 (2005).
6. El-Kaderi, H. M. *et al.* Designed synthesis of 3D covalent organic frameworks. *Science* **316**, 268-272 (2007).
7. Wan, S., Guo, J., Kim, J., Ihee, H. & Jiang, D. A belt-shaped, blue luminescent, and semiconducting covalent organic framework. *Angew. Chem. Int. Ed.* **48**, 3207-3207 (2009).
8. Wan, S., Guo, J., Kim, J., Ihee, H. & Jiang, D. A photoconductive covalent organic framework: self-condensed arene cubes composed of eclipsed 2D polypyrene sheets for photocurrent generation. *Angew. Chem. Int. Ed.* **48**, 5439-5442 (2009).
9. Wan, S. *et al.* Covalent organic frameworks with high charge carrier mobility. *Chem. Mater.* **23**, 4094-4097 (2011).
10. Ding, X. *et al.* An *n*-channel two-dimensional covalent organic framework. *J. Am. Chem. Soc.* **133**, 14510-14513 (2011).
11. Feng, X. *et al.* High-rate charge-carrier transport in porphyrin covalent organic frameworks: switching from hole to electron to ambipolar conduction. *Angew. Chem. Int. Ed.* **51**, 2618-2622 (2012).
12. Feng, X. *et al.* An ambipolar conducting covalent organic framework with self-sorted and periodic electron donor-acceptor ordering. *Adv. Mater.* **24**,

- 3026-3031 (2012).
13. Guo, J. *et al.* Conjugated organic framework with three-dimensionally ordered stable structure and delocalized π clouds. *Nat. Commun.* **4**, 2736 (2013).
 14. Dogru, M. *et al.* A photoconductive thienothiophene-based covalent organic framework showing charge transfer towards included fullerene. *Angew. Chem. Int. Ed.* **52**, 2920-2924 (2013).
 15. Jin, S. *et al.* Two-dimensional tetrathiafulvalene covalent organic frameworks: towards latticed conductive organic salts. *Chem. Eur. J.* **20**, 14608-14613 (2014).
 16. Ding, H. *et al.* A tetrathiafulvalene-based electroactive covalent organic framework. *Chem. Eur. J.* **20**, 14614-14618 (2014).
 17. Cai, S.-L. *et al.* Tunable electrical conductivity in oriented thin films of tetrathiafulvalene-based covalent organic framework. *Chem. Sci.* **5**, 4693-4700 (2014).
 18. Chen, L. *et al.* Photoelectric covalent organic frameworks: converting open lattices into ordered donor-acceptor heterojunctions. *J. Am. Chem. Soc.* **136**, 9806-9809 (2014).
 19. Duhović, S. & Dincă, M. Synthesis and electrical properties of covalent organic frameworks with heavy chalcogens. *Chem. Mater.* **27**, 5487-5490 (2015).
 20. Dalapati, S. *et al.* Rational design of crystalline supermicroporous covalent organic frameworks with triangular topologies. *Nat. Commun.* **6**, 7786 (2015).
 21. Feldblyum, J. I. *et al.* Few-layer, large-area, 2D covalent organic framework semiconductor thin films. *Chem. Commun.* **51**, 13894-13897 (2015).
 22. Li, Z. *et al.* A 2D azine-linked covalent organic framework for gas storage applications. *Chem. Commun.* **50**, 13825-13828 (2014).
 23. Huang, N., Krishna, R. & Jiang, D. Tailor-made pore surface engineering in covalent organic frameworks: systematic functionalization for performance screening. *J. Am. Chem. Soc.* **137**, 7079-7082 (2015).
 24. Huang, N., Chen, X., Krishna, R. & Jiang, D. Two-dimensional covalent organic frameworks for carbon dioxide capture through channel-wall functionalization. *Angew. Chem. Int. Ed.* **54**, 2986-2990 (2015).

25. Chandra, S. *et al.* Phosphoric acid loaded azo (–N=N–) based covalent organic framework for proton conduction. *J. Am. Chem. Soc.* **136**, 6570-6573 (2014).
26. Xu, H., Tao, S. & Jiang, D. Proton conduction in crystalline and porous covalent organic frameworks. *Nat. Mater.* **15**, 722-727 (2016).
27. Ma, H. *et al.* Cationic covalent organic frameworks: a simple platform of anionic exchange for porosity tuning and proton conduction. *J. Am. Chem. Soc.* **138**, 5897-5903 (2016).
28. Chandra, S. *et al.* Interplaying intrinsic and extrinsic proton conductivities in covalent organic frameworks. *Chem. Mater.* **28**, 1489-1494 (2016).
29. Dalapati, S. *et al.* An azine-linked covalent organic framework. *J. Am. Chem. Soc.* **135**, 17310-17313 (2013).
30. Ding, S.-Y. *et al.* Thioether-based fluorescent covalent organic framework for selective detection and facile removal of mercury(II). *J. Am. Chem. Soc.* **138**, 3031-3037 (2016).
31. Dalapati, S., Jin, E., Addicoat, M., Heine, T. & Jiang, D. Highly emissive covalent organic frameworks. *J. Am. Chem. Soc.* **138**, 5797-5800 (2016).
32. Ding, S.-Y. *et al.* Construction of covalent organic framework for catalysis: Pd/COF-LZU1 in Suzuki-Miyaura coupling reaction. *J. Am. Chem. Soc.* **133**, 19816-19822 (2011).
33. Nagai, A. *et al.* A squaraine-linked mesoporous covalent organic framework. *Angew. Chem. Int. Ed.* **52**, 3770-3774 (2013).
34. Pachfule, P. *et al.* Multifunctional and robust covalent organic framework-nanoparticle hybrids. *J. Mater. Chem. A* **2**, 7944-7952 (2014).
35. Shinde, D. B., Kandambeth, S., Pachfule, P., Kumar, R. R. & Banerjee, R. Bifunctional covalent organic frameworks with two dimensional organocatalytic micropores. *Chem. Commun.* **51**, 310-313 (2015).
36. Xu, H., Gao, J. & Jiang, D. Stable, crystalline, porous, covalent organic frameworks as a platform for chiral organocatalysts. *Nat. Chem.* **7**, 905-912 (2015).
37. Lin, S. *et al.* Covalent organic frameworks comprising cobalt porphyrins for

- catalytic CO₂ reduction in water. *Science* **349**, 1208-1213 (2015).
38. Thote, J. *et al.* A covalent organic framework-cadmium sulfide hybrid as a prototype photocatalyst for visible-light-driven hydrogen production. *Chem. Eur. J.* **20**, 15961-15965 (2014).
 39. Stegbauer, L., Schwinghammer, K. & Lotsch, B. V. A hydrazone-based covalent organic framework for photocatalytic hydrogen production. *Chem. Sci.* **5**, 2789-2793 (2014).
 40. Vyas, V. S. *et al.* A tunable azine covalent organic framework platform for visible light-induced hydrogen generation. *Nat. Commun.* **6**, 8508 (2015).
 41. DeBlase, C. R., Silberstein, K. E., Truong, T.-T., Abruña, H. D. & Dichtel, W. R. β -ketoenamine-linked covalent organic frameworks capable of pseudocapacitive energy storage. *J. Am. Chem. Soc.* **135**, 16821-16824 (2013).
 42. Xu, F. *et al.* Electrochemically active, crystalline, mesoporous covalent organic frameworks on carbon nanotubes for synergistic lithium-ion battery energy storage. *Sci. Rep.* **5**, 8225 (2015).
 43. Xu, F. *et al.* Radical covalent organic frameworks: a general strategy to immobilize open-accessible polyradicals for high-performance capacitive energy storage. *Angew. Chem. Int. Ed.* **54**, 6814-6818 (2015).
 44. Tilford, R. W., Gemmill, W. R., zur Loye, H.-C. & Lavigne, J. J. Facile synthesis of a highly crystalline, covalently linked porous boronate network. *Chem. Mater.* **18**, 5296-5301 (2006).
 45. Côté, A. P., El-Kaderi, H. M., Furukawa, H., Hunt, J. R. & Yaghi, O. M. Reticular synthesis of microporous and mesoporous 2D covalent organic frameworks. *J. Am. Chem. Soc.* **129**, 12914-12915 (2007).
 46. Tilford, R. W., Mugavero, S. J., Pellechia, P. J. & Lavigne, J. J. Tailoring microporosity in covalent organic frameworks. *Adv. Mater.* **20**, 2741-2746 (2008).
 47. Dogru, M., Sonnauer, A., Gavryushin, A., Knochel, P. & Bein, T. A covalent organic framework with 4 nm open pores. *Chem. Commun.* **47**, 1707-1709 (2011).

48. Spitler, E. L. *et al.* A 2D covalent organic framework with 4.7-nm pores and insight into its interlayer stacking. *J. Am. Chem. Soc.* **133**, 19416-19421 (2011).
49. Yu, J.-T., Chen, Z., Sun, J., Huang, Z.-T. & Zheng, Q.-Y. Cyclotricatechylene based porous crystalline material: synthesis and applications in gas storage. *J. Mater. Chem.* **22**, 5369-5373 (2012).
50. Kahveci, Z., Islamoglu, T., Shar, G. A., Ding, R. & El-Kaderi, H. M. Targeted synthesis of a mesoporous triptycene-derived covalent organic framework. *CrystEngComm* **15**, 1524-1527 (2013).
51. Bertrand, G. H. V., Michaelis, V. K., Ong, T.-C., Griffin, R. G. & Dincă, M. Thiophene-based covalent organic frameworks. *Proc. Natl. Acad. Sci.* **110**, 4923-4928 (2013).
52. Feng, X., Dong, Y. & Jiang, D. Star-shaped two-dimensional covalent organic frameworks. *CrystEngComm* **15**, 1508-1511 (2013).
53. Zhang, J. *et al.* A novel azobenzene covalent organic framework. *CrystEngComm* **16**, 6547-6551 (2014).
54. Fang, Q. *et al.* Designed synthesis of large-pore crystalline polyimide covalent organic frameworks. *Nat. Commun.* **5**, 4503 (2014).
55. Song, J.-R., Sun, J., Liu, J., Huang, Z.-T. & Zheng, Q.-Y. Thermally/hydrolytically stable covalent organic frameworks from a rigid macrocyclic host. *Chem. Commun.* **50**, 788-791 (2014).
56. Das, G. *et al.* Chemical sensing in two dimensional porous covalent organic nanosheets. *Chem. Sci.* **6**, 3931-3939 (2015).
57. Yang, H. *et al.* Mesoporous 2D covalent organic frameworks based on shape-persistent arylene-ethynylene macrocycles. *Chem. Sci.* **6**, 4049-4053 (2015).
58. Biswal, B. P. *et al.* Pore surface engineering in porous, chemically stable covalent organic frameworks for water adsorption. *J. Mater. Chem. A* **3**, 23664-23669 (2015).
59. Baldwin, L. A., Crowe, J. W., Shannon, M. D., Jaroniec, C. P. & McGrier, P. L. 2D covalent organic frameworks with alternating triangular and hexagonal pores.

- Chem. Mater.* **27**, 6169-6172 (2015).
60. Lin, S. *et al.* A triazine-based covalent organic framework/palladium hybrid for one-pot silicon-based cross-coupling of silanes and aryl iodides. *RSC Adv.* **5**, 41017-41024 (2015).
 61. Li, Z., Zhang, Y., Xia, H., Mu, Y. & Liu, X. A robust and luminescent covalent organic framework as a highly sensitive and selective sensor for the detection of Cu²⁺ ions. *Chem. Commun.* **52**, 6613-6616 (2016).
 62. Zhen, J. *et al.* Preparation of a series of aCTV-based covalent organic frameworks and substituent effects on their properties. *CrystEngComm* **18**, 1039-1045 (2016).
 63. Lohse, M. S. *et al.* Sequential pore wall modification in a covalent organic framework for application in lactic acid adsorption. *Chem. Mater.* **28**, 626-631 (2016).
 64. Li, Z.-J., Ding, S.-Y., Xue, H.-D., Cao, W. & Wang, W. Synthesis of –C=N– linked covalent organic frameworks via the direct condensation of acetals and amines. *Chem. Commun.* **52**, 7217-7220 (2016).
 65. Lohse, M. S. *et al.* From benzodithiophene to diethoxy-benzodithiophene covalent organic frameworks-structural investigations. *CrystEngComm* **18**, 4295-4302 (2016).
 66. Kuhn, P., Antonietti, M. & Thomas, A. Porous, covalent triazine-based frameworks prepared by ionothermal synthesis. *Angew. Chem. Int. Ed.* **47**, 3450-3453 (2008).
 67. Jackson, K. T., Reich, T. E. & El-Kaderi, H. M. Targeted synthesis of a porous borazine-linked covalent organic framework. *Chem. Commun.* **48**, 8823-8825 (2012).
 68. Xie, Y.-F., Ding, S.-Y., Liu, J.-M., Wang, W. & Zheng, Q.-Y. Triazatruxene based covalent organic framework and its quick-response fluorescence-on nature towards electron rich arenes. *J. Mater. Chem. C* **3**, 10066-10069 (2015).
 69. de la Peña Ruigómez, A. *et al.* Direct on-surface patterning of a crystalline laminar covalent organic framework synthesized at room temperature. *Chem. Eur.*

- J.* **21**, 10666-10670 (2015).
70. Kaleeswaran, D., Vishnoi, P. & Murugavel, R. [3+3] Imine and β -ketoenamine tethered fluorescent covalent-organic frameworks for CO₂ uptake and nitroaromatic sensing. *J. Mater. Chem. C* **3**, 7159-7171 (2015).
 71. Xu, L. *et al.* Highly crystalline covalent organic frameworks from flexible building blocks. *Chem. Commun.* **52**, 4706-4709 (2016).
 72. Spitler, E. L. & Dichtel, W. R. Lewis acid-catalyzed formation of two-dimensional phthalocyanine covalent organic frameworks. *Chem. Commun.* **47**, 1979-1981 (2011).
 73. Feng, X., Chen, L., Dong, Y. & Jing, D. Porphyrin-based two-dimensional covalent organic frameworks: synchronized synthetic control of macroscopic structures and pore parameters. *Chem. Commun.* **47**, 1979-1981 (2011).
 74. Ding, X. *et al.* Synthesis of metallophthalocyanine covalent organic frameworks that exhibit high carrier mobility and photoconductivity. *Angew. Chem. Int. Ed.* **50**, 1289-1293 (2011).
 75. Ding, X. *et al.* Conducting metallophthalocyanine 2D covalent organic frameworks: the role of central metals in controlling π -electronic functions. *Chem. Commun.* **48**, 8952-8954 (2012).
 76. Neti, V. S. P. K. *et al.* Synthesis of a phthalocyanine 2D covalent organic framework. *CrystEngComm* **15**, 7157-7160 (2013).
 77. Neti, V. S. P. K., Wu, X., Deng, S. & Echegoyen, L. Synthesis of a phthalocyanine and porphyrin 2D covalent organic framework. *CrystEngComm* **15**, 6892-6895 (2013).
 78. Chen, X., Gao, J. & Jiang, D. Designed synthesis of porphyrin-based two-dimensional covalent organic frameworks with highly ordered structures. *Chem. Lett.* **44**, 1257-1259 (2015).
 79. Chen, X. *et al.* Towards covalent organic frameworks with designable and aligned open docking sites. *Chem. Commun.* **50**, 6161-6163 (2014).
 80. Wu, Y., Xu, H., Chen, X., Gao, J. & Jiang, D. A π -electronic covalent organic framework catalyst: π -walls as catalytic beds for Diels-Alder reactions under

- ambient conditions. *Chem. Commun.* **51**, 10096-10098 (2015).
81. Zhou, T.-Y., Xu, S.-Q., Wen, Q., Pang, Z.-F. & Zhao, X. One-step construction of two different kinds of pores in a 2D covalent organic framework. *J. Am. Chem. Soc.* **136**, 15885-15888 (2014).
82. Alahakoon, S. B. *et al.* An azine-linked hexaphenylbenzene based covalent organic framework. *Chem. Commun.* **52**, 2843-2845 (2016).
83. Xu, S.-Q., Zhan, T.-G., Wen, Q., Pang, Z.-F. & Zhao, X. Diversity of covalent organic frameworks (COFs): a 2D COF containing two kinds of triangular micropores of different sizes. *ACS Macro Lett.* **5**, 99-102 (2016).
84. Pang, Z.-F. *et al.* Construction of covalent organic frameworks bearing three different kinds of pores through the heterostructural mixed linker strategy. *J. Am. Chem. Soc.* **138**, 4710-4713 (2016).
85. Zhu, Y., Wan, S., Jin, Y. & Zhang, W. Desymmetrized vertex design for the synthesis of covalent organic frameworks with periodically heterogeneous pore structures. *J. Am. Chem. Soc.* **137**, 13772-13775 (2015).
86. Spitler, E. L., Giovino, M. R., White, S. L. & Dichtel, W. R. A mechanistic study of Lewis acid-catalyzed covalent organic framework formation. *Chem. Sci.* **2**, 1588-1593 (2011).
87. Uribe-Romo, F. J. *et al.* A crystalline imine-linked 3-D porous covalent organic framework. *J. Am. Chem. Soc.* **131**, 4570-4571 (2009).
88. Uribe-Romo, F. J., Doonan, C. J., Furukawa, H., Oisaki, K. & Yaghi, O. M. Crystalline covalent organic frameworks with hydrazone linkages. *J. Am. Chem. Soc.* **133**, 11478-11481 (2011).
89. Zeng, Y. *et al.* Covalent organic frameworks formed with two types of covalent bonds based on orthogonal reactions. *J. Am. Chem. Soc.* **137**, 1020-1023 (2015).
90. Chen, X. *et al.* Designed synthesis of double-stage two-dimensional covalent organic frameworks. *Sci. Rep.* **5**, 14650 (2015).
91. Zhang, W., Jiang, P., Wang, Y., Zhang, J. & Zhang, P. Bottom-up approach to engineer two covalent porphyrinic frameworks as effective catalysts for selective oxidation. *Catal. Sci. Technol.* **5**, 101-104 (2015).

92. Du, Y. *et al.* Ionic covalent organic frameworks with spiroborate linkage. *Angew. Chem. Int. Ed.* **55**, 1737-1741 (2016).
93. Nath, B. *et al.* A new azodioxy-linked porphyrin-based semiconductive covalent organic framework with I₂ doping-enhanced photoconductivity. *CrystEngComm* **18**, 4259-4263 (2016).
94. Bojdys, M. J., Jeromenok, J., Thomas, A. & Antonietti, M. Rational extension of the family of layered, covalent, triazine-based frameworks with regular porosity. *Adv. Mater.* **22**, 2202-2205 (2010).
95. Kuecken, S., Schmidt, J., Zhi, L. & Thomas, A. Conversion of amorphous polymer networks to covalent organic frameworks under ionothermal conditions: a facile synthesis route for covalent triazine frameworks. *J. Mater. Chem. A* **3**, 24422-24427 (2015).
96. Campbell, N. L., Clowes, R., Ritchie, L. K. & Cooper, A. I. Rapid microwave synthesis and purification of porous covalent organic frameworks. *Chem. Mater.* **21**, 204-206 (2009).
97. Ren, S. *et al.* Porous, fluorescent, covalent triazine-based frameworks via room-temperature and microwave-assisted synthesis. *Adv. Mater.* **24**, 2357-2361 (2012).
98. Dogru, M. *et al.* Facile synthesis of a mesoporous benzothiadiazole-COF based on a transesterification process. *CrystEngComm* **15**, 1500-1502 (2013).
99. Wei, H. *et al.* The microwave-assisted solvothermal synthesis of a crystalline two-dimensional covalent organic framework with high CO₂ capacity. *Chem. Commun.* **51**, 12178-12181 (2015).
100. Biswal, B. P. *et al.* Mechanochemical synthesis of chemically stable isorecticular covalent organic frameworks. *J. Am. Chem. Soc.* **135**, 5328-5331 (2013).
101. Chandra, S. *et al.* Chemically stable multilayered covalent organic nanosheets from covalent organic frameworks via mechanical delamination. *J. Am. Chem. Soc.* **135**, 17853-17861 (2013).
102. Das, G., Balaji Shinde, D., Kandambeth, S., Biswal, B. P. & Banerjee, R. Mechanosynthesis of imine, β -ketoenamine, and hydrogen-bonded imine-linked

- covalent organic frameworks using liquid-assisted grinding. *Chem. Commun.* **50**, 12615-12618 (2014).
103. Blunt, M. O., Russell, J. C., Champness, N. R. & Beton, P. H. Templating molecular adsorption using a covalent organic framework. *Chem. Commun.* **46**, 7157-7159 (2010).
104. Marele, A. C. *et al.* Formation of a surface covalent organic framework based on polyester condensation. *Chem. Commun.* **48**, 6779-6781 (2012).
105. Gutzler, R. *et al.* Surface mediated synthesis of 2D covalent organic frameworks: 1,3,5-tris(4-bromophenyl)benzene on graphite (001), Cu (111), and Ag (110). *Chem. Commun.* 4456-4458 (2009).
106. Zwaneveld, N. A. A. *et al.* Organized formation of 2D extended covalent organic frameworks at surfaces. *J. Am. Chem. Soc.* **130**, 6678-6679 (2008).
107. Larrea, C. R. & Baddeley, C. J. Fabrication of a high-quality, porous, surface-confined covalent organic framework on a reactive metal surface. *ChemPhysChem* **17**, 971-975 (2016).
108. Hao, D. *et al.* Fabrication of a COF-5 membrane on a functionalized α -Al₂O₃ ceramic support using a microwave irradiation method. *Chem. Commun.* **50**, 1462-1464 (2014).
109. Colson, J. W. *et al.* Oriented 2D covalent organic framework thin films on single-layer graphene. *Science* **332**, 228-231 (2011).
110. Spitler, E. L. *et al.* Lattice expansion of highly oriented 2D phthalocyanine covalent organic framework films. *Angew. Chem. Int. Ed.* **51**, 2623-2627 (2012).
111. Xu, L. *et al.* Surface-confined single-layer covalent organic framework on single-layer graphene grown on copper foil. *Angew. Chem. Int. Ed.* **53**, 9564-9568 (2014).
112. Zha, Z. *et al.* 3D graphene functionalized by covalent organic framework thin film as capacitive electrode in alkaline media. *ACS Appl. Mater. Interfaces* **7**, 17837-17843 (2015).
113. Colson, J. W., Mann, J. A., DeBlase, C. R. & Dichtel, W. R. Patterned growth of oriented 2D covalent organic framework thin films on single-layer graphene. *J.*

- Polym. Sci., Part A: Polym. Chem.* **53**, 378-384 (2015).
114. Yue, J.-Y., Liu, X.-H., Sun, B. & Wang, D. The on-surface synthesis of imine-based covalent organic frameworks with non-aromatic linkage. *Chem. Commun.* **51**, 14318-14321 (2015).
115. Medina, D. D. *et al.* Oriented thin films of a benzodithiophene covalent organic framework. *ACS Nano* **8**, 4042-4052 (2014).
116. Gou, X. *et al.* Preparation and engineering of oriented 2D covalent organic framework thin films. *RSC Adv.* **6**, 39198-39203 (2016).
117. Chen, Y. *et al.* Surface growth of highly oriented covalent organic framework thin film with enhanced photoresponse speed. *RSC Adv.* **5**, 92573-92576 (2015).
118. Medina, D. D. *et al.* Room temperature synthesis of covalent-organic framework films through vapor-assisted conversion. *J. Am. Chem. Soc.* **137**, 1016-1019 (2015).
119. Hunt, J. R., Doonan, C. J., LeVangie, J. D., Côté, A. P. & Yaghi, O. M. Reticular synthesis of covalent organic borosilicate frameworks. *J. Am. Chem. Soc.* **130**, 11872-11873 (2008).
120. Bunck, D. N. & Dichtel, W. R. Internal functionalization of three-dimensional covalent organic frameworks. *Angew. Chem. Int. Ed.* **51**, 1885-1889 (2012).
121. Bunck, D. N. & Dichtel, W. R. Postsynthetic functionalization of 3D covalent organic frameworks. *Chem. Commun.* **49**, 2457-2459 (2013).
122. Zhang, Y.-B. *et al.* Single-crystal structure of a covalent organic framework. *J. Am. Chem. Soc.* **135**, 16336-16339 (2013).
123. Fang, Q. *et al.* 3D Microporous base-functionalized covalent organic frameworks for size-selective catalysis. *Angew. Chem. Int. Ed.* **53**, 2878-2882 (2014).
124. Fang, Q. *et al.* 3D porous crystalline polyimide covalent organic frameworks for drug delivery. *J. Am. Chem. Soc.* **137**, 8352-8355 (2015).
125. Lin, G., Ding, H., Yuan, D., Wang, B. & Wang, C. A pyrene-based, fluorescent three-dimensional covalent organic framework. *J. Am. Chem. Soc.* **138**, 3302-3305 (2016).
126. Liu, Y. *et al.* Weaving of organic threads into a crystalline covalent organic

- framework. *Science* **351**, 365-369 (2016).
127. Chen, X., Addicoat, M., Irle, S., Nagai, A. & Jiang, D. Control of crystallinity and porosity of covalent organic frameworks by managing interlayer interactions based on self-complementary π -electronic force. *J. Am. Chem. Soc.* **135**, 546-549 (2013).
128. Kandambeth, S. *et al.* Enhancement of chemical stability and crystallinity in porphyrin-containing covalent organic frameworks by intramolecular hydrogen bonds. *Angew. Chem. Int. Ed.* **52**, 13052-13056 (2013).
129. Chen, X. *et al.* Locking covalent organic frameworks with hydrogen bonds: general and remarkable effects on crystalline structure, physical properties, and photochemical activity. *J. Am. Chem. Soc.* **137**, 3241-3247 (2015).
130. Kandambeth, S. *et al.* Construction of crystalline 2D covalent organic frameworks with remarkable chemical (acid/base) stability via a combined reversible and irreversible route. *J. Am. Chem. Soc.* **134**, 19524-19527 (2012).
131. Ascherl, L. *et al.* Molecular docking sites designed for the generation of highly crystalline covalent organic frameworks. *Nat. Chem.* **8**, 310-316 (2016).
132. Yu, S.-B. *et al.* A polycationic covalent organic framework: a robust adsorbent for anionic dye pollutants. *Polym. Chem.* **7**, 3392-3397 (2016).
133. Jin, S. *et al.* Large pore donor-acceptor covalent organic frameworks. *Chem. Sci.* **4**, 4505-4511 (2013).
134. Furukawa, H. & Yaghi, O. M. Storage of hydrogen, methane, and carbon dioxide in highly porous covalent organic frameworks for clean energy applications. *J. Am. Chem. Soc.* **131**, 8875-8883 (2009).
135. Doonan, C. J., Tranchemontagne, D. J., Glover, T. G., Hunt, J. R. & Yaghi, O. M. Exceptional ammonia uptake by a covalent organic framework. *Nat. Chem.* **2**, 235-238 (2010).
136. Zeng, Y., Zou, R. & Zhao, Y. Covalent organic frameworks for CO₂ capture. *Adv. Mater.* **28**, 2855-2873 (2016).
137. Zhao, Y., Yao, K. X., Teng, B., Zhang, T. & Han, Y. A perfluorinated covalent triazine-based framework for highly selective and water-tolerant CO₂ capture.

- Energy Environ. Sci.* **6**, 3684-3692 (2013).
138. Rabbani, M. G. *et al.* A 2D mesoporous imine-linked covalent organic framework for high pressure gas storage applications. *Chem. Eur. J.* **19**, 3324-3328 (2013).
139. Gomes, R., Bhanja, P. & Bhaumik, A. A triazine-based covalent organic polymer for efficient CO₂ adsorption. *Chem. Commun.* **51**, 10050-10053 (2015).
140. Gao, Q. *et al.* Synthesis of microporous nitrogen-rich covalent-organic framework and its application in CO₂ capture. *Chin. J. Chem.* **33**, 90-94 (2015).
141. Zhao, S. *et al.* Channel-wall functionalization in covalent organic frameworks for the enhancement of CO₂ uptake and CO₂/N₂ selectivity. *RSC Adv.* **6**, 38774-38781 (2016).
142. Li, Z. *et al.* An azine-linked covalent organic framework: synthesis, characterization and efficient gas storage. *Chem. Eur. J.* **21**, 12079-12084 (2015).
143. Gomes, R. & Bhaumik, A. A new triazine functionalized luminescent covalent organic framework for nitroaromatic sensing and CO₂ storage. *RSC Adv.* **6**, 28047-28054 (2016).
144. Dong, B. *et al.* Immobilization of ionic liquids to covalent organic frameworks for catalyzing the formylation of amines with CO₂ and phenylsilane. *Chem. Commun.* **52**, 7082-7085 (2016).
145. Li, L., Yang, J., Li, J., Chen, Y. & Li, J. Separation of CO₂/CH₄ and CH₄/N₂ mixtures by M/DOBDC: A detailed dynamic comparison with MIL-100(Cr) and activated carbon. *Micropor. Mesopor. Mater.* **198**, 236-246 (2014).
146. Wu, X. *et al.* Microwave synthesis and characterization of MOF-74 (M = Ni, Mg) for gas separation. *Micropor. Mesopor. Mater.* **180**, 114-122 (2013).
147. Mason, J. A. *et al.* Application of a high-throughput analyzer in evaluating solid adsorbents for post-combustion carbon capture via multicomponent adsorption of CO₂, N₂, and H₂O. *J. Am. Chem. Soc.* **137**, 4787-4803 (2015).
148. Li, L. *et al.* High gas storage capacities and stepwise adsorption in a UiO type metal-organic framework incorporating Lewis basic bipyridyl sites. *Chem. Commun.* **50**, 2304-2307 (2014).

149. Nagai, A. *et al.* Pore surface engineering in covalent organic frameworks. *Nat. Commun.* **2**, 536 (2011).
150. Pachfule, P., Kandambeth, S., Diaz Diaz, D. & Banerjee, R. Highly stable covalent organic framework-Au nanoparticles hybrids for enhanced activity for nitrophenol reduction. *Chem. Commun.* **50**, 3169-3172 (2014).
151. Leng, W., Ge, R., Dong, B., Wang, C. & Gao, Y. Bimetallic docked covalent organic frameworks with high catalytic performance towards tandem reactions. *RSC Adv.* **6**, 37403-37406 (2016).
152. Leng, W. *et al.* Sophisticated design of covalent organic frameworks with controllable bimetallic docking for a cascade reaction. *Chem Eur. J.* **22**, 9087-9091 (2016).
153. Xu, H. *et al.* Catalytic covalent organic frameworks via pore surface engineering. *Chem. Commun.* **50**, 1292-1294 (2014).
154. Diaz, R., Orcajo, M. G., Botas, J. A., Callega, G & Palma, J. Co8-MOF-5 as electrode for supercapacitores. *Mater. Letter.* **68**, 126-128 (2012).
155. Li, S. -L., & Xu, Q. Metal-organic frameworks as platforms for clean energy. *Energy Environ. Sci.* **6**, 1656-1683, (2013).
156. Lee, D. Y., *et al.* Unusual energy storage and charge retention in Co-based metal-organic frameworks. *Micropor. Mesopor. Mater.* **153**, 163-165, (2012)
157. Gao, Y. *et al.* Synthesis of nickel oxalate/zeolitic imidazolate framework-67 (NiC₂O₄/ZIF-67) as a supercapacitor electrode. *New J. Chem.* **39**, 94097 (2015).
158. Liao, H., Ding, H., Li, B., Ai, X. & Wang, C. Covalent-organic frameworks: potential host materials for sulfur impregnation in lithium-sulfur batteries. *J. Mater. Chem. A* **2**, 8854-8858 (2014).
159. Yang, X. *et al.* Sulfur impregnated in a mesoporous covalent organic framework for high performance lithium-sulfur batteries. *RSC Adv.* **5**, 86137-86143 (2015).
160. Sun, M. -H. *et al.* Applications of hierarchically structural porous materials from energy storage and conversion, catalysis, photocatalysis, adsorption, separation, and sensing to biomedicine. *Chem. Soc. Rev.* **45**, 3479-3563 (2016).
161. Kitamura, T. *et al.* Electroactive superamolecular self-assembled fibers comprise

- of doped tetrathiafulvalene-based gelators. *J. Am. Chem. Soc.* **127**, 554-567 (2011).
162. Braga, D. & Horowitz, G. High-performance organic field-effect transistors. *Adv. Mater.* **21**, 1473-1486 (2009).
163. Pisula, W., Feng, X. & Müllen, K. Charge-carrier transporting graphene-type molecules. *Chem. Mater.* **23**, 554-567 (2011).
164. Jin, S. *et al.* Charge dynamics in a donor-acceptor covalent organic framework with periodically ordered bicontinuous heterojunctions. *Angew. Chem. Int. Ed.* **52**, 2017-2021 (2013).
165. Jin, S. *et al.* Charge dynamics in a donor-acceptor covalent organic framework with periodically ordered bicontinuous heterojunctions. *Angew. Chem. Int. Ed.* **52**, 2017-2021 (2013).
166. Jimenez, A., J., Calderon, R. M. K., Rodriguez-Morgade, M. S., Cudi, D. M. & Yorres, T. Synthesis, characterization and photophysical properties of a melamin-mediated hydrogen-bonded phthalogyanine-perylene diimide assembly. *Chem. Sci.* **4**, 1064-1074 (2013).
167. Calik, M. *et al.* Extraction of photogenerated electrons and holes from a covalent organic framework integrated heterojunction. *J. Am. Chem. Soc.* **136**, 17802-17807 (2014).
168. Gole, B., Bar, A. K., Mallick, A., Banerjee, R. & Mukherjee, P. S. An electron rich porous extended framework as a heterogeneous catalyst for Diels-Alder Reactions. *Chem. Commun.* **49**, 7439-7441 (2013).
169. Costentin, C., Robert, M. & Saveant, J. -M. Catalysis of the electrochemical reduction of carbon dioxide. *Chem. Soc. Rev.* **42**, 2423-2436 (2013).
170. Kumar, *et al.* Photochemical and photoelectrochemical reduction of CO₂. *Annu. Rev. Phys. Chem.* **63**, 541-569 (2012).
171. DeBlase, C. R. *et al.* Rapid and efficient redox processes within 2D covalent organic framework thin films. *ACS Nano* **9**, 3178-3183 (2015).
172. Wu, H. *et al.* Flexible and binder-free organic cathode for high-performance lithium-ion batteries. *Adv. Mater.* **26**, 3338-3343 (2014).

173. Meng, Y., Wu, H., Zhang, Y. & Wei, Z. A flexible electrode based on a three-dimensional graphene network-supported polyimide for lithium-ion batteries. *J. Mater. Chem. A* **2**, 10842-10846 (2014).
174. Shinde, D. B. *et al.* A mechanochemically synthesized covalent organic framework as a proton-conducting solid electrolyte. *J. Mater. Chem. A* **4**, 2682-2690 (2016).
175. Guldi, D. M., Fouloumis, A., Vazquez, P. & Torres, T. Charge-transfer stages in strongly coupled phthalocyanine fullerene ensembles. *Chem. Commun.* **2002**, 2056-2057 (2002).
176. Green, M. A., Emery, K., Hishikawa, Y., Warta, W. & Dunlop, E. D. Solar cell efficiency tables (version 47). *Prog. Photovolt. Res. Appl.* **24**, 3-11.
177. Schwinghammer, K. *et al.* Triazine-based carbon nitrides for visible-light-driven hydrogen evolution. *Angew. Chem. Int. Ed.* **52**, 2435-2439 (2013).
178. Zhang, J. *et al.* Synthesis of a carbon nitride structure for visible-light catalysis by copolymerization. *Angew. Chem. Int. Ed.* **49**, 441-444 (2010).
179. Nguyen, N. T. T. *et al.* Three-dimensional metal catecholate frameworks and their ultrahigh proton conductivity. *J. Am. Chem. Soc.* **137**, 15394-15397 (2015).
180. Yoon, M. *et al.* High and highly anisotropic proton conductivity in organic molecular porous materials. *Angew. Chem. Int. Ed.* **50**, 7870-7873 (2011).
181. Bureekaew, S. *et al.* One-dimensional imidazole aggregate in aluminium porous coordination polymers with high proton conductivity. *Nat. Mater.* **8**, 831-836 (2009).
182. Hurd, J. A. *et al.* Anhydrous proton conduction at 150 °C in a crystalline metal organic framework. *Nat. Chem.* **1**, 705-710 (2009).

**Chapter 2. Design and Synthesis of
Microporous Dual-pore Covalent Organic
Frameworks bearing Triangular Topology**

Abstract Covalent organic frameworks (COFs) are a special kind of porous materials made from pure organic building blocks which integrate atomically into ordered porous crystalline frameworks. Design strategy is an important prerequisite for the successfully synthesis of COFs. Here I report the synthesis of a series of dual-pore triangular COFs by deliberate monomer structural design. C_3 symmetry vertex units bearing six reaction active sites were successfully interweaved into COF framework skeletons and three dual-pore structure COFs were created. Generality of the design strategy was confirmed by systematically extending the linker length. The three resulting COFs present high crystallinity, discrete dual-pore distribution and the largest surface area among all the existed triangular COFs.

2.1 Introduction

Covalent organic frameworks (COFs) are a special kind of polymers made from pure organic building blocks. These building blocks together create periodically nanochannel space through crystallization while these building blocks are covalently linked into various organic polygons.^{1, 2} The periodically ordered π -array skeletons and aligned one-dimensional nanochannels are the typical characters of two-dimensional (2D) COFs.³⁻⁹ These crystalline porous polymers are quite attractive for applications in various fields, including catalysis,¹⁰⁻¹³ gas adsorption,¹⁴⁻¹⁶ sensing,^{17, 18} proton conduction,¹⁹⁻²¹ and energy conversion and storage.²²⁻²⁷ Pore dimension plays vital role for COF application. Microporous materials have long been preferred as gas adsorbents for the facilitated interaction within the pore space. Recently, triangular topology design is reported as optimum approach for microporous COF synthesis.³² However, it still remains a great challenge to develop a general strategy for the synthesis of high-crystalline and high-porosity triangular COFs.^{33, 34}

The building block chemical activity and structural rigidity and the neighbor layer stacking state determine COF properties including crystallinity and porosity.^{1, 2} By taking advantage of the building block geometry, I designed a six-armed building block basing on the highly conjugated triphenylene. The delicate designed building block is expected able to endow the resulting COFs with good crystallinity because the strong π - π interaction between triphenylene fragments can facilitate the stacking between layers. Considering of the C_3 symmetry of triphenylene, a dual-pore structure can be expected from the resulting COFs. Recently the development of multi-pore COFs becomes a hot topic in COF field.²⁸⁻³⁰ The multi-pore nature is supposed able to endow COFs with versatile functions by allowing the stepwise pore decoration and diffusion path design.³¹ Thus, it is reasonable to expect the multi-pore COFs working as a mini chemical factory after multi-function decoration.

Herein, I report the design and synthesis of a series of microporous COF bearing triangular topology and dual-pore structure. The present strategy demonstrates that the

triangular topology with the right choice of the linkage length endows the COFs with high crystallinity and microporous pore structure, making them descent carbon dioxide uptake media.

2.2 Results and Discussion

2.2.1 Triangular COF Design

The strategy for preparing triangular COFs starts from the design of a six-arm building block, HTP-CHO, which is synthesized by substituting triphenylene with six phenyl aldehyde groups. HTP-CHO is a typical C_3 symmetry building block since the six arms of HTP-CHO are not identical. Thus dual-pore structure is resulted in the COFs constructed by HTP-CHO knots and diamine linkers (Figure 2.1a).

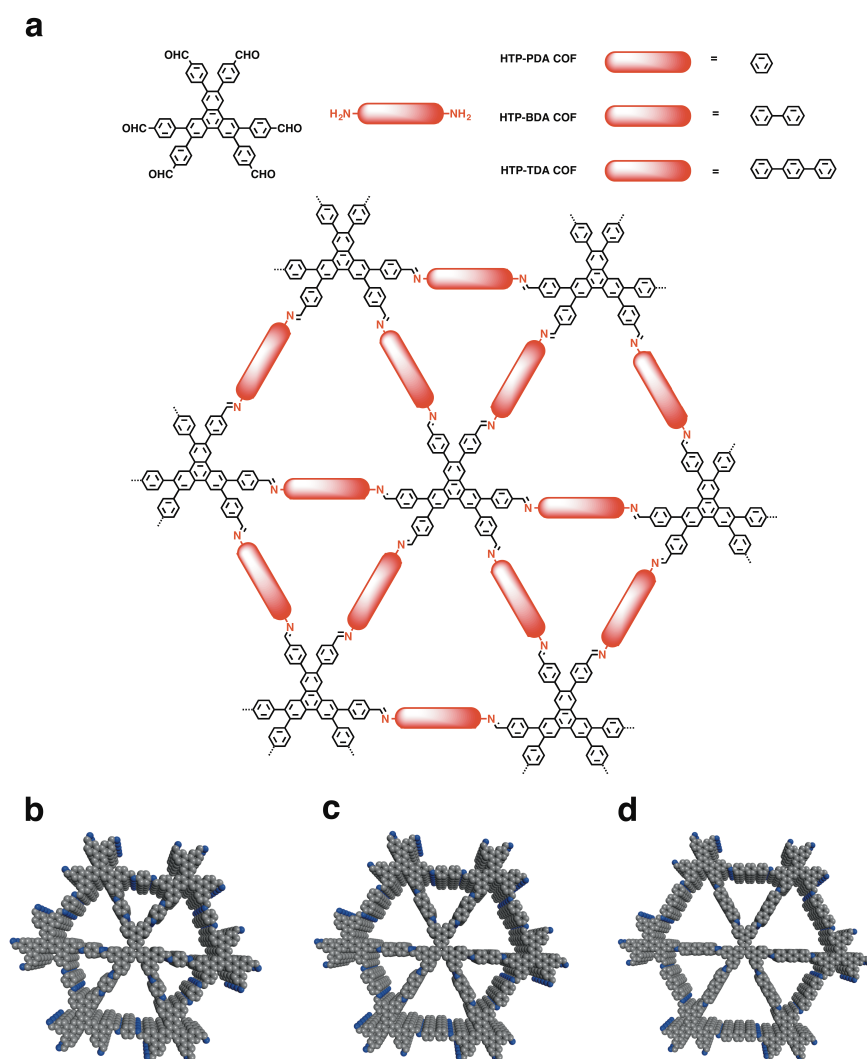


Figure 2.1 Schematic representation of the synthesis of HTP-COFs. (a) Synthesis of

HTP-COF through the condensation of HTP-CHO (black) and diamines (red). Schematic structure of (b) HTP-PDA COF, (c) HTP-BDA COF and (d) HTP-TDA COF. Blue, N; gray, C; hydrogen is omitted for clarity.

The generality of the COF design strategy is confirmed by increasing the linear edge length systematically. I chose three diamines 1,4-phenylenediamine (PDA), 1,1'-biphenyl-4,4'-diamine (BDA) and 1,1':4',1''-terphenyl-4,4''-diamine (TDA), to take condensation reaction with HTP-CHO. Benefit from facilitated π - π interaction between layers by the triphenylene planar structure and the triangular geometry, a series of COFs with discrete but slightly different pores are created, yielding HTP-PDA COF, HTP-BDA COF, and HTP-TDA COF, respectively (Figures 2.1 b-d).

2.2.2 Synthesis and Characterization

The triangular COFs were synthesized solvothermally by dispersing HTP-CHO and diamine partners in the mixture solution of *o*-DCB: *n*-BuOH: 6M aqueous acetic acid = 5:5:1(v:v:v) and heating at 120 °C for 5 days. The resulting HTP-COFs were obtained as yellow powders with isolated yield of 80% for HTP-PDA COF, 84% for HTP-BDA COF and 80% for HTP-TDA COF.

Fourier transform infrared spectra presented the absorption at 1620 cm^{-1} for all the three COFs, which corresponded to the vibration band of C=N group (Figure 2.2). All the three COFs adopted aggregated particle morphologies as revealed by field-emission scanning electron microscopy (FE-SEM) (Figure 2.3). This HTP-COF series presented high thermal stability justified by thermogravimetric analysis (TGA) up to 500 °C (Figure 2.4).

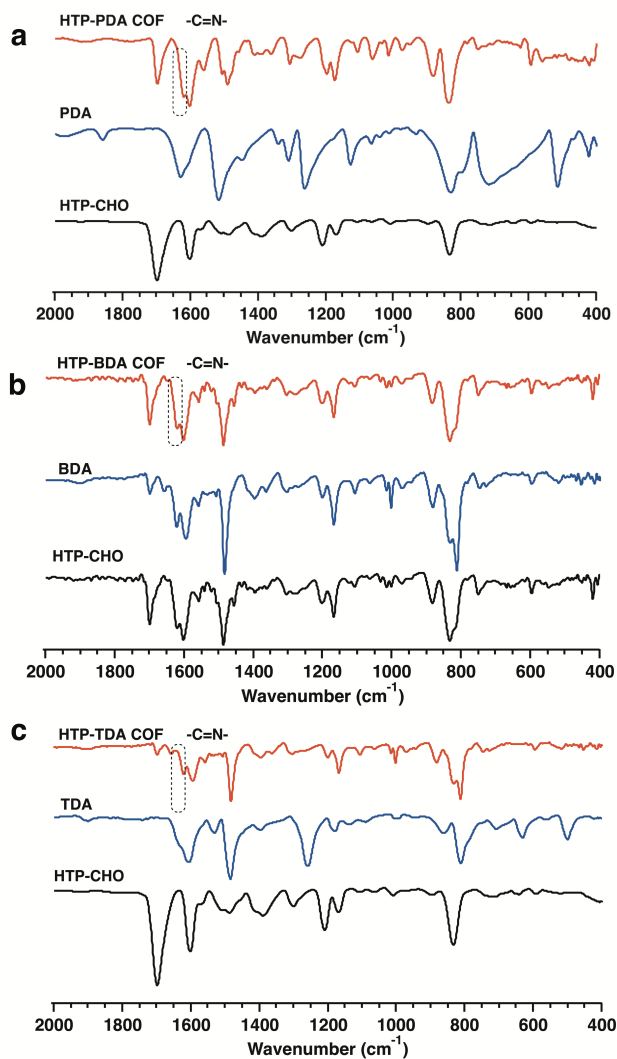


Figure 2.2 FT-IR spectra of (a) HTP-PDA COF, (b) HTP-BDA COF and (c) HTP-TDA COF.

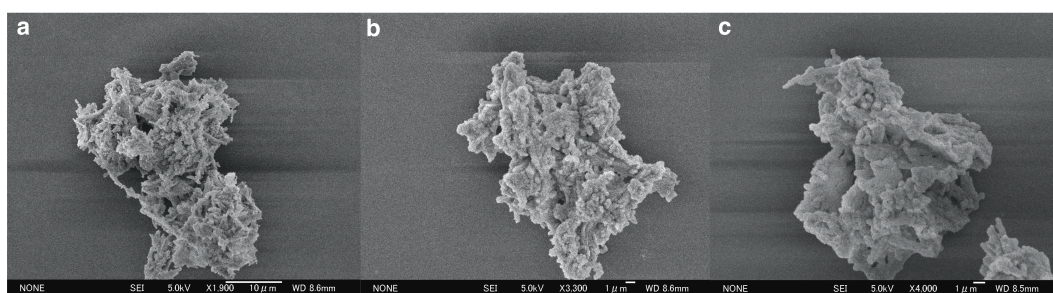


Figure 2.3 FE-SEM image of (a) HTP-PDA COF, (b) HTP-BDA COF and (c) HTP-TDA COF.

Crystal structures of the COFs were resolved by measuring experimental X-ray

diffraction (XRD) in conjunction with structural simulation and Pawley refinement (Figures 2.5 and 2.6). Experimentally, the HTP-PDA COF, HTP-BDA COF and HTP-TDA COF exhibited strong XRD signals at 4.1° , 3.4° and 3.0° , respectively, which were assigned to the (100) facets (Figures 2.5a, b and c, red curve). The (200) and (001) facets were observed for HTP-PDA-COF at 8.1° and 23.4° , HTP-BDA-COF at 6.9° and 24.7° , and HTP-TDA-COF at 6.1° and 24.6° , respectively. The presence of the (001) peak indicates that the periodicity of the 2D sheets is extended to the third dimension. The Pawley refinements (Figures 2.5a, b and c, green curve) reproduced the experimentally observed XRD pattern with a negligible difference (Figures 2.5a, b and c, black curve), confirming the correctness of the peak assignments.

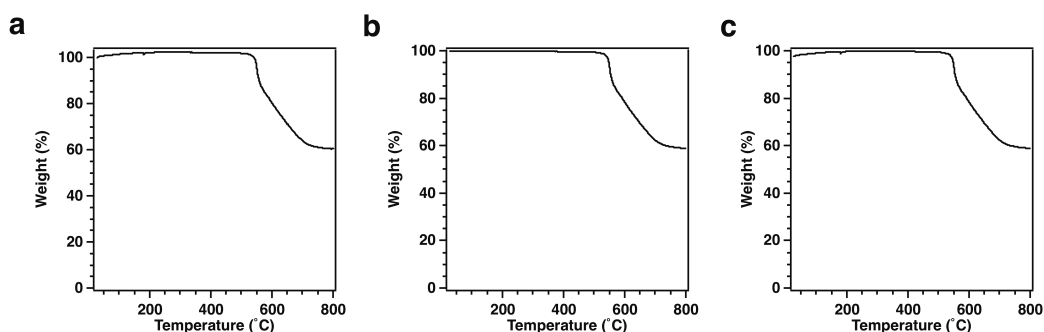


Figure 2.4 TGA curves of (a) HTP-PDA COF, (b) HTP-BDA COF and (c) HTP-TDA COF.

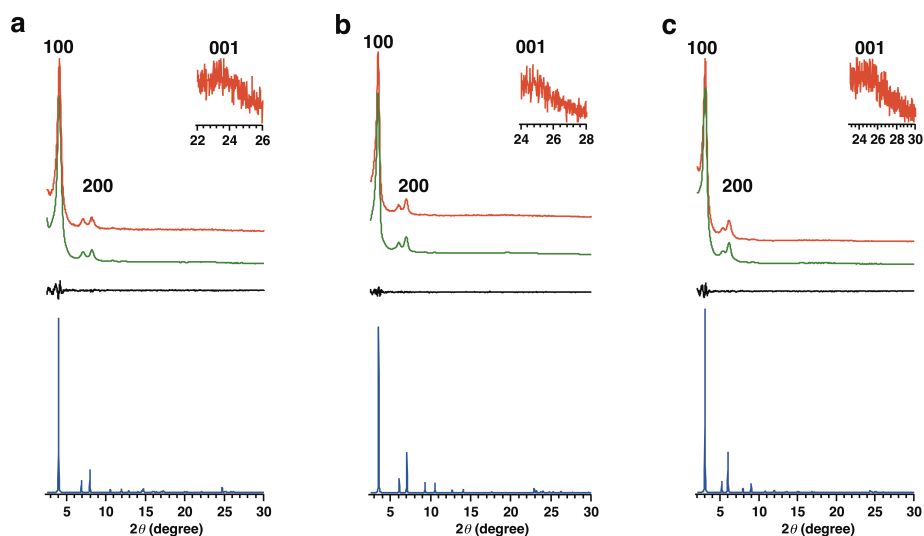


Figure 2.5 PXRD pattern of (a) HTP-PDA COF, (b) HTP-BDA COF and (c)

HTP-TDA COF with experimentally observed in red, Pawley refined in green, the difference (observed minus refined) in black and simulated using eclipsed AA staking structure in blue.

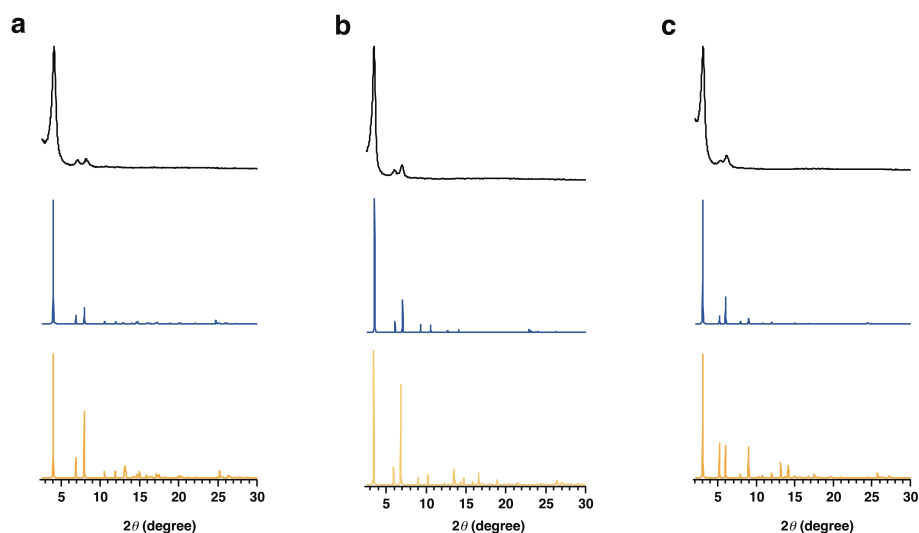


Figure 2.6 Comparison between experimental and simulated PXRD pattern of (a) HTP-PDA COF, (b) HTP-BDA COF and (c) HTP-TDA COF. Experimentally observed in black, simulated using eclipsed AA staking structure in blue and simulated using staggered AB staking structure in yellow.

Structural simulations were conducted using density-functional tight-binding (DFTB) method including Lennard–Jones (LJ) dispersion. For the simulation process, starting structures were created by AuToGraFS and pre-optimized using a topology-preserving force field. Then the monolayer was further optimized and further extended to layered frameworks with different stacking modes. From the monolayer structures, eclipsed AA and staggered AB modes were generated and optimized by DFTB method. The interlayer stacking distances for the central ring, and the corresponding LJ, and crystal stacking energies per monolayer of each structure are shown in Table 2.1. For all the three HTP-COFs, the eclipsed AA stacking mode was the more stable in comparison with the staggered AB mode (Tables 2.1). I used the eclipsed AA stacking mode to reconstruct the crystal structures of the HTP-COFs and the resulting PXRD patterns (Figures 2.5a, b, and C, blue curves) were in

agreement with the experimentally observed PXRD profiles. As for the simulated XRD of all staggered-AB COFs, the data (Figures 2.6a, b and c, yellow curve) are different from the experimentally observed XRD patterns. The eclipsed AA stacking mode between layers guarantees the triangular topology of the COF nanochannels.

Table 2.1 The total DFTB energies, Lennard-Jones contributions (LJ), and the crystal stacking energies per monolayer as well as the corresponding HOMO-LUMO energy gap for HTP-PDA COF, HTP-BDA COF and HTP-TDA COF.

COF	Stacking mood	Interlayer distance	Total Energy	LJ energy	Per layer stabilization (kcal. mol ⁻¹)	HOMO-LUMO gap (eV)
HTP-PDA	Monolayer	–	-165.82 4428	0.7284 60123	–	2.26989
	AA	3.89306	-331.86 28922	1.1898 78276	-67.1548157	1.9632
	AB	3.53614	-331.83 79938	1.2263 16732	-59.3428363	2.11261
HTP-BDA	Monolayer	–	-201.16 80095	0.8916 60574	–	2.30528
	AA	3.798735	-402.63 04837	1.4350 17599	-92.3896628	1.91653
	AB	3.402405	-402.62 14397	1.4947 76994	-89.5520690	2.03571
HTP-TDA	Monolayer	–	-236.51 6474	1.0591 41898	–	2.30482
	AA	3.785765	-473.38 16033	1.71143 6716	-109.392167	1.91064
	AB	3.46896	-473.27 92766	1.8547 80061	-77.2867328	2.13198

Specifically, the crystalline structures of COFs were determined using the density-functional tight-binding (DFTB) method including Lennard-Jones (LJ) dispersion. The calculations were carried out with the DFTB program package version 1.2. DFTB is an approximate density functional theory method based on the tight binding approach and utilizes an optimized minimal LCAO Slater-type all-valence basis set in combination with a two-center approximation for Hamiltonian matrix elements. The Coulombic interaction between partial atomic charges was determined using the self-consistent charge (SCC) formalism. Lennard-Jones type dispersion was employed in all calculations to describe van der Waals (vdW) and π -stacking interactions with starting structures created by AuToGraFS and pre-optimized using a topology-preserving force field were used to optimize the monolayer and were further extended to layered frameworks with different stacking modes. The lattice dimensions were optimized simultaneously with the geometry. Standard DFTB parameters for X-Y element pair (X, Y = C, H and N) interactions were employed from the mio-0-1 set10. The XRD pattern simulation was performed in a software package for crystal determination from PXRD pattern, implemented in MS modeling version 4.4 (Accelrys Inc.). I performed Pawley refinement to optimize the lattice parameters iteratively until the R_p and R_{WP} values converge. The pseudo-Voigt profile function was used for whole profile fitting and instrument geometry function as Bragg-Brentano was used during the refinement processes. The final unit cell parameters and refinement factors are summarized in Table 2.2.

Table 2.2 Final unit cell parameters and refinement factors for the COFs by using Material Studio module.

COFs	a (Å)	b (Å)	c (Å)	α (°)	β (°)	γ (°)	R_{WP}	R_p
HTP-PDA	25.85	26.06	7.27	90.27	89.02	60.03	6.49%	4.85%
HTP-BDA	29.87	30.09	7.17	90.18	89.91	60.01	8.09%	6.43%
HTP-TDA	35.07	35.34	7.53	91.31	91.00	60.16	5.33%	3.80%

The porosity of HTP-COFs was investigated by conducting nitrogen gas (N_2) adsorption at 77 K (Figure 2.7). The sharp uptake below $P/P_0 = 0.1$ justified the microporous character of these COFs. The BET surface area was $566 \text{ m}^2 \text{ g}^{-1}$ for HTP-PDA-COF, $1045 \text{ m}^2 \text{ g}^{-1}$ for HTP-BDA-COF and $933 \text{ m}^2 \text{ g}^{-1}$ for HTP-TDA-COF, respectively. The pore size distribution calculated by nonlocal density functional theory (NLDFT) revealed two main peaks for each HTP-COF. The specific pore size was concluded basing on the peak position as 11 and 15 Å for HTP-PDA COF, 12 and 16 Å for HTP-BDA COF and 13 and 17 Å for HTP-TDA COF. The dual-pore structure expected based on the geometry feature of HTP-CHO was corroborated by the pore size distribution concluded from the N_2 sorption results.

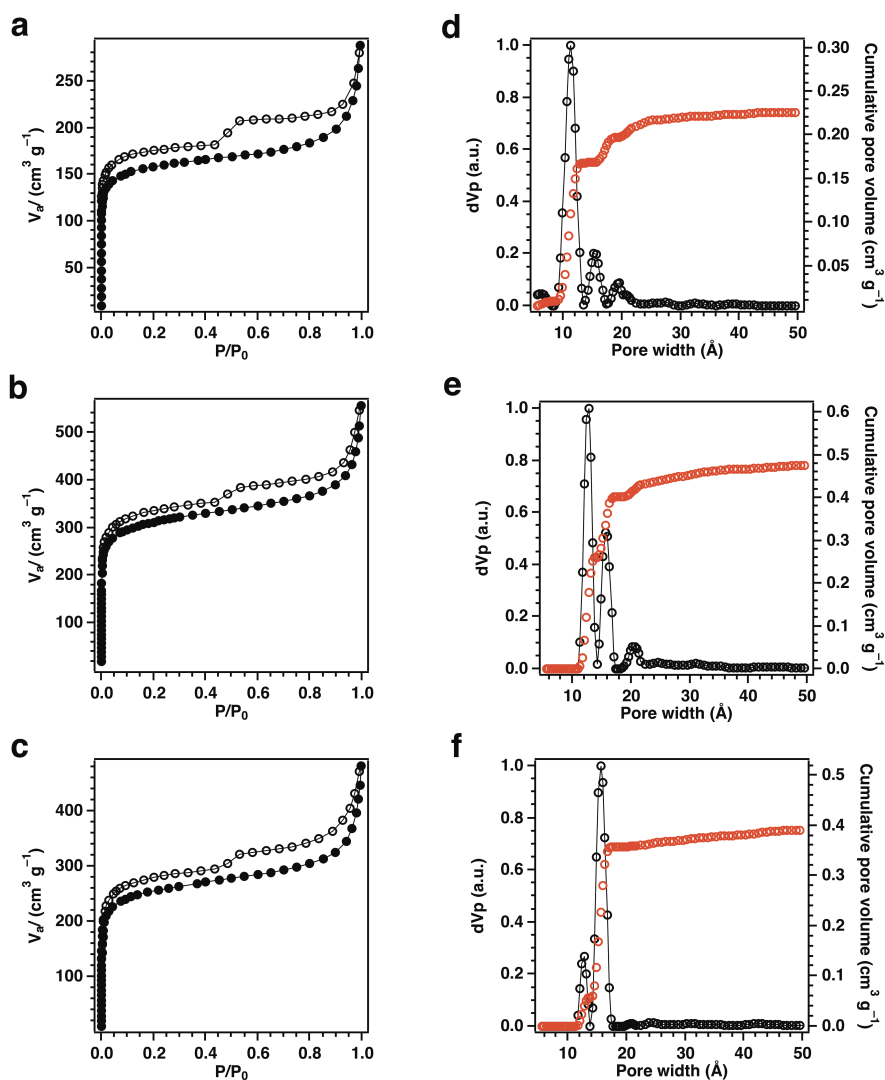


Figure 2.7 Nitrogen sorption isotherm profiles of (a) HTP-PDA COF, (b) HTP-BDA

COF, (c) HTP-TDA COF. Pore size distribution profiles of (d) HTP-PDA COF, (e) HTP-BDA COF, (f) HTP-TDA COF.

2.2.3 CO₂ Uptake

To date, a great number of porous polymers have been prepared and utilized in the context of CO₂ capture and separation. These investigation reveals the microporous materials are more effective for CO₂ adsorption in comparison of the mesoporous analogues.³⁵ Therefore, the large surface area and microporosity endow HTP-COFs with promising application for CO₂ storage.

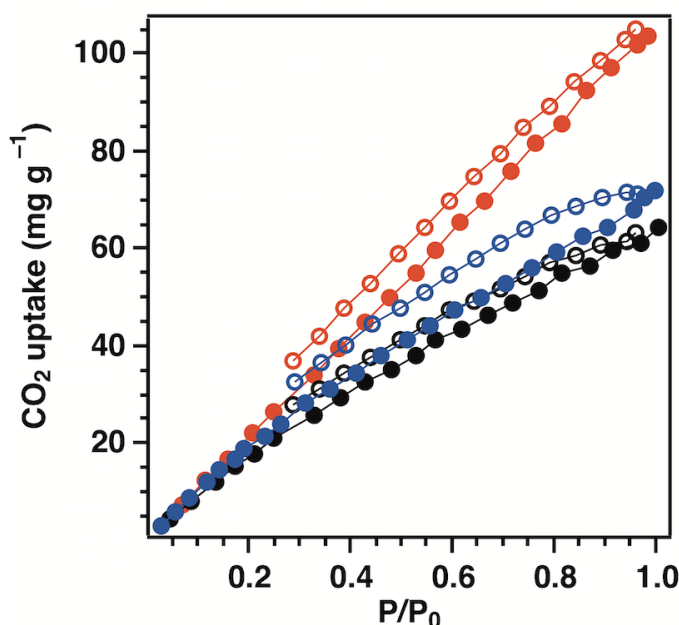


Figure 2.8 CO₂ sorption curve of (a) HTP-PDA COF in black, (b) HTP-BDA COF in red and (c) HTP-TDA COF in blue at 273 K and 1 bar.

At 273 K and 1 bar, the uptakes CO₂ with high values of 64.6, 103.9 and 72.0 mg g⁻¹ for HTP-PDA COF, HTP-BDA COF and HTP-TDA COF, respectively. The uptake capacity ranks HTP-BDA COF a top COF material for CO₂ uptake reported to date, exceeding COF-5 (5.9 wt%),³⁶ COF-102 (1.21 wt%),³⁶ COF-103 (7.6 wt%),³⁶ ILCOF-1 (6.0 wt%),³⁷ TDCOF-5 (9.2 wt%),³⁸ and comparable to TpPa-1 (15.6 wt%)³⁹ at 273 K and 1 bar.

2.3 Conclusion

In summary, basing on topology predesign, I developed three microporous HTP-COFs bearing triangular topology and dual-pore structure. The strategy generality was confirmed by systematically extending the linker length and a series of COFs of the same topology but slightly dimension difference were created. Benefited from the large planar structure of HTP core which facilitates the π - π interaction between layers, the resulting COFs exhibit high crystallinity, large surface area, uniform microporous dual-pore structure and excellent CO₂ capture capacity. These results suggest the microporous HTP-COFs have great potential towards molecular adsorption and separation.

2.4 Experimental Sections

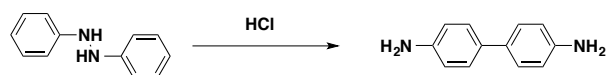
2.4.1 Methods

JEOL models JNM-LA400 NMR spectrometers were used to measure the ¹H nuclear magnetic resonance (NMR) spectra. Using the solvent residual proton peaks as reference, the chemical shifts (δ in ppm) of compounds are confirmed. A JASCO model FT-IR-6100 infrared spectrometer was used to determine the Fourier transform infrared (FT-IR) spectra. The Rigaku model RINT Ultima III diffractometer was used to confirm the crystallinity character by the Powder X-ray diffraction (PXRD) data. Detailly, the sample powder was deposited on glass substrate and the measure starts from $2\theta = 2.5^\circ$ up to 30° with 0.02° increment. At 77 K created by liquid nitrogen, a Micromeritics Instrument Corporation model 3Flex surface characterization analyzer was used to measure the nitrogen sorption isotherms. The specific surface areas and the pore distribution was confirmed by the Brunauer-Emmett-Teller (BET) method and the non-local density functional theory (NLDFT) model, respectively. A Bel Japan Inc. model BELSORP-mini II analyzer was used to confirm the carbon dioxide sorption isotherms. For the isotherm measurements, all the samples were degassed in vacuum at 120 °C for more than 10 h. A Mettler-Toledo model TGA/SDTA851e was used to measure the TGA curves in nitrogen atmosphere at a rate of 10 °C min⁻¹. The JEOL model JSM-6700 was used for field-emission scanning electron microscopy

(FE-SEM). The operation is conducted at an accelerating voltage of 5.0 kV. To improved sample conductivity, before measure, the sample was coated by gold after drop-casting its acetone suspension on mica substrate.

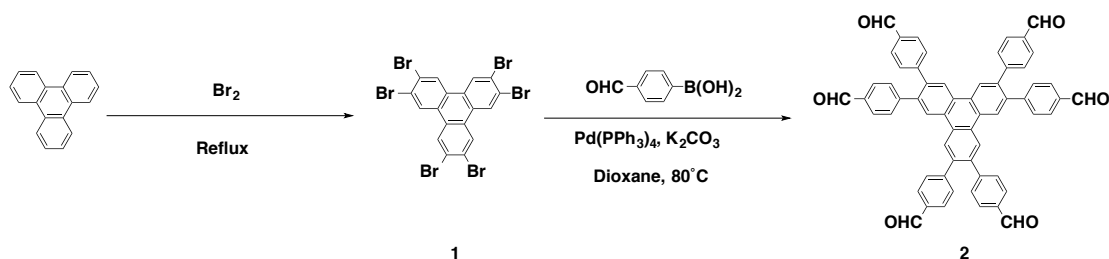
Reflex, a software package to determine the crystal XRD pattern, was used for Molecular modeling and Pawley refinement. The simulation work was implemented in Material Studio modeling version 8 (Accelrys Inc.). The crystalline structures of COFs were determined using the density-functional tight-binding (DFTB) method including Lennard-Jones (LJ) dispersion. The calculations were carried out with the DFTB program package version 1.2. DFTB is an approximate density functional theory method based on the tight binding approach and utilizes an optimized minimal LCAO Slater-type all-valence basis set in combination with a two-center approximation for Hamiltonian matrix elements. The Coulombic interaction between partial atomic charges was determined using the self-consistent charge (SCC) formalism. Lennard-Jones type dispersion was employed in all calculations to describe van der Waals (vdW) and π -stacking interactions with starting structures created by AuToGraFS and pre-optimized using a topology-preserving force field were used to optimize the monolayer and were further extended to layered frameworks with different stacking modes. The lattice dimensions were optimized simultaneously with the geometry. Standard DFTB parameters for X-Y element pair (X, Y = C, H and N) interactions were employed from the mio-0-1 set10. I performed Pawley refinement to optimize the lattice parameters iteratively until the R_p and R_{WP} values converge. The pseudo-Voigt profile function was used for whole profile fitting and instrument geometry function as Bragg–Brentano was used during the refinement processes.

2.4.2 Synthetic Procedures



4,4'-diaminobiphenyl.⁴⁰ Hydrazobenzene (5.0 g, 27.1 mmol) was dissolved into EtOH/water (3:1, 200 mL) and the system was cooled to 0 °C. Concentrated hydrochloric acid (20 mL, 57.4 mmol) was diluted by EtOH/water (11:4, 300 mL) and

added the diluted acid into the hydrazobenzene solution at 0 °C. Let the system stir for 24 h and gradually warm to room temperature. Evaporated EtOH and cooled the system to get white crystal. The crystal was dissolved into 200 mL water and the solution was neutralized by saturated sodium bicarbonate solution. Extracted the aqueous solution by dichloromethane (3×300 mL). The organic part was dried over sodium magnesium and evaporated to obtained brown solid. The brown solid was recrystallized in water and the final product was collected as white crystal (59% yield). ¹H NMR (400MHz, CDCl₃, 25 °C): δ (ppm) 7.36 (4H, d, J = 8.4 Hz, ArH), 6.75 (4H, d, J = 8.8 Hz, ArH), 3.67 (4H, s, -NH₂).



2,3,6,7,10,11-Hexabromotriphenylene (1).⁴¹ Triphenylene (1 g, 2.4 mmol) was dissolved into nitrobenzene (40 mL) in accompany of iron powder (80 mg). Bromine (3 mL, 58 mmol) was added slowly into the system over 5 min. The system was kept still overnight and then heated to reflux for 2 h. The system was cooled down to room temperature and diethyl ether (100 mL) was added into it. The black solid was filtered out and recrystallized from 1,2-dichlorobenzene. The final product is white crystal which is insoluble in common solvent. Take the sample directly into next step reaction without further characterization (90% yield).

2,3,6,7,10,11-hexakis (4-formylphenyl) triphenylene (HTP-CHO, 2). A mixture of 2,3,6,7,10,11-hexabromotriphenylene (140.2 mg, 0.2 mmol), tetrakis(triphenylphosphine)palladium(0) (138.6 mg, 0.12 mmol), K₂CO₃ (248.4 mg, 1.8 mmol), 4-formylphenylboronic acid (270 mg, 1.8 mmol), and toluene/methanol/dioxane (20 mL, 2/1/1 by vol.) in a 50 mL two-necked round bottle flask was purged with Ar for 30 minutes and stirred under reflux for 48 h. After cooling to room temperature, the solvent was evaporated and extracted the residual by CHCl₃, washed it with water and brine and dried it over anhydrous MgSO₄. The

solvent was removed under vacuum and purified the resulting solid by column chromatography (silica gel, CHCl₃: AcOEt = 19:1) to give HTP-CHO as white solid (82% yield). ¹H NMR (400 MHz, CDCl₃, 25 °C): δ (ppm) 10.021 (s, 6H, -CHO), 8.753 (s, 6H, ArH), 7.85 (d, 12H, J = 8.2 Hz, ArH), 7.49 (d, 12H, J = 8.2 Hz, ArH).

General synthesis of COFs. All COFs were prepared by a procedure identical to the one described here for the synthesis of HTP-BDA COF. An *o*-DCB/*n*-BuOH (0.5/0.5 mL) mixture of BDA (0.070 mmol, 13 mg) and HTP-CHO (0.023 mmol, 20 mg) in the presence of an acetic acid catalyst (6 M, 0.1 mL) in a Pyrex tube (10 mL) was degassed via three freeze–pump–thaw cycles. Sealed the tube and heated at 120 °C for five days. Centrifuged the solid part out and washed it six times with THF. Soxhlet was conducted to the COF sample using THF as solvent for one day to remove the trapped guest molecules. The sample was collected and dried at 120 °C under vacuum overnight to produce HTP-BDA COF in an isolated yield of 84%.

2.5 References

1. Côté A. P., Benin A. I., Ockwig N. W., O’Keeffe M., Matzger A. J., Yaghi O. M. Porous, crystalline, covalent organic frameworks. *Science* **310**, 1166-1170 (2005).
2. El-Kaderi H. M., *et al.* Designed synthesis of 3D covalent organic frameworks. *Science* **316**, 268-272 (2007).
3. Waller P. J., Gandara F., Yaghi O. M. Chemistry of covalent organic frameworks. *Acc. Chem. Res.* **48**, 3053-3063 (2015).
4. Diercks C. S., Yaghi O. M. The atom, the molecule, and the covalent organic framework. *Science* **355**, 923-930 (2017).
5. Huang N., Wang P., Jiang D. Covalent organic frameworks: A materials platform for structural and functional designs. *Nat. Rev. Mater.* **1**, 68 (2016).
6. Feng X., Ding X., Jiang D. Covalent organic frameworks. *Chem. Soc. Rev.* **41**, 6010-6022 (2012).
7. Ding S. Y., Wang W. Covalent organic frameworks (COFs): From design to applications. *Chem. Soc. Rev.* **42**, 548-568 (2013).

8. Dogru M., Bein T. On the road towards electroactive covalent organic frameworks. *Chem. Commun.* **50**, 5531-5546 (2014).
9. DeBlase C. R., Dichtel W. R. Moving beyond boron: The emergence of new linkage chemistries in covalent organic frameworks. *Macromolecules*, **49**, 5297-5305 (2016).
10. Xu H., Gao J., Jiang D. L. Stable, crystalline, porous, covalent organic frameworks as a platform for chiral organocatalysts. *Nat. Chem.* **7**, 905-912 (2015).
11. Xu H.-S., Ding S.-Y., An W.-K., Wu H., Wang W. Constructing crystalline covalent organic frameworks from chiral building blocks. *J. Am. Chem. Soc.* **138**, 11489-11492 (2016).
12. Wang X., Han X., Zhang J., Wu X., Liu Y., Cui Y. Homochiral 2D porous covalent organic frameworks for heterogeneous asymmetric catalysis. *J. Am. Chem. Soc.* **138**, 12332-12335 (2016).
13. Sun Q., Aguila B., Perman J., Nguyen N., Ma S. Flexibility matters: Cooperative active sites in covalent organic framework and threaded ionic polymer. *J. Am. Chem. Soc.* **138**, 15790-15796 (2016).
14. Doonan C. J., Tranchemontagne D. J., Glover T. G., Hunt J. R., Yaghi O. M. Exceptional ammonia uptake by a covalent organic framework. *Nat. Chem.* **2**, 235-238 (2010).
15. Huang N., Chen X., Krishna R., Jiang D. Two-dimensional covalent organic frameworks for carbon dioxide capture through channel-wall functionalization. *Angew. Chem. Int. Ed.* **54**, 2986-2990 (2015).
16. Huang N., Krishna R., Jiang D. Tailor-made pore surface engineering in covalent organic frameworks: Systematic functionalization for performance screening. *J. Am. Chem. Soc.* **137**, 7079-7082 (2015).
17. Dalapati S., Jin E., Addicoat M., Heine T., Jiang D. Highly emissive covalent organic frameworks. *J. Am. Chem. Soc.* **138**, 5797-5800 (2016).
18. Ding S. Y., *et al.* Thioether-based fluorescent covalent organic framework for

- selective detection and facile removal of mercury(II). *J. Am. Chem. Soc.* **138**, 3031-3037 (2016).
19. Xu H., Tao S., Jiang D. Proton conduction in crystalline and porous covalent organic frameworks. *Nat. Mater.* **15**, 722-726 (2016).
 20. Chandra S., *et al.* Phosphoric acid loaded azo ($-N=N-$) based covalent organic framework for proton conduction. *J. Am. Chem. Soc.* **136**, 6570-6573 (2014).
 21. Ma H., *et al.* Cationic covalent organic frameworks: A simple platform of anionic exchange for porosity tuning and proton conduction. *J. Am. Chem. Soc.* **138**, 5897-5903 (2016).
 22. Dogru M., *et al.* A photoconductive thienothiophene-based covalent organic framework showing charge transfer towards included fullerene. *Angew. Chem. Int. Ed.* **52**, 2920-2924 (2013).
 23. Guo J., *et al.* Conjugated organic framework with three-dimensionally ordered stable structure and delocalized π clouds. *Nat. Commun.* **4**, 2736 (2013).
 24. Jin S., *et al.* Charge dynamics in a donor-acceptor covalent organic framework with periodically ordered bicontinuous heterojunctions. *Angew. Chem. Int. Ed.* **52**, 2017-2021 (2013).
 25. Xu F., *et al.* Electrochemically active, crystalline, mesoporous covalent organic frameworks on carbon nanotubes for synergistic lithium-ion battery energy storage. *Sci. Rep.* **5**, 8225 (2015).
 26. Xu F., *et al.* Radical covalent organic frameworks: A general strategy to immobilize open-accessible polyradicals for high-performance capacitive energy storage. *Angew. Chem. Int. Ed.* **54**, 6814-6818 (2015).
 27. DeBlase C. R., Silberstein K. E., Truong T. T., Abruna H. D., Dichtel W. R. β -ketoenamine-linked covalent organic frameworks capable of pseudocapacitive energy storage. *J. Am. Chem. Soc.* **135**, 16821-16824 (2013).
 28. Huang N., *et al.* Multiple-component covalent organic frameworks. *Nat. Commun.* **7**, 12325 (2016).
 29. Zhu Y., Wan S., Jin Y., Zhang W. Desymmetrized vertex design for the synthesis

- of covalent organic frameworks with periodically heterogeneous pore structures. *J. Am. Chem. Soc.* **137**, 13772-13775 (2015).
30. Qian C., Qi Q.-Y., Jiang G.-F., Cui F.-Z., Tian Y., Zhao X. Toward covalent organic frameworks bearing three different kinds of pores: The strategy for construction and COF-to-COF transformation via heterogeneous linker exchange. *J. Am. Chem. Soc.* **139**, 6736-6743 (2017).
 31. Li B., *et al.* Dual functionalized cages in metal–organic frameworks via stepwise postsynthetic modification. *Chem. Mater.* **28**, 4781-4786 (2016).
 32. Dalapati S., *et al.* Rational design of crystalline supermicroporous covalent organic frameworks with triangular topologies. *Nat. Commun.* **6**, 7786 (2015).
 33. Xu S.-Q., Zhan T.-G., Wen Q., Pang Z.-F., Zhao X. Diversity of covalent organic frameworks (COFs): A 2D cof containing two kinds of triangular micropores of different sizes. *ACS Macro Lett.* **5**, 99-102 (2016).
 34. Alahakoon S. B., Thompson C. M., Nguyen A. X., Occhialini G., McCandless G. T., Smaldone R. A. An azine-linked hexaphenylbenzene based covalent organic framework. *Chem. Comm.* **52**, 2843-2845 (2016).
 35. Zeng Y., Zou R., Zhao Y. Covalent organic frameworks for CO₂ capture. *Adv. Mater.* **28**, 2855-2873 (2016).
 36. Furukawa H., Yaghi O. M. Storage of hydrogen, methane, and carbon dioxide in highly porous covalent organic frameworks for clean energy applications. *J. Am. Chem. Soc.* **131**, 8875-8883 (2009).
 37. Rabbani M. G., Sekizkardes A. K., Kahveci Z., Reich T. E., Ding R., El-Kaderi H. M. A 2D mesoporous imine-linked covalent organic framework for high pressure gas storage applications. *Chem. Eur. J.* **19**, 3324-3328 (2013).
 38. Kahveci Z., Islamoglu T., Shar G. A., Ding R., El-Kaderi H. M. Targeted synthesis of a mesoporous triptycene-derived covalent organic framework. *CrystEngComm* **15**, 1524-1527 (2013).
 39. Kandambeth S., Mallick A., Lukose B., Mane M. V., Heine T., Banerjee R. Construction of crystalline 2D covalent organic frameworks with remarkable

- chemical (acid/base) stability via a combined reversible and irreversible route. *J. Am. Chem. Soc.* **134**, 19524-19527 (2012).
40. Clegg J. et al. A stimuli responsive system of self-assembled anionbinding $\text{Fe}_4\text{L}_6^{8+}$ cages. *Chem. Sci.* **4**, 68-76 (2013).
41. Breslow R., Jaun B., Kluttz R. Q., Xia C.-z. Ground state π -electron triplet molecules of potential use in the synthesis of organic ferromagnets. *Tetrahedron* **38**, 863-867 (1982).

**Chapter 3. Sub-angstrom Molecular
Discrimination in Crystalline Microporous
Covalent Organic Frameworks**

Abstract The energy economic character and essentially infinite selectivity make size exclusive separation attractive candidate for traditional separation. However, conventional porous materials can barely realize demands of designable discrete pore size and descent chemical stability. Covalent organic frameworks (COFs) characterize by aligned one-dimensional channels ranging from micro- to mesoporous scale and precise structure designability, which endow them with molecular sieve potential. Besides, the instinct chemical stability originated from the covalent bonds makes COF molecular sieves especially suitable for bulky molecule separation operated in solutions. Here I elaborated a crystalline and microporous triangular COF as size exclusive adsorbent for bulky neutral molecular mixtures. The COF realized discrimination at sub-angstrom level by including molecules with size of 15.0 Å into the 15.6 Å triangular channels but exclude the counterpart with size of 15.5 Å. The size exclusive adsorption behavior was confirmed by single compound adsorption experiment and energy calculation. The guest molecule accommodation within COF channels was affirmed by gas sorption measurement.

3.1 Introduction

Separation techniques depending on equilibrium separation are essential for the modern industrial economy and cover approximately 10 to 15% of the world energy consumption.¹ Adsorptive separation based on porous materials as separation agents is regarded as an economic alternative to traditional separation approaches.² Adsorptive separation can be realized basing on (1) interaction difference between guest molecules and adsorbents,³⁻⁵ or (2) size exclusion—molecules smaller than the apertures are permitted to enter while bigger ones are denied.^{6, 7} On principle, size-exclusive separation can offer essentially infinite selectivity and thus highly attractive.

For size exclusive adsorbents, it is the pore distribution that determines the discrimination ability—the narrower the distribution, the smaller the difference between the molecules being adsorbed and excluded. The ideal adsorbents are the porous materials bearing discrete pore distribution. This requirement can barely be realized by conventional amorphous porous materials but is common character of crystalline frameworks including zeolites, metal organic frameworks (MOFs) and covalent organic frameworks (COFs). Zeolites are the most well-known molecular sieving adsorbents and have been successfully applied for petrochemical industry.^{8,9} However, the performance of zeolites is impaired by the limited pore designability owing to the determined obtuse O-Si-O and Si-O-Si angles.¹⁰ The high coordination numbers endow MOFs with various pore structures and a wide range of aperture size, making them more promising size-exclusive adsorbents. By fine-tuning the aperture on 0.1 Å level, MOFs successfully sieved linear paraffin over branched isomer¹¹ and alkene over alkane⁶. The rapid development of biochemistry, pharmacy and commodity makes the separation and purification of organic molecule larger than 1 nm on highly demand. Since the bulky molecule separation usually conducts in solution, the poor humidity stability of MOFs makes them not competitive for separation in solution.

Two-dimensional (2D) COFs are frameworks consisted of pure organic

composites and linkages.¹² They are characterized by aligned one-dimensional (1D) nanochannels resulting from crystallization of covalently linked organic polygons.¹³⁻¹⁹ The structural designability enables the discrete channel size control on angstrom level, rendering COFs able to construct molecular sieves. Therefore, COFs are potentially very interesting platform for designing molecular sieves. Furthermore, the covalent linkages endow COFs with outstanding structural stability in water and common organic solvents.²⁰ These crystalline porous polymers are attractive in various fields, including catalysis,²¹⁻²³ gas adsorption,²⁴⁻²⁶ sensing,²⁷⁻²⁸ proton conduction,^{29, 30} environment issues,^{31, 32} and energy conversion³³⁻³⁶ and storage^{37, 38} but they are barely explored for molecular discrimination. Actually, the pore structure designability and robust skeleton endow COFs with promising potential as molecular sieves for both gas mixtures and multi-compound solutions.

It has to be pointed out, though size exclusive separation of bulky ions has been detailed before. The assistant of electrostatic interaction makes the dimension requirement of ion size exclusion totally different from that of neutral molecule. The electronic interaction is strong enough to regular the orientation of ionic guests. So when the minimum dimension of the ion is beneath the size of sieving media, the guests could enter into pores and the separation occurred. But for neutral molecules, the neutral molecules cannot voluntarily diffuse into adsorbent nanochannels whose window sizes are smaller than the largest dimension of guests. It means the character dimension of neutral molecules is the maximum dimension rather than the minimum one. Only when the media pore larger than the maximum dimension of guest molecules, can the molecular sieves work. This phenomenon has been observed in ion separation researches^{39, 40} but never been pointed out before. Actually the most bulky organic molecules are not charged but by far there are no molecular sieves being developed targeting to these neutral bulky molecules.

In this study, I explored the discrimination potential of COFs as neutral molecular sieves by design and synthesis a new COF bearing microporous triangular channels. The triangular topology endows the COF with countless microporous channels whose

dimension is comparable to the size of neutral molecules. Sub-angstrom-level molecular discrimination was achieved by the COF driven by the uptake behavior of the 1D nanochannels—adsorbing molecules with size of 15.0 Å but excluding analogues with size of 15.5 Å. Solution separation experiments and chromatographic column studies revealed that the COF enabled rapid separation of mixtures with molecular dimension difference on sub-angstrom level. The molecular sieve mechanism was further confirmed by single compound adsorption experiment, bonding energy calculation and gas sorption measurement.

3.2 Results

3.2.1 Design and Synthesis

Bulky molecules with dimension excess than 1 nm is widely produced and researched for cosmetic industry and biochemistry field. In this study I determined to design COF molecular sieves targeting on relatively large molecules of this dimension. Basing on separation task, COF with channels on the same scale is required. Previous report demonstrated that triangular topology was an optimum approach to microporous COFs,⁴¹ so I determined to synthesis a microporous COF basing on the triangular topology design. Though several triangular COFs have been reported, but the poor crystallinity and inferior pore structure make them not appropriate separation media for the sake of separation selectivity and capacity.⁴¹⁻⁴³

The synthesis of high quality triangular COF starts from the delicate monomer design. HTP-BDA COF was synthesized by selecting 1,1'-biphenyl-4,4'-diamine (BDA) as linkers and the six-arm HTP-CHO as vertices (Figure 3.1). The biphenyl linkers contribute to maximum COF long-range order degree by site locking, resulting the crystallinity and surface area enhancement in comparison with structure analogue HAT COF.⁴⁴ Additionally, different from the C_6 -symmetry building blocks reported in the previous work,⁴¹ the six arms of HTP-CHO are not identical and thus dual-pore structure can be expected for the HTP-BDA COFs.

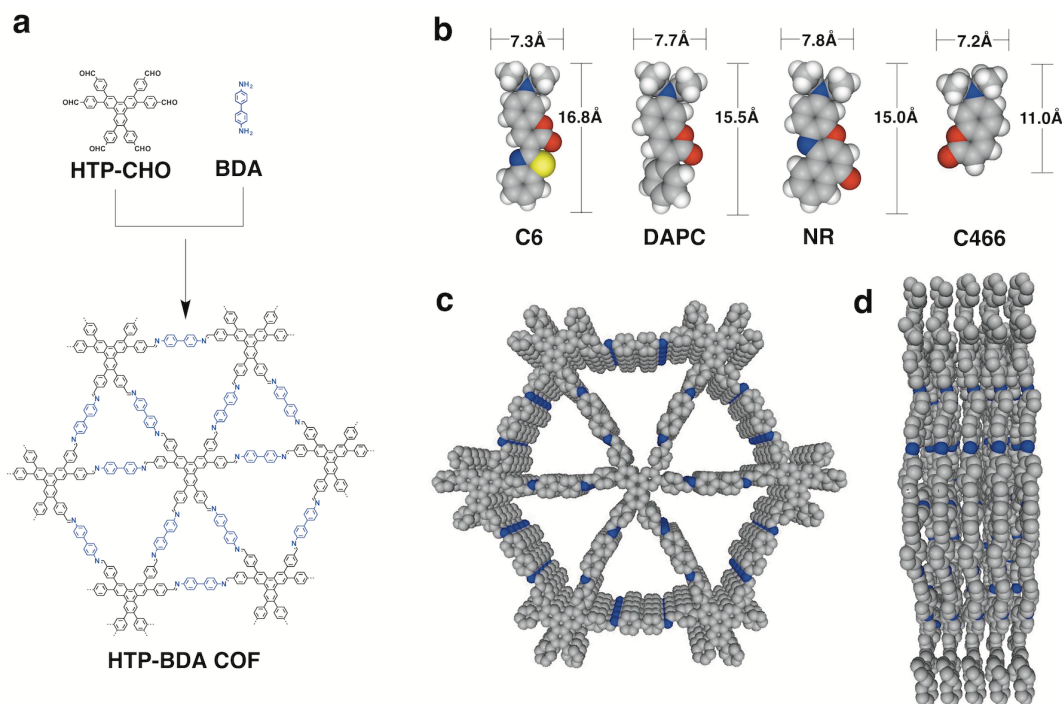


Figure 3.1 Schematic representation of the HTP-BDA COF synthesis. (a) Synthesis of HTP-BDA COF through the condensation of HTP-CHO (black) and BDA (blue). (b) Structures of the guest molecules used for exploration the separation capability of HTP-BDA COF (blue, N; yellow, S; gray, C; white, H). Top (c) and side (d) views of HTP-BDA COF (blue, N; gray, C; hydrogen is omitted for clarity).

The triangular COF was synthesized solvothermally by dispersing HTP-CHO and BDA in mixture solution of *o*-DCB: *n*-BuOH: 6M aqueous acetic acid = 5:5:1 (v:v:v) and heating at 120 °C for 5 days, giving yellow solid in an isolated yield of 84%. Fourier transform infrared spectra (FT-IR) presented absorption at 1620 cm^{-1} for the HTP-BDA COF, which corresponded to the vibration band of C=N group (Figure 3.2). The COF adopted particle morphology as revealed by field-emission scanning electron microscopy (FE-SEM) (Figure 3.3). HTP-BDA COF presented high thermal stability justified by thermogravimetric analysis (TGA) up to 500 °C (Figure 3.4).

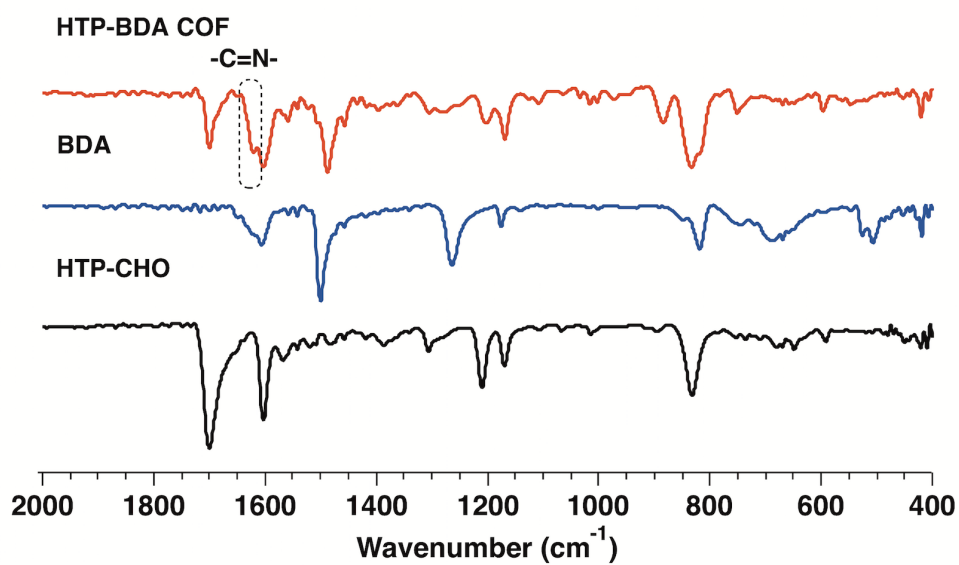


Figure 3.2 FT-IR spectra of HTP-BDA COF (red), BDA (blue) and HTP-CHO (black).

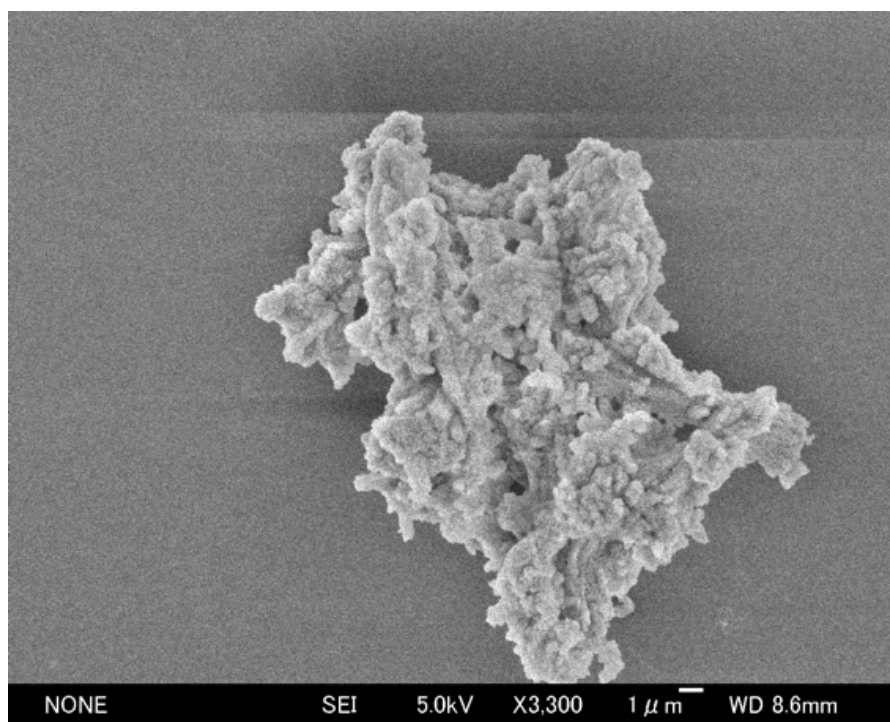


Figure 3.3 FE-SEM image of HTP-BDA COF.

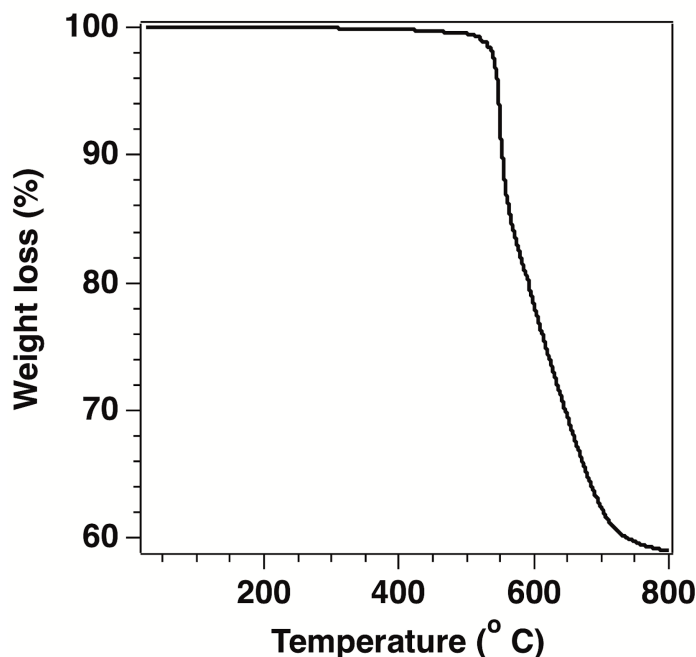


Figure 3.4 TGA curve of HTP-BDA COF under N₂.

3.2.2 Crystallinity and Porosity

Crystal structure of the HTP-BDA COF was resolved by measuring experimental X-ray diffraction (XRD) in conjunction with Pawley refinement and structural simulation (Figure 3.5). Experimentally, the HTP-BDA COF exhibited XRD signals at 3.42°, 5.98°, 6.96, 9.26, 10.38 and 19.77 respectively, which were assigned to the (100), (110), (200), (210), (300) and (510) facets (Figure 3.5a red curve). The Pawley-refined pattern (green curve) with R_{wp} and R_p values of 5.61% and 3.90%, respectively, confirmed the correctness of peak assignments by negligible deviation from the observed PXRD patterns (black curve).

Structural simulations were conducted using density-functional tight-binding (DFTB) method including Lennard–Jones (LJ) dispersion. The starting simulative structures was created by AuToGraFS and pre-optimized using a topology-preserving force field. Then the monolayer was further optimized and was further extended to layered frameworks with different stacking modes. From the monolayer structures, eclipsed AA and staggered AB modes were generated and optimized by DFTB method. The interlayer stacking distances for the central ring, and the corresponding

LJ, and crystal stacking energies per monolayer of each structure are shown in Table 3.1. The eclipsed AA stacking mode was the more stable in comparison with the staggered AB mode. I used the eclipsed AA stacking mode to reconstruct the crystal structure of the HTP-BDA COF and the resulting PXRD pattern (Figure 3.5a, blue curves) was in agreement with the experimentally observed PXRD profile, assuming the space group $P3$ with unit cell parameters of $a = b = 29.1211 \text{ \AA}$, $c = 3.8840 \text{ \AA}$, $\alpha = \beta = 90^\circ$, and $\gamma = 120^\circ$. As for the simulated XRD of staggered-AB condition, the data is different from the experimentally observed XRD pattern.

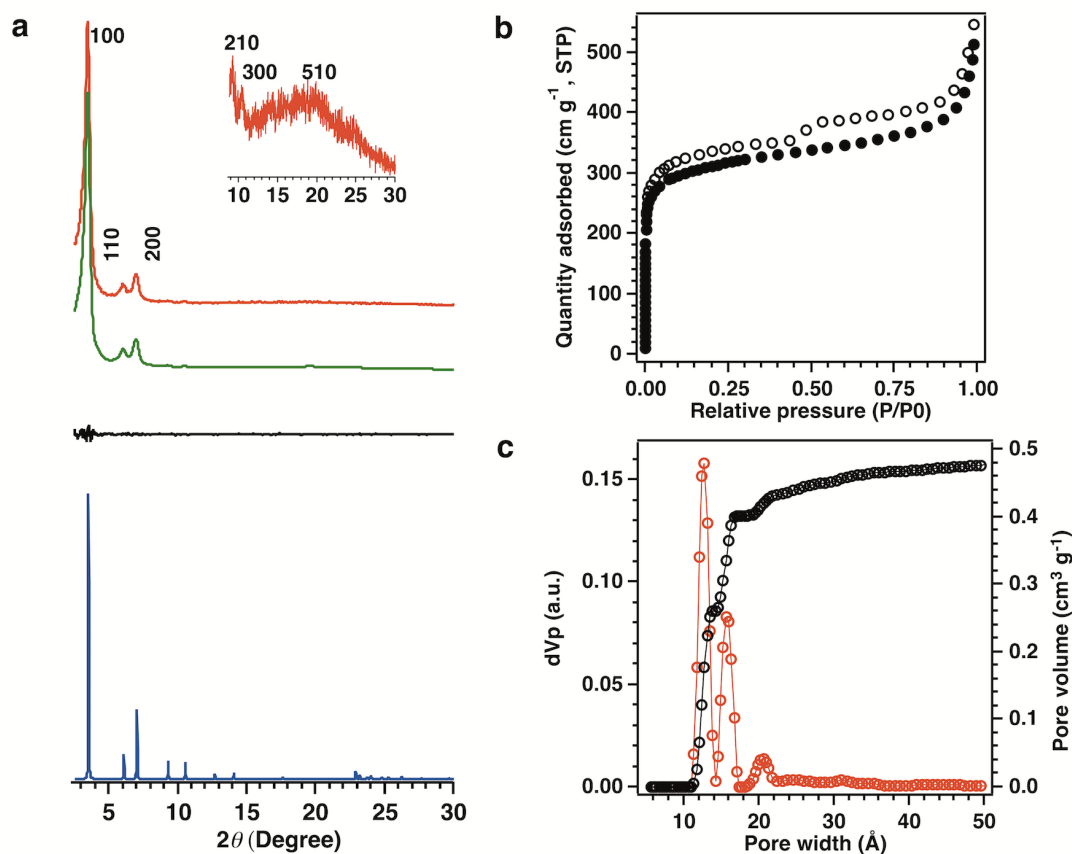


Figure 3.5 Crystallinity and porosity. (a) PXRD profiles of HTP-BDA COF. Experimentally observed (red), Pawley refined (green), their difference (black) and simulated using the AA stacking mode (blue). (b) Nitrogen-sorption isotherm curves measured at 77 K. (c) Profiles of the pore size distribution.

Table 3.1 The total DFTB energies, Lennard-Jones contributions (LJ), and the crystal stacking energies per monolayer as well as the corresponding HOMO-LUMO energy gap for HTP-BDA COF.

Stacking	c [Å]	Total DFTB Energy [a.u.]	LJ energy [a.u.]	Per unit crystal stacking energy [kcal.mol ⁻¹]	HOMO-LUMO gap [eV]
monolayer	–	-201.168009	0.8917	–	2.305
AA	3.80	-402.630484	1.4350	-92.39	1.917
AB	3.40	-402.6214397	1.4948	-89.55	2.036

Specifically, the crystalline structures of COFs were determined using the density-functional tight-binding (DFTB) method including Lennard-Jones (LJ) dispersion. The calculation was carried out with the DFTB program package version 1.2. DFTB is an approximate density functional theory method based on the tight binding approach and utilizes an optimized minimal LCAO Slater-type all-valence basis set in combination with a two-center approximation for Hamiltonian matrix elements. The Coulombic interaction between partial atomic charges was determined using the self-consistent charge (SCC) formalism. Lennard-Jones type dispersion was employed in all calculations to describe van der Waals (vdW) and π -stacking interactions with starting structures created by AuToGraFS and pre-optimized using a topology-preserving force field were used to optimize the monolayer and were further extended to layered frameworks with different stacking modes. The lattice dimension was optimized simultaneously with the geometry. Standard DFTB parameters for X-Y element pair (X, Y = C, H and N) interactions were employed from the mio-0-1 set¹⁰. The XRD pattern simulation was performed in a software package for crystal determination from PXRD pattern, implemented in MS modeling version 4.4 (Accelrys Inc.). I performed Pawley refinement to optimize the lattice parameters iteratively until the R_p and R_{WP} values converge. The pseudo-Voigt profile function

was used for whole profile fitting and instrument geometry function as Bragg–Brentano was used during the refinement processes.

The porosity of HTP-BDA COF was investigated by conducting nitrogen gas (N_2) adsorption at 77 K (Figures 3.5b and c). The sharp uptake below $P/P_0 = 0.1$ justified the microporous character of the COF. The Brunauer–Emmett–Teller (BET) surface area was calculated as high as $1045 \text{ m}^2 \text{ g}^{-1}$. I evaluated the pore size distributions by using the nonlocal density function theory (NLDF) method. The HTP-BDA COF has two main peaks centered at 12.7 and 15.6 Å, confirming the COF is of dual-pore structure with a small pore size of 12.7 Å and a big pore size of 15.6 Å. The dual-pore structure, expecting based on the geometry feature of HTP-CHO, was corroborated by the pore size distribution concluded from the N_2 sorption result.

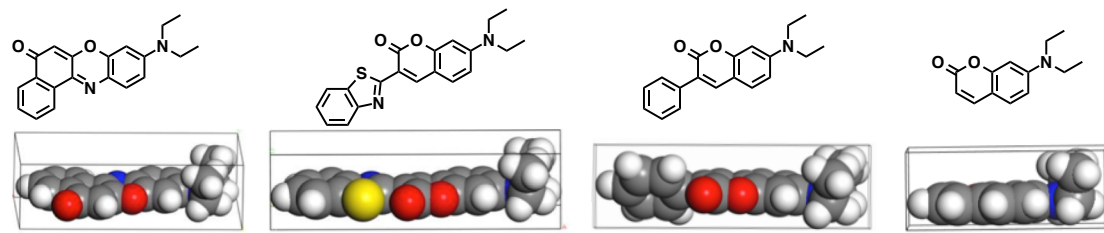
3.2.3 Selective Adsorption in Solution

Nile Red (NR) and Coumarin 6 (C6) are two typical natural laser dyes of very similar structures: they both are conjugated planar molecules and vary only on dimension (Figure 3.1b and Table 3.2). Therefore, they are ideal probes for size exclusion and I can take advantage of their vision color at the same time. The pore sizes of HTP-BDA COF are 12.7 and 15.6 Å. The big pore is smaller than the dimension of C6 (16.8 Å) but bigger than that of NR (15.0 Å). Thus HTP-BDA COF is assumed able to sieve C6 from NR by permitting NR entering into the 15.6 Å channels but deny the entrance of C6.

I started the discrimination study by immersing 5 mg HTP-BDA COF into 3 mL dye mixture solution of equimolar NR and C6. Within 10 min, the NR absorption peak at 528 nm dropped significantly, indicating the rapid uptake of NR by HTP-BDA COF (Figure 3.6 a). Since the signal at 466 nm is the absorbance combination of both NR and C6, it is necessary to exclude the effect of NR before calculating the concentrate variation of C6. After eliminating the effect caused by NR according to the Beer–Lambert law carefully, I found the decay at 446 nm was resulted from NR and there was no absorption variation for C6 (Figure 3.7). The adsorption experiment in NR and C6 mixture solution demonstrates, HTP-BDA COF is able to discriminate

NR from by C6 by selective adsorption and the discriminative dimension difference is 1.8 Å.

Table 3.2 Molecule dimension of the dye molecules was estimated from the solid-state structures.



Dye molecules	Dimensions (Å)
NR	15.0×7.8×4.5
C6	16.8×7.3×4.3
DAPC	15.5×7.7×4.7
C466	11.0×7.2×4.3

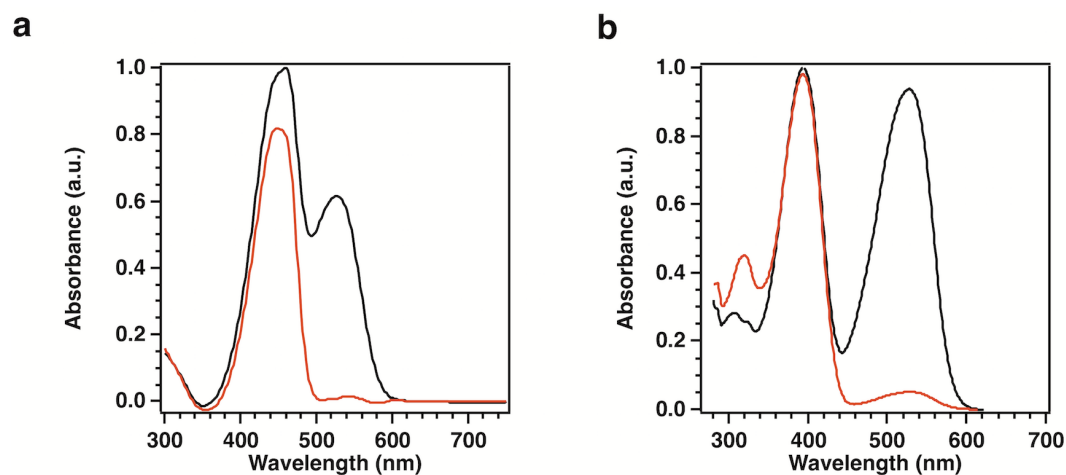


Figure 3.6 Separation and adsorption performance in solutions. UV-vis spectra before (black) and after (red) HTP-BDA COF adsorption. (a) NR:C6 = 1:1 (mol: mol, total 0.025 mM), (b) NR:DAPC = 1:1 (mol: mol, total 0.025 mM).

I further explored the discrimination ability of HTP-BDA COF by replacing C6 to 7-(diethylamino)-3-phenylcoumarin (DAPC) that was more similar dimensionally to

NR (Figure 3.1b and Table 3.2). Adsorption experiment was conducted in DAPC : NR = 1:1 mixture (Figure 3.6b) and the successful separation between DAPC and NR was realized by the selective adsorption of NR over DAPC. The selective adsorption behaviors confirmed HTP-BDA COFs as rigorous separation media with dimension difference tolerance narrowing down to 0.5 Å.

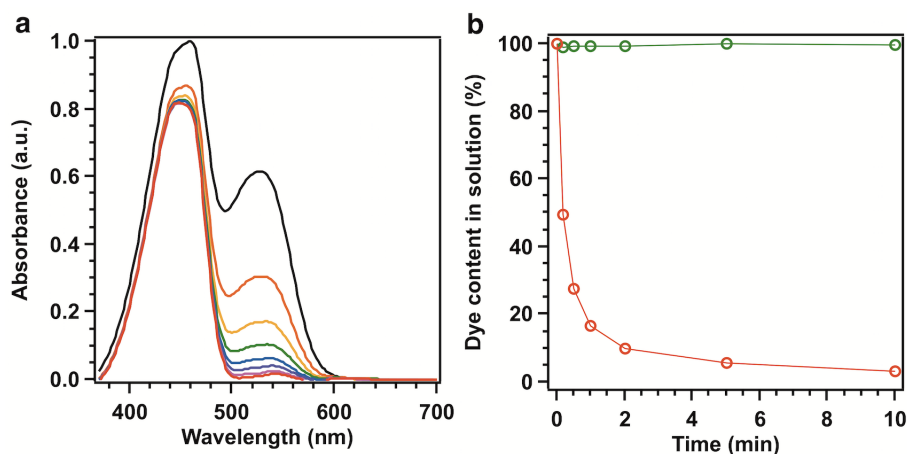


Figure 3.7 (a) UV-vis spectra of mixture solution with NR : C6 (mol : mol) = 1:1 monitored along time in the existence of HTP-BDA COF (original in black, 10 s in orange, 30 s in yellow, 1 min in green, 2 min in blue, 5 min in purple, 10 min in pink, and 12 h in red). (b) Resulting adsorption efficiency of C6 (green) and NR (red) (%).

3.2.4 Column Chromatographic Separation

Chromatographic column separation experiment was conducted in a 1.5 cm-high HTP-BDA COF column made by filling 30 mg HTP-BDA COF into a Pasteur pipette. Then DAPC and NR equal molar mixture (1:1, 0.02 mmol) in THF was introduced into the COF column. The separation was not only observable by the naked eye (Figures 3.8a-e) but was also confirmed by UV-vis spectra of the effluent (Figure 3.8f). DAPC transported through the column immediately—started from 4 min after the mixture introduce and ended at 7 min. As for NR, the signal appeared at 50 min, and then gradually flew out until 160 min. The 43 min time interval implies HTP-BDA COF is capable to separate the two-dye mixture into two 100% purity single compounds and the dimension difference between the two compounds is 0.5 Å.

Furthermore, the rapid escape of DAPC and long retention time of NR demonstrate the adsorption behaviors of the two compounds are definitely distinct within the HTP-BDA COF column.

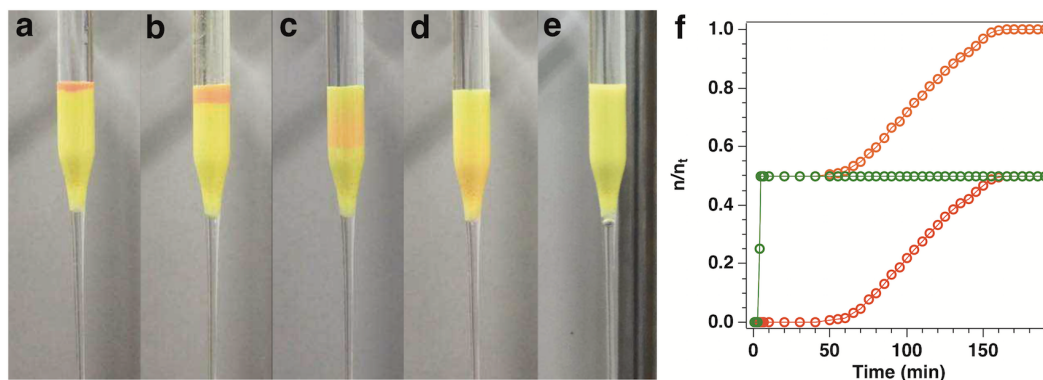


Figure 3.8 Column chromatographic separation. Photographs of the HTP-BDA COF-filled column after DAPC and NR equimolar mixture loading for (a) 0 min, (b) 4 min, (c) 30min, (d) 90 min, and (e) 180 min. (f) The accumulated flow-out amount of DAPC and NR (orange), DAPC (green) and NR (red).

3.3 Discussion

For the discrimination phenomenon of HTP-BDA COF, I assumed it results from the size exclusive behavior of COF channels. The discrete channels only allow the entrance of molecules whose dimension is smaller than the pore size and strictly deny the access of larger guests. To confirm the assumption, I need to prove (1) the separation resulted from size exclusion instead of dynamic adsorption competition between the dyes or diffusion difference within COF channels; (2) the discrimination originates from the selective uptake of the 15.6 Å COF channels.

Investigation was firstly processed to find out whether the selective adsorption resulted from dynamic competition between two compounds. I conducted adsorption experiments by immersing HTP-BDA COF in NR, C6 and DAPC single-compound solutions and monitored the concentrate change by UV spectra. The adsorption results showed that the concentration of NR solution decreased dramatically from 100 to 5.7% (Figures 3.9a and 3.10) while there was no content change of C6 and DAPC solution

during the same period (Figures 3.9b, c and 3.10). Such observation indicates that the separations of NR/C6 and NR/DAPC are not dynamic competition process and HTP-BDA COF is indeed adsorption mute to C6 and DAPC thermodynamically. The dimension depending adsorption was further confirmed by the uptake of HTP-BDA COF to 7-(diethylamino) coumarin (C466, $11.0 \times 7.2 \times 4.3$ Å, Table 3.2). The obvious fade of C466 main adsorption peak at 369 nm demonstrated the irrefutable uptake behavior of HTP-BDA COF to C466 (Figure 3.9d). C466 is the same structure fragment of C6 and DAPC. The uptake of C466 by HTP-BDA COF indicates the adsorption denies of C6 and DAPC is not resulting from specific structure features but dimension. The adsorption access to HTP-BDA COF switches from off to on when the target molecule dimension decreases from C6 and DAPC to C466. Thus, the discrimination ability of HTP-BDA COF is a result of thermodynamically size exclusion rather than dynamic competition.

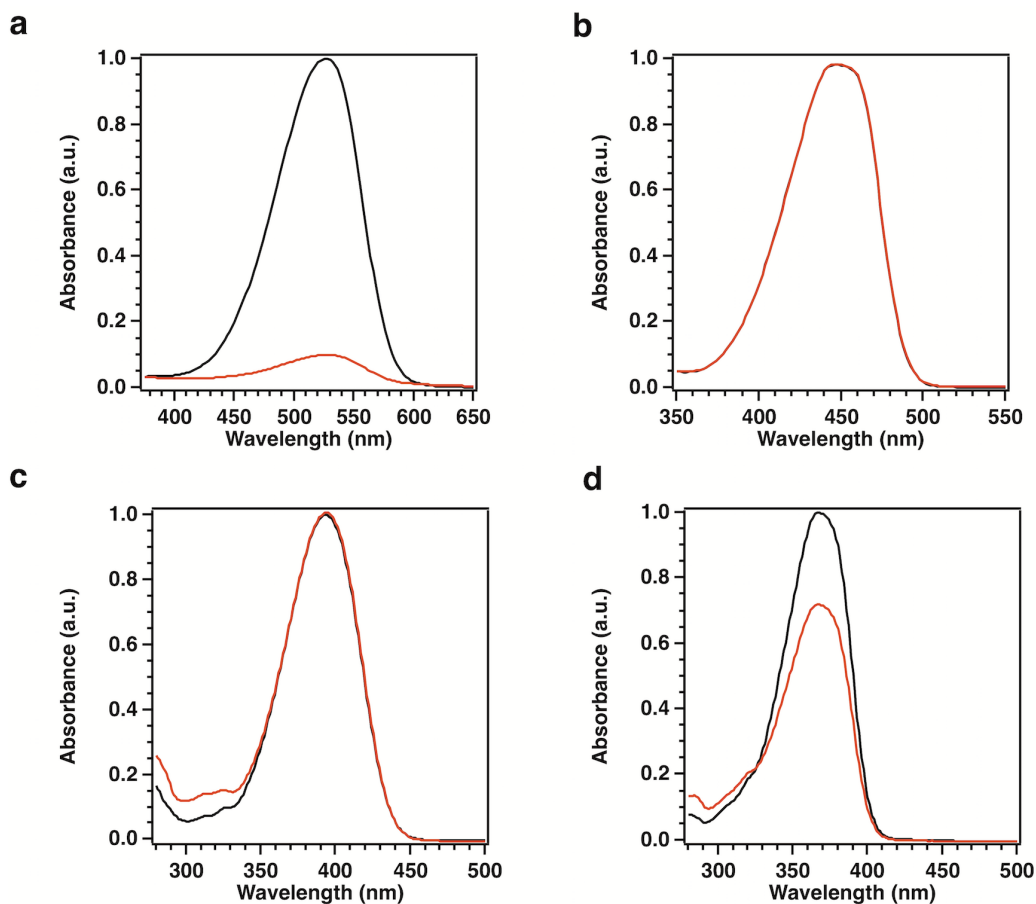


Figure 3.9 UV-vis spectra before (black) and after (red) HTP-BDA COF adsorption.

(a) NR (0.025 mM), (b) C6 (0.025 mM), (c) DAPC (0.025 mM), and (d) C466 (0.025 mM).

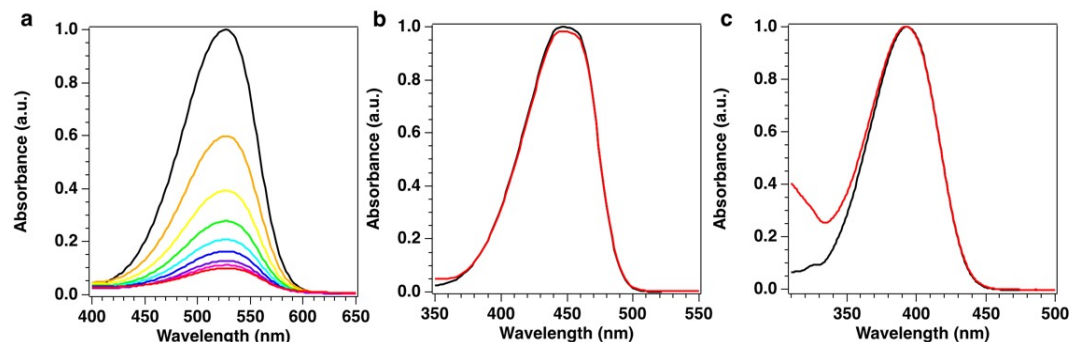


Figure 3.10 UV-vis spectra of single-compound dye solution before (black) and after (red) adsorbed by HTP-BDA COF for 12 h (a) NR, (b) C6, and (c) DAPC. For NR, original in black, 10s in orange, 30s in yellow, 1min in green, 2 min in blue, 5 min in purple, 10 min in pink, and 12 h in red.

It is reasonable to wonder whether the separation results from the different in-pore diffusion: the interaction is too weak to prevent C6 and DAPC leaking out the channels while t NR was tightly bonded within channels. I deposited the four guest molecules into the 15.7 Å channels directly and calculated the binding energies of all dyes bound along the pore wall (Table 3.3).

Specifically, dye molecules were randomly inserted into the channel using the Kick3 algorithm that allows for random conformations of flexible molecules to be placed. 500 random starting geometries were generated for each dye molecule and optimized using self-consistent charge density functional tight-binding, as implemented in the DFTB package version 1.3. All atoms were described using the mio-0-1 parameter set and UFF dispersion. DFTB has been proved the most reliable tool for COF structural and energetic simulation and its reliability is confirmed by negligible difference between experimental data and simulation results.³³⁻³⁶ In this study, basing on the DFTB model, optimized geometries were sorted by final energy and the lowest energy geometries were manually inspected to identify their binding

geometry. To confirm the completeness of the stochastic search, binding geometries of interest (e.g. along the channel wall) were manually generated and optimized, in each case producing higher energies than the previously identified structures.

The HTP-BDA COF presents distinct adsorption behaviors to NR and DAPC—it can adsorb NR rapidly from solution but keep intact in DAPC solution. However, the bonding energy difference between NR and DAPC is as small as 1 kcal mol⁻¹. Basing on same calculation model, the bond energy for C466 is 6.5 kcal mol⁻¹ smaller than that of NR but the HTP-BDA COF shows similar obvious adsorption to both NR and C466 demonstrated by the obvious UV spectra decay. Therefore, the bond energy difference cannot be responsible to the separation phenomenon and C6 and DAPC are not escape from the channels but indeed entrance deny by the channels.

Table 3.3 The binding energies of all dyes bound along the pore wall.

Dye molecules	Binding energies (kcal mol ⁻¹)
Nile red	-34.6
DAPC	-33.6
C466	-27.9
C6	-40.6

Based on the dimension match between the COF pores and NR molecule, I assumed that the adsorption sites of NR are the 15.6 Å COF nanochannels and it is the selective adsorption of the 15.6 Å channels that take responsibility to the discrimination phenomenon. To confirm the assumption, N₂ sorption measurement was conducted to the fully NR-loaded HTP-BDA COF. Firstly, I immersed 5 mg HTP-BDA COF into NR THF solutions of varied concentrations (Figure 3.11a) to monitor the thermodynamic adsorption process. When NR concentration varied from 0.006 to 0.19 mM, the adsorption efficiency of HTP-BDA COF slightly decreased from 96.1% to 84.4% with a almost 15-fold improvement of dye uptake amount from 1.1 to 15.2 mg g⁻¹. This phenomenon suggests that the adsorption sites available to

NR are not fully occupied in diluted dye solution and are gradually covered by NR molecules while the dye solution concentrating gradually. Further increasing NR concentration from 0.19 to 0.55 mM, the uptake efficiency of HTP-BDA COF fell down sharply from 89.0% to 34.7% with an almost constant uptake amount (30 to 36 mg g^{-1}), meaning the uptake reached the limitation in the concentrated dye solution and all the adsorption sites were fully occupied by NR. I isolated HTP-BDA COF from concentrate NR solution (0.55 mM) and took it for N_2 sorption measurement. After NR adsorption, the BET surface area largely decayed compared to that of the original COF and the 15.6 Å pores totally disappeared (Figures 3.11b and c). The N_2 sorption results demonstrate that 15.0 Å NR molecules indeed accommodate into the 15.6 Å channels of HTP-BDA COF. The discrimination behavior of HTP-BDA COF is really resulted from the selective adsorption of the 15.6 Å channels basing on dimension match. Furthermore, Soxhlet in THF could regenerate the NR-loaded COF and its porosity and crystallinity could maintain for five cycles (Figure 3.12).

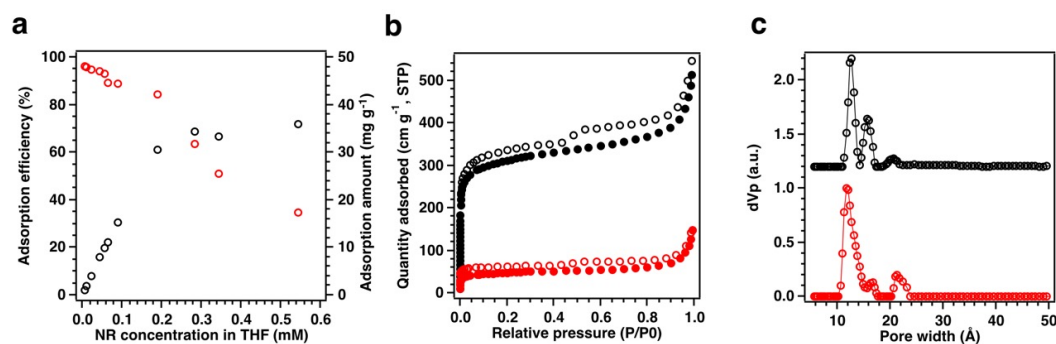


Figure 3.11 Adsorption thermodynamic study. (a) Adsorption efficiency and capacity of HTP-BDA COF in NR solution of varied concentrations. (b) Nitrogen-sorption isotherm curves of HTP-BDA COF before (black) and after (red) NR adsorption in 0.55 mM NR solution measured at 77 K. (c) Profiles of the pore-size distribution of HTP-BDA COF before (black) and after (red) NR adsorption in 0.55 mM NR solution.

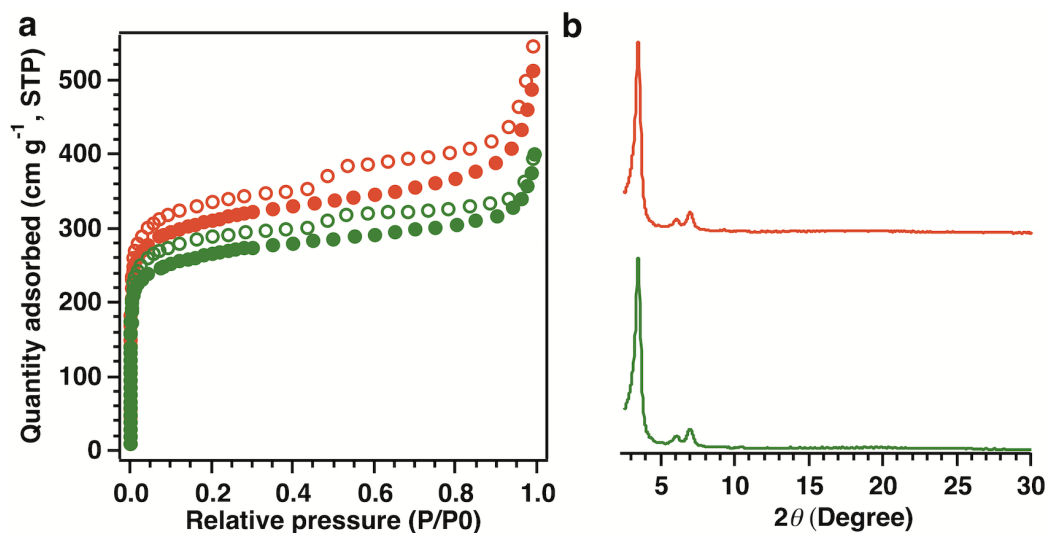


Figure 3.12 (a) Nitrogen sorption isotherm profiles of HTP-BDA COF (red: fresh, green: regenerated from 0.55 mM NR solution after 5 adsorption cycles). The filled circles represent adsorption and the open circles represent desorption. (b) PXRD patterns of HTP-BDA COF after each cycle (red: fresh, green: regenerated from 0.0250 mM NR solution after 5 adsorption cycles).

Therefore, it is safe to conclude the discrimination between NR and C6/DAPC is originated from the size exclusion behavior of the 15.6 Å COF channels. The dimension of NR is beneath the scale of HTP-BDA COF pore and thus NR freely flows into channels; while the C6 and DAPC are too bulky and COF channels deny the entrance of C6 and DAPC. The selective adsorption with dimension difference as small as 0.5 Å is thus resulted. For the column experiment, the diffusion of trapped NR within COF channels is depressed by van der Waals force from channel walls and the slow creeping diffuse within channels leads to the long retention time of NR. As for DAPC, it flows through HTP-BDA COF surface rapidly and a short retention time is thus resulted.

3.4. Conclusion

In summary, by employing dye probes, I explored the discrimination capability of microporous HTP-BDA COF towards guest molecules by solution adsorption and chromatographic column experiment. The HTP-BDA COF was able to distinguish guest molecules with dimension difference of 0.5 Å. By single compound adsorption

investigation, bonding energy calculation and gas sorption measurement, I confirmed that the molecular discrimination phenomenon originated from the size exclusive adsorption behavior of the 1D nanochannels. The discrete pore structure enabled HTP-BDA COF to uptake or exclude guest basing on dimension match between the pore size and guest molecule scale. The work for the first time demonstrates that COFs offer a predesignable platform for molecular discrimination, especially for large and neutral molecules difficult to be accurately separated by other porous materials.

3.5 Experimental Sections

3.5.1 Methods

JEOL models JNM-LA400 NMR spectrometers were used to measure the ^1H nuclear magnetic resonance (NMR) spectra. Using the solvent residual proton peaks as reference, the chemical shifts (δ in ppm) of compounds are confirmed. A JASCO model FT-IR-6100 infrared spectrometer was used to determine the Fourier transform infrared (FT-IR) spectra. The Rigaku model RINT Ultima III diffractometer was used to confirm the crystallinity character by the Powder X-ray diffraction (PXRD) data. Detailly, the sample powder was deposited on glass substrate and the measure starts from $2\theta = 2.5^\circ$ up to 30° with 0.02° increment. At 77 K created by liquid nitrogen, a Micromeritics Instrument Corporation model 3Flex surface characterization analyzer was used to measure the nitrogen sorption isotherms. The specific surface areas and the pore distribution was confirmed by the Brunauer-Emmett-Teller (BET) method and the non-local density functional theory (NLDFT) model, respectively. A Bel Japan Inc. model BELSORP-mini II analyzer was used to confirm the carbon dioxide sorption isotherms. For the isotherm measurements, all the samples were degassed in vacuum at 120°C for more than 10 h. A Mettler-Toledo model TGA/SDTA851e was used to measure the TGA curves in nitrogen atmosphere at a rate of $10^\circ\text{C min}^{-1}$. The JEOL model JSM-6700 was used for field-emission scanning electron microscopy (FE-SEM). The operation is conducted at an accelerating voltage of 5.0 kV. To improved sample conductivity, before measure, the sample was coated by gold after drop-casting its acetone suspension on mica substrate.

Reflex, a software package to determine the crystal XRD pattern, was used for Molecular modeling and Pawley refinement. The simulation work was implemented in Material Studio modeling version 8 (Accelrys Inc.). The crystalline structures of COFs were determined using the density-functional tight-binding (DFTB) method including Lennard-Jones (LJ) dispersion. The calculations were carried out with the DFTB program package version 1.2. DFTB is an approximate density functional theory method based on the tight binding approach and utilizes an optimized minimal LCAO Slater-type all-valence basis set in combination with a two-center approximation for Hamiltonian matrix elements. The Coulombic interaction between partial atomic charges was determined using the self-consistent charge (SCC) formalism. Lennard-Jones type dispersion was employed in all calculations to describe van der Waals (vdW) and π -stacking interactions with starting structures created by AuToGraFS and pre-optimized using a topology-preserving force field were used to optimize the monolayer and were further extended to layered frameworks with different stacking modes. The lattice dimensions were optimized simultaneously with the geometry. Standard DFTB parameters for X-Y element pair (X, Y = C, H and N) interactions were employed from the mio-0-1 set10. I performed Pawley refinement to optimize the lattice parameters iteratively until the R_p and R_{WP} values converge. The pseudo-Voigt profile function was used for whole profile fitting and instrument geometry function as Bragg–Brentano was used during the refinement processes. The final unit cell parameters and refinement factors are $a = b = 29.1211 \text{ \AA}$, $c = 3.8840 \text{ \AA}$, $\alpha = \beta = 90^\circ$, $\gamma = 120^\circ$, $R_{WP} = 5.61\%$ and $R_p = 3.90\%$, respectively.

Separation and adsorption studies in dye solutions. HTP-BDA COF (5 mg) was transformed into a 10 mL glass vial and then a dye solution (3 mL) was added. The specific dye concentration was listed in Table 3.4. The mixture was stirred for a certain time period and 1.5 mL of the suspension were taken out using a syringe and filtered immediately by a Cosmonice 0.45 μm membrane filter. The residual concentration of the dye solution was determined by UV-vis spectroscopy. The molar extinction coefficients (ϵ in units of M^{-1}) were determined for NR (38,075 at $\lambda_{\text{max}} =$

528 nm, 7307 at $\lambda = 466$ nm), C6 (58,578 at $\lambda_{\max} = 466$ nm), DAPC (36,158 at $\lambda_{\max} = 393$ nm), and C466 (25,600 at $\lambda_{\max} = 367$ nm) by experiment.

Table 3.4 Dye concentration in mixture and single-compound solutions

Dye solution	C_1 (mM)	C_2 (mM)	C_{total} (mM)
$C_1:C_2 = \text{NR}:C6 = 1:1$	0.0125	0.0125	0.0250
$C_1:C_2 = \text{NR}:DAPC = 1:1$	0.0125	0.0125	0.0250
$C_1 = \text{NR}$	0.0250	0.0000	0.0250
$C_1 = C6$	0.0250	0.0000	0.0250
$C_1 = DAPC$	0.0250	0.0000	0.0250
$C_1 = C466$	0.0250	0.0000	0.0250

Column chromatographic separation. The Pasteur pipette ($\varnothing 7$ mm, 229 mm) was filled with 30 mg HTP-BDA COF (1.5 cm in height) as a chromatographic column using THF as mobile phase. The THF solution of mixed NR and DAPC (1:1 in mole, total of 0.02 mmol) and then pure THF passed through the chromatographic column. The UV-vis spectra of effluents were examined along with time to confirm the column separation capability.

NR adsorption thermodynamic study. HTP-BDA COF (5 mg) was transformed into a 10 mL glass vial and then NR solution of varied concentration was added. The mixture was kept stirring and 1.5 mL of the suspension were taken after 12 h via syringe and filtered immediately by a Cosmonice 0.45 μm membrane filter. The residual concentration of the dye solution was determined by UV-vis spectroscopy. The molar extinction coefficients (ϵ in units of M^{-1}) was determined for NR as 38,075 at $\lambda_{\max} = 528$ nm.

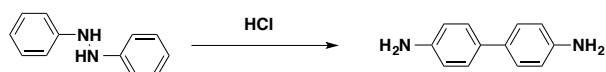
NR adsorption efficiency (Ads eff): $\text{Ads eff} = 100 \times (C_0 - C_t) / C_0$. Where C_0 (mM) and C_t (mM) is the initial and residual concentration of NR in the stock solution and filtrate, respectively.

NR adsorption amount (q_t): $q_t = ((C_0 - C_t)M_w) / m$. Where q_t (mg g^{-1}) is the

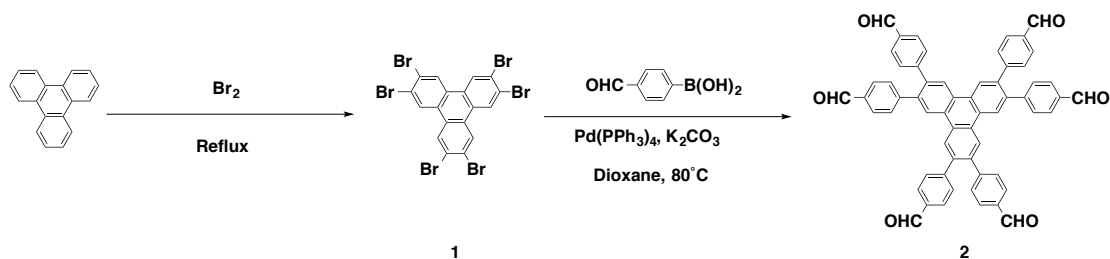
amount of NR adsorbed by per gram of HTP-BDA COF at time t (min). C_0 (mM) and C_t (mM) is the initial and residual concentration of NR in the pristine solution and filtrate, respectively. M_W (g mol^{-1}) is the molar mass of NR and m (g) is the mass of HTP-BDA COF.

N_2 sorption measurement of NR loaded HTP-BDA COF. 20 mg HTP-BDA COF was immersed and kept stirring in 12 mL 0.55 mM NR solution for 12 h. The NR loaded sample was isolated by filter, rinsed by 20 mL hexane and dried in vacuum.

3.5.2 Synthetic Procedures



4,4'-diaminobiphenyl.⁴⁵ Hydrazobenzene (5.0 g, 27.1 mmol) was dissolved into EtOH/water (3:1, 200 mL) and the system was cooled to 0 °C. Concentrated hydrochloric acid (20 mL, 57.4 mmol) was diluted by EtOH/water (11:4, 300 mL) and added the diluted acid into the hydrazobenzene solution at 0 °C. Let the system stir for 24 h and gradually warm to room temperature. Evaporated EtOH and cooled the system to get white crystal. The crystal was dissolved into 200 mL water and the solution was neutralized by saturated sodium bicarbonate solution. Extracted the aqueous solution by dichloromethane (3×300 mL). The organic part was dried over sodium magnesium and evaporated to obtained brown solid. The brown solid was recrystallized in water and the final product was collected as white crystal (59% yield). ^1H NMR (400MHz, CDCl_3 , 25 °C): δ (ppm) 7.36 (4H, d, $J = 8.4$ Hz, ArH), 6.75 (4H, d, $J = 8.8$ Hz, ArH), 3.67 (4H, s, $-\text{NH}_2$).



2,3,6,7,10,11-Hexabromotriphenylene (1).⁴⁶ Triphenylene (1 g, 2.4 mmol) was dissolved into nitrobenzene (40 mL) in accompany of iron powder (80 mg). Bromine

(3 mL, 58 mmol) was added slowly into the system over 5 min. The system was kept still overnight and then heated to reflux for 2 h. The system was cooled down to room temperature and added diethyl ether (100 mL) into it. The black solid was filtered out and recrystallized from 1,2-dichlorobenzene. The final product is white crystal which is insoluble in common solvent. Take the sample directly into next step reaction without further purification (90% yield).

2,3,6,7,10,11-hexakis (4-formylphenyl) triphenylene (HTP-CHO, 2) A mixture of 2,3,6,7,10,11-hexabromotriphenylene (140.2 mg, 0.2 mmol), tetrakis(triphenylphosphine)palladium(0) (138.6 mg, 0.12 mmol), K₂CO₃ (248.4 mg, 1.8 mmol), 4-formylphenylboronic acid (270 mg, 1.8 mmol), and toluene/methanol/dioxane (20 mL, 2/1/1 by vol.) in a 50 mL two-necked round bottle flask was purged with Ar for 30 minutes and stirred under reflux for 48h. After cooling to room temperature, the solvent was evaporated and extracted the residual by CHCl₃, washed it with water and brine and dried it over anhydrous MgSO₄. The solvent was removed under vacuum and purified the resulting solid by column chromatography (silica gel, CHCl₃: AcOEt = 19:1) to give HTP-CHO as white solid (82% yield). ¹H NMR (400 MHz, CDCl₃, 25 °C): δ (ppm) 10.021 (s, 6H, -CHO), 8.753 (s, 6H, ArH), 7.85 (d, 12H, J = 8.2 Hz, ArH), 7.49 (d, 12H, J = 8.2 Hz, ArH).

HTP-BDA COF. An *o*-DCB/*n*-BuOH (0.5/0.5 mL) mixture of BDA (0.070 mmol, 13 mg) and HTP-CHO (0.023 mmol, 20 mg) in the presence of an acetic-acid catalyst (6 M, 0.1 mL) in a Pyrex tube (10 mL) was degassed via three freeze-pump-thaw cycles. The tube was flame sealed and heated at 120 °C for five days. The precipitate was centrifuged out and washed by THF. The sample was then subjected to Soxhlet extraction with THF as the solvent for one day to remove the trapped guest molecules. The powder was collected and dried at 120 °C under vacuum overnight to produce HTP-BDA COF in an isolated yield of 84%.

3.6 References

1. Humphrey J. L. & Keller G. E. *Separation Process Technology*. (McGraw-Hill: New York, United States, 1997.)

2. Slater A. G. & Cooper A. I. Function-led design of new porous materials. *Science* **348**, 8075-8084 (2015).
3. Nugent P., *et al.* Porous materials with optimal adsorption thermodynamics and kinetics for CO₂ separation. *Nature* **495**, 80-84 (2013).
4. Alsbaiee A., Smith B. J., Xiao L., Ling Y., Helbling D. E. & Dichtel W. R. Rapid removal of organic micropollutants from water by a porous β -cyclodextrin polymer. *Nature* **529**, 190-194 (2016).
5. Cui X., *et al.* Pore chemistry and size control in hybrid porous materials for acetylene capture from ethylene. *Science* **353**, 141-144 (2016).
6. Cadiau A., Adil K., Bhatt P. M., Belmabkhout Y. & Eddaoudi M. A metal-organic framework-based splitter for separating propylene from propane. *Science* **353**, 137-140 (2016).
7. Koh D.-Y., McCool B. A., Deckman H. W. & Lively R. P. Reverse osmosis molecular differentiation of organic liquids using carbon molecular sieve membranes. *Science* **353**, 804-807 (2016).
8. Grande C. A., Gascon J., Kapteijn F. & Rodrigues A. E. Propane/propylene separation with Li-exchanged zeolite 13X. *Chem. Eng. J.* **160**, 207-214 (2010).
9. Grande C. A. & Rodrigues A. E. Propane/propylene separation by pressure swing adsorption using Zeolite 4A. *Ind. Eng. Chem. Res.* **44**, 8815-8829 (2005).
10. Lobo R. F. Introduction to the structural chemistry of zeolites. In: Auerbach S. M., Carrado K. A., Dutta P. K. (eds). *Handbook of Zeolite Science and Technology*. (Marcel Dekker: New York, 2003.)
11. Assen A. H., *et al.* Ultra-tuning of the rare-earth fcu-MOF aperture size for selective molecular exclusion of branched paraffins. *Angew. Chem. Int. Ed.* **54**, 14353-14358 (2015).
12. Côté A. P., Benin A. I., Ockwig N. W., O'Keeffe M., Matzger A. J. & Yaghi O. M. Porous, crystalline, covalent organic frameworks. *Science* **310**, 1166-1170 (2005).
13. Feng X., Ding X. & Jiang D. Covalent organic frameworks. *Chem. Soc. Rev.* **41**,

- 6010-6022 (2012).
14. Ding S. Y. & Wang W. Covalent organic frameworks (COFs): from design to applications. *Chem. Soc. Rev.* **42**, 548-568 (2013).
 15. Dogru M. & Bein T. On the road towards electroactive covalent organic frameworks. *Chem. Commun.* **50**, 5531-5546 (2014).
 16. Jiang J., Zhao Y. & Yaghi O.M. Covalent chemistry beyond molecules. *J. Am. Chem. Soc.* **138**, 3255-3265 (2016).
 17. Huang N., Wang P. & Jiang D. Covalent organic frameworks: a materials platform for structural and functional designs. *Nat. Rev. Mater.* **1**, 16068 (2016).
 18. Waller P. J., Gandara F. & Yaghi O. M. Chemistry of covalent organic frameworks. *Acc. Chem. Res.* **48**, 3053-3063 (2015).
 19. DeBlase C. R. & Dichtel W. R. Moving beyond boron: the emergence of new linkage chemistries in covalent organic frameworks. *Macromolecules* **49**, 5297-5305 (2016).
 20. Xu H., Gao J. & Jiang D. L. Stable, crystalline, porous, covalent organic frameworks as a platform for chiral organocatalysts. *Nat. Chem.* **7**, 905-912 (2015).
 21. Xu H., *et al.* Catalytic covalent organic frameworks via pore surface engineering. *Chem. Commun.* **50**, 1292-1294 (2014).
 22. Wang X., Han X., Zhang J., Wu X., Liu Y. & Cui Y. Homochiral 2D porous covalent organic frameworks for heterogeneous asymmetric catalysis. *J. Am. Chem. Soc.* **138**, 12332-12335 (2016).
 23. Xu H. -S., Ding S. -Y., An W. -K., Wu H. & Wang W. Constructing crystalline covalent organic frameworks from chiral building blocks. *J. Am. Chem. Soc.* **138**, 11489-11492 (2016).
 24. Huang N., Chen X., Krishna R. & Jiang D. Two-dimensional covalent organic frameworks for carbon dioxide capture through channel-wall functionalization. *Angew. Chem. Int. Ed.* **54**, 2986-2990 (2015).
 25. Huang N., Krishna R. & Jiang D. Tailor-made pore surface engineering in

- covalent organic frameworks: systematic functionalization for performance screening. *J. Am. Chem. Soc.* **137**, 7079-7082 (2015).
26. Doonan C. J., Tranchemontagne D. J., Glover T. G., Hunt J. R. & Yaghi O. M. Exceptional ammonia uptake by a covalent organic framework. *Nat. Chem.* **2**, 235-238 (2010).
 27. Dalapati S., Jin E., Addicoat M., Heine T. & Jiang D. Highly emissive covalent organic frameworks. *J. Am. Chem. Soc.* **138**, 5797-5800 (2016).
 28. Ding S. Y., *et al.* Thioether-based fluorescent covalent organic framework for selective detection and facile removal of mercury(II). *J. Am. Chem. Soc.* **138**, 3031-3037 (2016).
 29. Chandra S., *et al.* Phosphoric acid loaded azo (-N=N-) based covalent organic framework for proton conduction. *J. Am. Chem. Soc.* **136**, 6570-6573 (2014).
 30. Xu H., Tao S. & Jiang D. Proton conduction in crystalline and porous covalent organic frameworks. *Nat. Mater.* **15**, 722-726 (2016).
 31. Huang N., Zhai L., Xu H. & Jiang D. Stable covalent organic frameworks for exceptional mercury removal from aqueous Solutions. *J. Am. Chem. Soc.* **139**, 2428-2434 (2017).
 32. Sun Q., *et al.* Postsynthetically modified covalent organic frameworks for efficient and effective mercury removal. *J. Am. Chem. Soc.* **139**, 2786-2793 (2017).
 33. Dogru M., *et al.* A photoconductive thienothiophene-based covalent organic framework showing charge transfer towards included fullerene. *Angew. Chem. Int. Ed.* **52**, 2920-2924 (2013).
 34. Guo J., *et al.* Conjugated organic framework with three-dimensionally ordered stable structure and delocalized π clouds. *Nat. Commun.* **4**, 2736 (2013).
 35. Chen L., *et al.* Photoelectric covalent organic frameworks: converting open lattices into ordered donor-acceptor heterojunctions. *J. Am. Chem. Soc.* **136**, 9806-9809 (2014).
 36. Jin S., *et al.* Charge dynamics in a donor-acceptor covalent organic framework

- with periodically ordered bicontinuous heterojunctions. *Angew. Chem. Int. Ed.* **52**, 2017-2021 (2013).
37. Xu F., *et al.* Radical covalent organic frameworks: a general strategy to immobilize open-accessible polyradicals for high-performance capacitive energy storage. *Angew. Chem. Int. Ed.* **54**, 6814-6818 (2015).
 38. DeBlase C. R., Silberstein K. E., Truong T. T., Abruna H. D. & Dichtel W. R. β -Ketoenamine-linked covalent organic frameworks capable of pseudocapacitive energy storage. *J. Am. Chem. Soc.* **135**, 16821-16824 (2013).
 39. Zhao X., Bu X., Wu T., Zheng S. -T., Wang L. & Feng P. Selective anion exchange with nanogated isoreticular positive metal-organic frameworks. *Nat. Commun.* **4**, 2344 (2013).
 40. Zhao X., *et al.* Framework cationization by preemptive coordination of open metal sites for anion-exchange encapsulation of nucleotides and coenzymes. *Angew. Chem. Int. Ed.* **55**, 2768-2772 (2016).
 41. Dalapati S., *et al.* Rational design of crystalline supermicroporous covalent organic frameworks with triangular topologies. *Nat. Commun.* **6**, 7786 (2015).
 42. Xu S. -Q., Zhan T. -G., Wen Q., Pang Z. -F. & Zhao X. Diversity of covalent organic frameworks (COFs): A 2D COF containing two kinds of triangular micropores of different sizes. *ACS Macro Lett.* **5**, 99-102 (2016).
 43. Alahakoon S. B., Thompson C. M., Nguyen A. X., Occhialini G., McCandless G. T. & Smaldone R. A. An azine-linked hexaphenylbenzene based covalent organic framework. *Chem. Comm.* **52**, 2843-2845 (2016).
 44. Ascherl L., *et al.* Molecular docking sites designed for the generation of highly crystalline covalent organic frameworks. *Nat. Chem.* **8**, 310-316 (2016).
 45. Clegg J. *et al.* A stimuli responsive system of self-assembled anionbinding $\text{Fe}_4\text{L}_6^{8+}$ cages. *Chem. Sci.* **4**, 68-76 (2013).
 46. Breslow R., Jaun B., Kluttz R. Q., Xia C.-z. Ground state π -electron triplet molecules of potential use in the synthesis of organic ferromagnets. *Tetrahedron* **38**, 863-867 (1982).

**Chapter 4. Iodine Capture in Stable,
Crystalline, Mesoporous Covalent Organic
Frameworks**

Abstract Iodine, released as a volatile fission product, is becoming an inevitable environment and health threat associated with the nuclear power industry. Different types of microporous materials have been intensively studied for the removal of iodine. However, microporous materials are usually limited in uptake capacity and efficiency. Herein I report the development of mesoporous materials as alternate porous media for iodine removal and demonstrate the exceptional capture of iodine with crystalline mesoporous covalent organic frameworks (COFs). The COFs are designed to have stable imine-linked skeletons, hold mesopores with pore size of 2.2 and 3.3 nm, and exhibit large pore volumes of 1.0 and 1.3 cm³ g⁻¹. Notably, the mesopores are entirely accessible to iodine, leading to a full accommodation of iodine within the nanochannels. Consequently, the COFs exhibit exceptional capacity as high as 6.26 g g⁻¹, which is far superior to the state-of-the-art microporous materials. Together with the cycle performance, the results demonstrate that mesoporous COFs offer a new platform to cope with volatile fission wastes in an efficient and recyclable way.

4.1 Introduction

The desperate of alternative sources to fossil energy promotes the development of nuclear energy. As a major volatile nuclear waste, iodine (^{129}I) bears radioactive half-life as long as 15.7 million years and its pollution to the ecosystem is permanent if once released. Unfortunately, radioiodine released from Chernobyl and Mayak has resulted in an increase in the incidence of thyroid cancer in the former Soviet Union.¹ Thus the safe handle of radioactive iodine is vital issue for nuclear energy development. Silver-based absorbent is widely researched as the most successful chemical absorbents for iodine; however, the difficult regeneration and high cost make silver absorbents not an economic choice to the industrial application.²⁻⁵ Chalcogen aerogels are also developed for iodine capture basing on the hard/soft acid-base principle—using chalcogen as soft Lewis base to trap the soft Lewis acid iodine.⁶⁻⁹ However, the inevitable chemical reactions render the chalcogen-based absorbents difficult to be recycled. Similar mechanism is also applied between nonporous nitrogen-rich polymer and iodine which also suffers from the unsatisfied cycle performance.¹⁰

Inspired by the boom of porous material research, the development of iodine physical adsorbents garners much research. 350 K and ambient pressure is the typical nuclear-fuel reprocessing condition and under this condition iodine vaporizes directly from solid state and diffuse within porous adsorbents. After cooling down, iodine vapor turns back to solid state and thus trapped within the porous adsorbents. Thus the iodine loading capacity is determined by the in-pore vapor diffusion and all the pore space should be fully occupied by iodine in the saturated state. The theoretical iodine uptake capacity is calculated as the density of solid iodine multiplies the porosity of the adsorbents. For the porous adsorbents, high pore volume endows the adsorbents with large potential capture capacity; the physical adsorption instinct guarantees the easy regeneration and descent recycle performance. Thus accommodating iodine physically into porous adsorbents becomes an economic and attractive approach.

Since the oxidation ability of iodine and the high working temperature (350 K)

make the adsorption conditions extremely harsh, a robust porous adsorbent is a must for the iodine removal. Active carbon and zeolites have been applied as stable adsorbents on industrial scale but are blamed for the limited adsorption capacity (only 0.1–0.28 g g⁻¹).³ Over the past two decades, pure covalent bonded porous materials including conjugated microporous polymers (CMPs)¹¹ and porous aromatic frameworks (PAFs)¹² have attracted increasing attention for iodine (¹²⁷I₂) capture because of their robust thermal stability and high porosity.¹³⁻¹⁹ However, their capacities are still very small in comparison with the theoretical values. Considering together with the fact of a relatively large molecular dimension of iodine (5.3 Å), the poor pore efficiency strongly suggests that the microporous interpenetrated networks are not the optimum for iodine removal.

Pore efficiency is determined by the diffusion behavior of iodine vapor within adsorbents. The in-pore diffusion within porous structure is influenced directly by pore characters including pore size, topology, and inter-pore connectivity.²⁰ Within micropores, the guest molecules are always under interaction from the pore walls and extra energy is required to overcome diffusion barriers.²¹ Thus the molecular diffusivity within micropores is much more sluggish in comparison with that of the free fluid state and poor dynamic behavior is resulted. Furthermore, the amorphous instinct leads CMPs and PAFs disordered interpenetrated networks containing plenty of intersections, narrow connecting channels and side pockets which are typical guest preferential locations. Once guest molecules block these sites, extra “push” is required to locate molecules elsewhere within the channels.^{22,23} Besides, the dynamic diameter of iodine is rather bulky (5.3 Å), making the micropores blocking highly possible. The blocking phenomenon may be responsible for the poor efficiency of pore space within the highly porous adsorbents.

To overcome the obstacle of limited pore accessibility, on the diffusion aspect, mesoporous adsorbents of large pore volume and uniform 1D channels are desired. Since interaction exerted by pore walls decays rapidly along the increase of molecule—pore wall distance, there is a central region in the mesopores where the

guest molecules flow freely as the bulky free fluid.²⁴ The facilitated diffusion allows the iodine molecule occupying the pore space rapidly. Uniform 1D channels without any intersections or periodic segments can avoid pore blocking and ensure the whole pore space available for guest molecules. The single crystal of organic zeolite has realized the full access of 1D nanochannels and its loading amount is almost identical to the theoretical value.²⁵

The mesoporous 1D channel topology can easily be realized by crystalline pore materials including metal-organic frameworks (MOFs) and covalent organic frameworks (COFs) but impossible for amorphous porous materials. Since the iodine rich off-gas from power plants is usually accompanied by high content moisture, the inferior water stability makes most MOFs unsatisfied for realistic application. In this study, I focused on developing crystalline mesoporous materials for the first time to challenge the bottleneck issues faced by the microporous materials and succeeded in demonstrating the exceptional uptake of iodine with crystalline mesoporous covalent organic frameworks (COFs).

COFs are a class of crystalline porous polymer that consists of periodically ordered skeletons and intrinsic polygon-type one-dimensional (1D) channels.²⁶⁻³³ The uniform 1D channels of two-dimensional (2D) COFs offer a platform for exploring pore chemistry for spatial confinement,³⁴⁻⁴⁰ mass transport,⁴¹⁻⁴⁶ and reactions.⁴⁷⁻⁵³ Especially, the predesignability of 2D COFs enables the creation of 1D channels with discrete size, specific polygon shape and precise in-pore chemical environment, leading to the synthesis of tailor-made pore structure.⁵⁴⁻⁵⁶ Herein, I reported the development of mesoporous 2D COFs with 1D large pores as an alternate porous platform for challenging the bottlenecks in iodine removal and highlighted the combined feature of capacity, efficiency and reusability finding in mesoporous COFs for iodine removal.

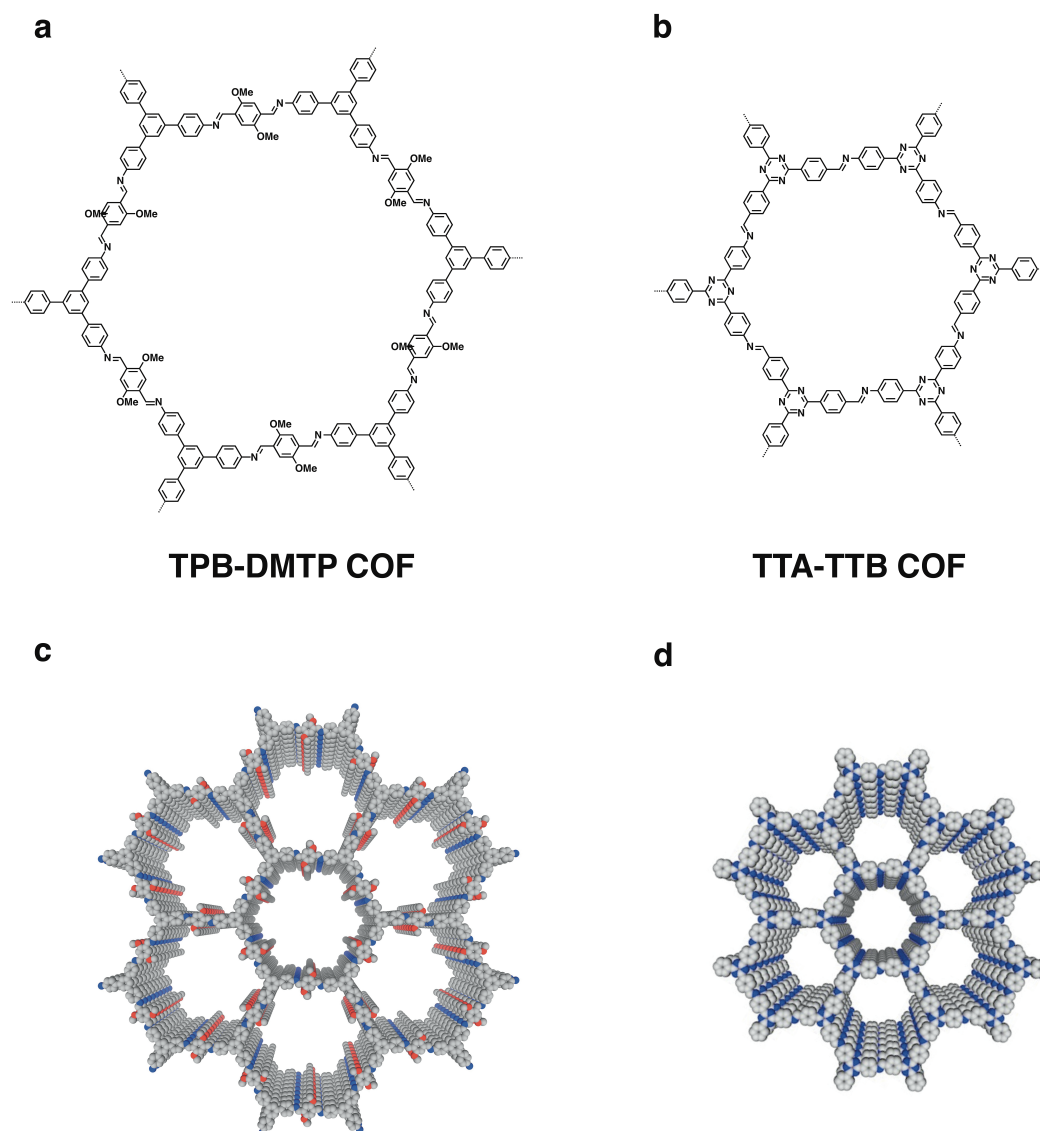


Figure 4.1 Chemical structures of (a) the TPB-DMTP COF and (b) the TTA-TTB COF. Graphic representation of layered hexagonal structure of (c) the TPB-DMTP COF and (d) the TTA-TTB COF.

I demonstrate the development of the 1D mesoporous channels as the accommodation space for iodine removal by using two typical imine-linked COFs, which are designed with the $[C_3 + C_2]$ and $[C_3 + C_3]$ topology diagrams (Figure 4.1). According to previous reports,^{48, 57, 58} the TPB-DMTP COF (Figure 4.1a) is a highly porous 2D COF with a pore size of 3.3 nm and the TTA-TTB COF (Figure 4.1b) has a pore size of 2.2 nm. The TPB-DMTP COF is chemically stable in common organic

solvents, boiling water, concentrated HCl and aqueous NaOH solution (14 M), and is thermally stable up to 400 °C under nitrogen.⁴⁸ On the other hand, the TTA-TTB COF due to the high planarity of the triazine vertices shows high crystallinity and porosity.^{57, 58}

4.2 Results and Discussion

4.2.1 COF Synthesis and Characterization

I synthesized the TPB-DMTP COF and the TTA-TTB COF by modified polycondensation reactions under solvothermal conditions in 81% and 78% isolation yields, respectively. The TPB-DMTP COF exhibited powder X-ray diffraction (PXRD) peaks at 2.76°, 4.82°, 5.60°, 7.42°, 9.70° and 25.2°, which were assigned to the (100), (110), (200), (210), (220) and (001) facets, respectively (Figure 4.2a, red curve). On the other hand, the TTA-TTB COF exhibited PXRD peaks at 4.00°, 6.98°, 8.02°, 10.56°, 14.49° and 25.84°, which were assigned to the (100), (110), (200), (210), and (001) facets, respectively (Figure 4.2b, red curve). These PXRD patterns agree well with those of reported ones.^{48, 58}

I simulated the crystal structures by using density functional tight binding (DFTB) methods including Lennard–Jones (LJ) dispersion. Among various different stacking modes, the TPB-DMTP COF assumes the eclipsed AA-stacking mode, which is the lowest in energy and yields a PXRD pattern (Figure 4.2a, blue curve) that is consistent with the experimentally observed one. Similarly, the TTA-TTB COF prefers the eclipsed AA-stacking mode that affords a PXDR profile (Figure 4.2b, blue curve) close to the experimental one. Pawley refinements generated PXRD patterns (Figure 4.2, green curves) that confirmed the assignment of the PXRD peaks of the TPB-DMTP COF and TTA-TTB COF, as shown by their negligible differences (Figure 4.2, black curves). Therefore, the TTA-TTB COF and TPB-DMTP COF possess hexagonally ordered mesoporous 1D channels (Figure 4.1c and 1d).

Specifically, the crystalline structures of COFs were determined using the density-functional tight-binding (DFTB) method including Lennard-Jones (LJ) dispersion. The calculations were carried out with the DFTB program package version

1.2. DFTB is an approximate density functional theory method based on the tight binding approach and utilizes an optimized minimal LCAO Slater-type all-valence basis set in combination with a two-center approximation for Hamiltonian matrix elements. The Coulombic interaction between partial atomic charges was determined using the self-consistent charge (SCC) formalism. Lennard-Jones type dispersion was employed in all calculations to describe van der Waals (vdW) and π -stacking interactions with starting structures created by AuToGraFS and pre-optimized using a topology-preserving force field were used to optimize the monolayer and were further extended to layered frameworks with different stacking modes. The lattice dimensions were optimized simultaneously with the geometry.

Standard DFTB parameters for X-Y element pair (X, Y = C, H and N) interactions were employed from the mio-0-1 set¹⁰. The XRD pattern simulation was performed in a software package for crystal determination from PXRD pattern, implemented in MS modeling version 4.4 (Accelrys Inc.). I performed Pawley refinement to optimize the lattice parameters iteratively until the R_P and R_{WP} values converge. The pseudo-Voigt profile function was used for whole profile fitting and instrument geometry function as Bragg–Brentano was used during the refinement processes. The final unit cell parameters and refinement factors are summarized in Table 4.1.

Table 4.1 Final unit cell parameters and refinement factors for the COFs by using Material Studio module.

COFs	a (Å)	b (Å)	c (Å)	α (°)	β (°)	γ (°)	R_{WP}	R_P
TPB-DMTP	36.21	36.21	3.85	90	90	120	6.25%	4.61%
TTA-TTB	25.41	25.41	3.61	90	90	120	5.30%	3.55%

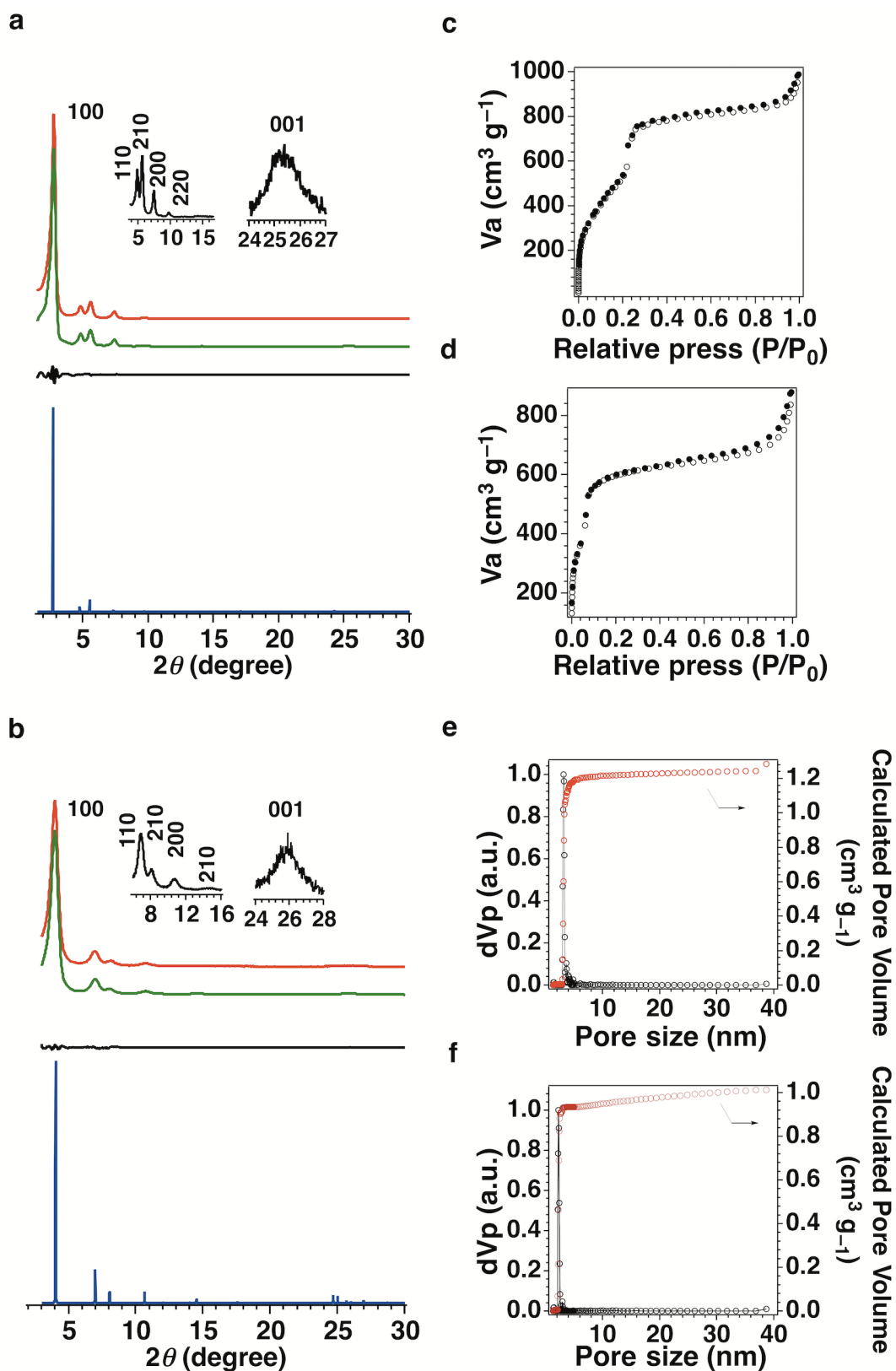


Figure 4.2 PXRD profiles of (a) the TPB-DMTP COF and (b) the TTA-TTB COF. Nitrogen-sorption isotherm curves of (c) the TPB-DMTP COF and the (d) TTA-TTB

COF measured at 77 K. Profiles of the pore size and pore-size distribution of (e) the TPB-DMTP COF and (f) the TTA-TTB COF.

The porosity of the TPB-DMTP COF and the TTA-TTB COF was investigated by nitrogen sorption isotherm measurements at 77 K. Both COFs exhibited typical IV nitrogen sorption isotherms, which justified their mesoporous characters (Figures 4.2c and d). According to the isotherms, the TPB-DMTP COF displayed the Brunauer-Emmett-Teller (BET) surface area of $2105 \text{ m}^2 \text{ g}^{-1}$, while the TTA-TTB COF has a BET surface area of $1733 \text{ m}^2 \text{ g}^{-1}$. By using the nonlocal density function theory method (NDFT), their pore size distribution was evaluated. As shown in Figures 4.2e and f, both COFs exhibited single peak in the pore distribution profiles, demonstrating the TPB-DMTP COF and the TTA-TTB COF possessing mesopores of 3.26 and 2.23 nm, respectively. The pore size is exactly same as that in the previous reports.^{48, 58} Their pore volumes were evaluated as 1.28 and $1.00 \text{ cm}^3 \text{ g}^{-1}$ for the TPB-DMTP COF and the TTA-TTB COF, respectively. Notably, these BET surface areas and pore volumes rank them among the highest porosities of 2D COFs synthesized by $[C_3 + C_2]$ and $[C_3 + C_3]$ topology diagrams. According to the pore volumes together with the density of iodine (4.93 g cm^{-3}), the theoretical capacities of the TPB-DMTP COF and TTA-TTB COF upon full occupation of the pores by iodine are 6.31 and 4.93 g g^{-1} , respectively.

The stability of COFs in the presence of iodine is a must for an adsorption medium. I investigated the oxidation potential of COFs by cyclic voltammetry (CV). The onset oxidation potentials of the TPB-DMTP COF and the TTA-TTB COF were 1.98 and 1.87 V vs RHE , respectively (Figure 4.3 and Table 4.2). These oxidation potentials are much higher than that of iodine (0.54 V vs RHE), so the two COFs are stable in the appearance of iodine.

Table 4.2 Onset oxidation potential of the TPB-DMTP COF and the TTA-TTB COF and iodine.

	Oxidation potential vs Ag/Ag^{+1} (V)	Oxidation potential vs RHE (V)
TPB-DMTP COF	0.78	1.99
TTA-TTB COF	0.66	1.87
Iodine	–	0.54

$$E_{\text{RHE}} = E_{\text{vs Ag/Ag}^+} + E_{\phi\text{Ag/Ag}^+} + 0.059\text{pH}$$

E_{RHE} ; standard potential based on RHE,

$E_{\text{vs Ag/Ag}^+}$; potential based on Ag/Ag^+ ,

$E_{\phi\text{Ag/Ag}^+}$; standard potential of Ag/Ag^+ based on RHE,

pH; pH of the electrolyte.

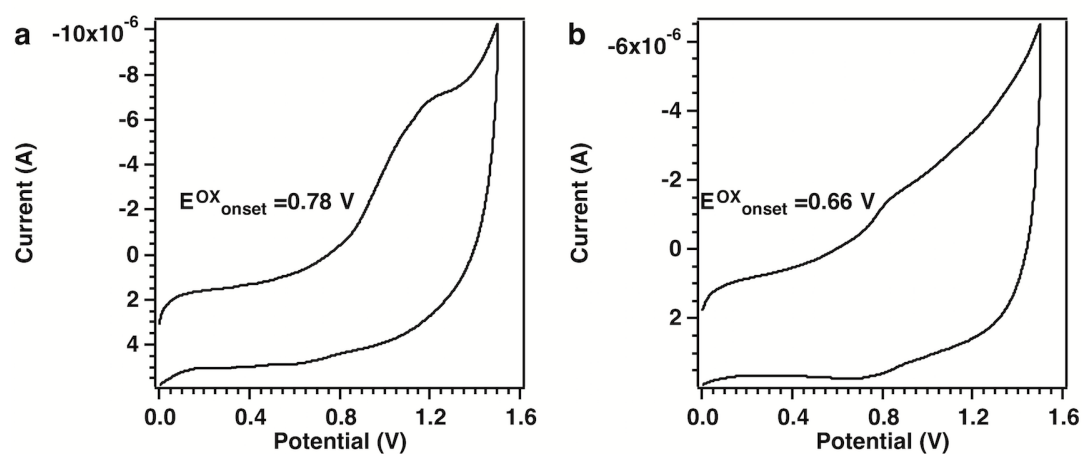


Figure 4.3 The CV curves of (a) the TPB-DMTP COF and (b) the TTA-TTB COF measured in acetonitrile at 298 K.

4.2.2 Iodine Vapor Capture

Vapor iodine uptake was conducted by exposing the COF solid samples to the iodine vapor at 350 K. The gravimetric changes of the COF samples were monitored

by plotting their gained weights versus the exposure time, which were widely used in the literatures.¹³⁻¹⁹ The TPB-DMTP COF exhibited a rapid adsorption to yield an almost linear increment before 48 h and then saturated within 92 h (Figure 4.4a, red marks). Similarly, the TTA-TTB COF exhibited a quick uptake of iodine and completed the adsorption in 96 h (Figure 4.4a, black marks). Remarkably, the equilibrium uptake reaches 6.26 and 4.51 g g⁻¹ for the TPB-DMTP COF and the TTA-TTB COF, respectively. Interestingly, these uptake capacities are very close to the theoretical values, which are 6.31 and 4.93 g g⁻¹, respectively, calculated by multiplying the pore volume and the density of iodine. From the above results, it is clear that the mesoporous 1D channels of COFs are fully accessible to iodine, so that the porous space is fully filled by iodine.

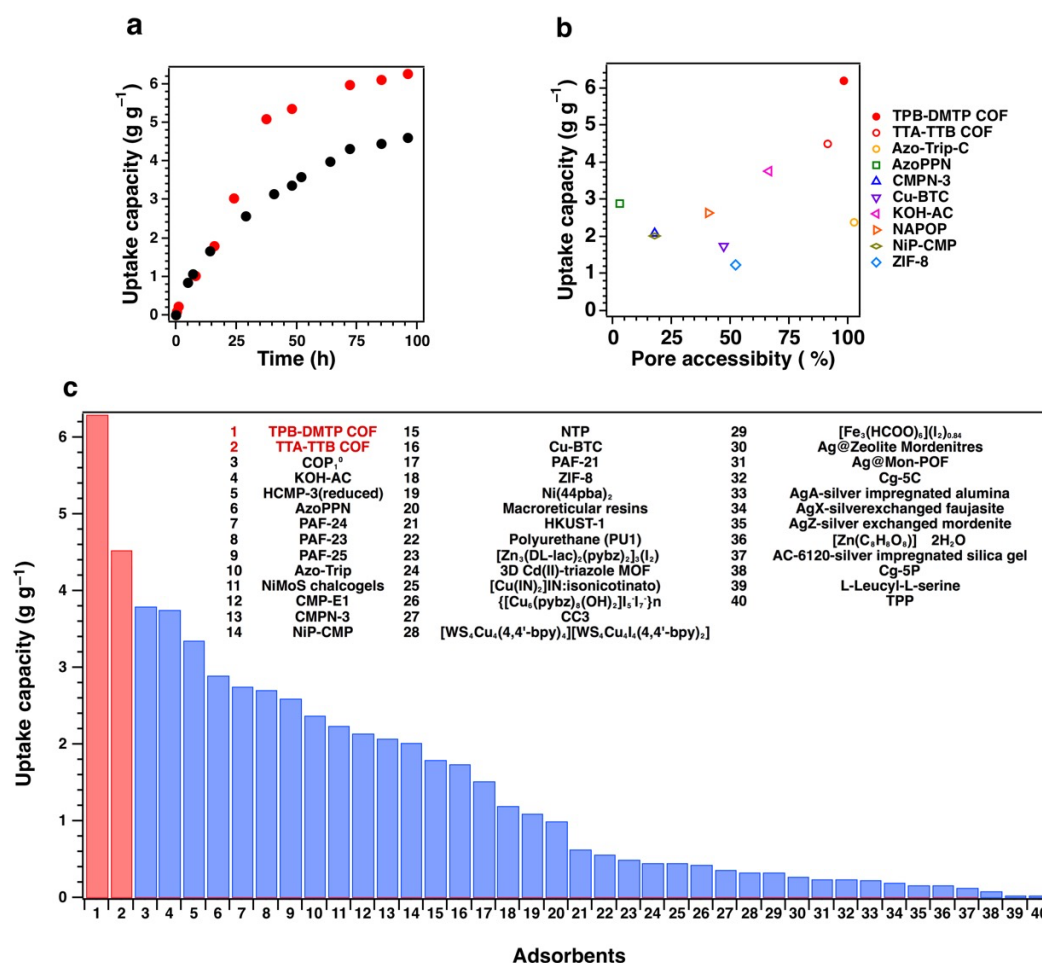


Figure 4.4 (a) Uptake of iodine as a function of time at 75 °C of the TPB-DMTP COF

(red filled circles) and the TTA-TTB COF (black filled circles). (b) Survey of capture performance in representative porous materials working at 350 K. (c) Comparisons of iodine uptake capacities of different adsorbent materials. The red columns represent the mesoporous COFs in this work and the blue columns represent the other porous materials.

The adsorption capacities of mesoporous COFs were further confirmed by the thermal gravimetric analysis (TGA) of the iodine-loaded COFs. The pristine TPB-DMTP COF and TTA-TTB COF exhibited high thermal stability up to 400 and 500 °C, respectively, under nitrogen (Figure 4.5). Upon heating under nitrogen, the iodine-loaded TPB-DMTP COF (Figure 4.5a) started to loss weight at 90 °C, and completed the weigh loss at 250 °C. This is the same case for the iodine-loaded TTA-TTB COF (Figure 4.5b), which also exhibited the loss of iodine at 90 °C and finished at 250 °C. Because these temperature ranges are much lower than those for the decomposition of COFs themselves, the weight loss of the samples can be attributed to the flow out of iodine. The weight loss of the iodine in the TGA samples is close to the amount of the loaded iodine.

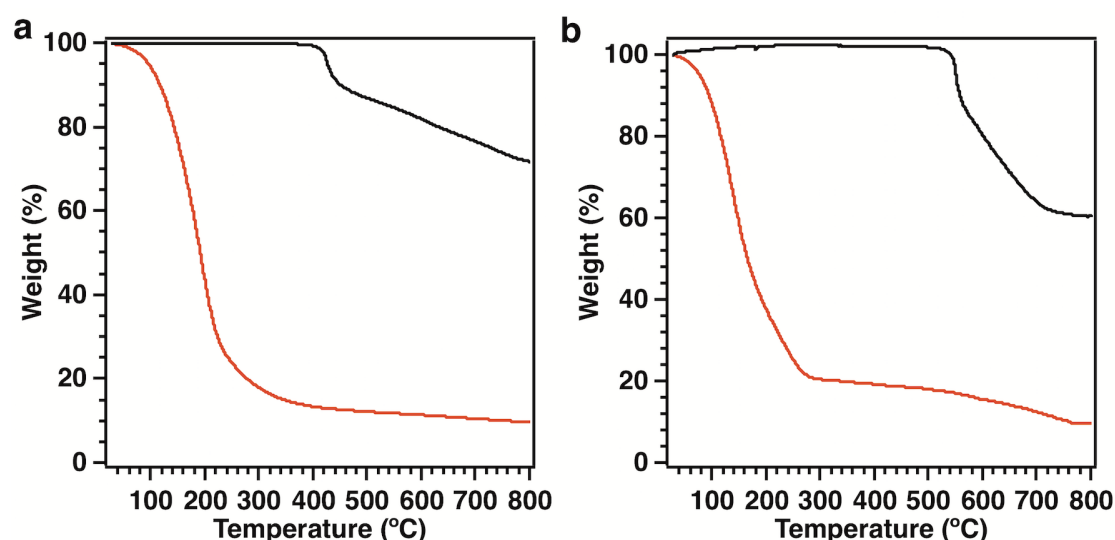


Figure 4.5 (a) TGA curves of the pristine TPB-DMTP COF (black curve) and the iodine-loaded TPB-DMTP COF (red curve). (b) TGA curves of the pristine TTA-TTB COF (black curve) and the iodine-loaded TTA-TTB COF (red curve).

It is interesting to compare the pore accessibility and equilibrium iodine uptake of the mesoporous COFs with the reported top-performing porous adsorbents. Figure 4.4b shows that both mesoporous COFs exhibit the largest pore accessibility and iodine capture capacity among all the reported porous iodine adsorbents worked at 350 K and ambient pressure in my literature survey. As summarized in Figure 4.4c and Table 4.3, the capacity of the TPB-DMTP COF is 1.7-27 fold as high as those of the iodine adsorbents reported to date, including porous Ag-MOR (0.275 g g^{-1}),² CC3 (0.364 g g^{-1}),⁵⁹ ZIF-8 (1.2 g g^{-1}),⁶⁰ NiP-CMP (2.02 g g^{-1}),¹⁹ PAF24 (2.76 g g^{-1}),¹⁵ AzoPPN (2.9 g g^{-1}),¹⁴ and KOH-AC (3.76 g g^{-1}).⁶¹ Although microporous COFs have been developed for iodine adsorption, the highest uptake capacity is reported for SIOC-COF-7, which has a pore volume of $0.41 \text{ cm}^3 \text{ g}^{-1}$ and shows a capacity of 4.81 g g^{-1} .⁶² This high capacity originates from the contribution of 1–2 μm sized extrinsic hollows formed by self-assembly of COFs other than the inherent microporosity. In contrast, the TPB-DMTP COF is based on its intrinsic mesoporous channels for the adsorption of iodine. Nevertheless, the capacity of the TPB-DMTP COF is still 1.3 fold as high as that of SIOC-COF-7.

4.2.3 Cycle Performance

The easy removal of iodine from the pores of the COFs enables the cycle use of the COF materials. In addition to the thermal approach, I observed that these COFs could also be regenerated by immersing the iodine-loaded samples in MeOH at room temperature. I dried the regenerated COFs samples under vacuum and subjected these samples for the next round iodine vapor capture. Notably, the TPB-DMTP COF exhibited excellent cycle performance and enabled at least five cycles by retaining 97% of the original capacity (Figure 4.6a). Under the otherwise same conditions, the TTA-TTB COF after five cycles retained 95% of its initial capacity (Figure 4.6b). The above cycle performances are exceptional and suggest that these mesoporous COFs are robust against oxidative iodine after even long-term high-temperature exposure. Surprisingly, the pore structure of the recycled COFs are still highly accessible with accessibility of 97% for TPB-DMTP COF and 95% for TTA-TTB COF, indicating

that the pores are fully accessible to iodine even after five cycles. Moreover, the porosity of the TPB-DMTP COF and TTA-TTB COF retained well after cycle use. (Figures 4.7 and 4.8) Indeed, the PXRD patterns of the regenerated COF samples revealed that the COF samples still possess the crystallinity, suggesting their robust nature of the crystalline networks (Figure 4.9).

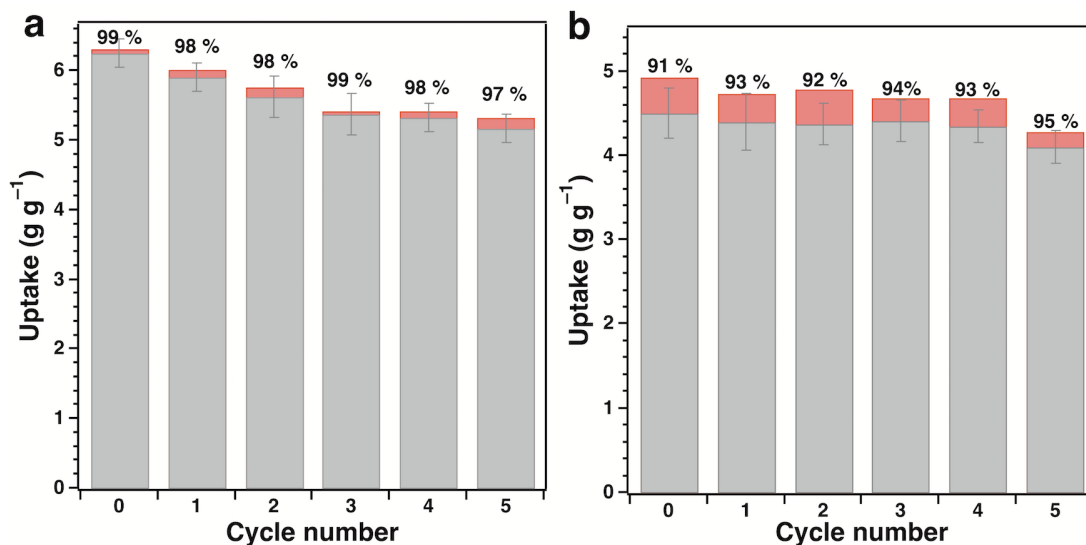


Figure 4.6 Cycle performance of the (a) TPB-DMTP COF and the (b) TTA-TTB COF in vapor adsorption of iodine. (Red for the theoretical uptake capacity and grey for the experimental uptake). The ration of experimental to the theoretical capacity was marked on the to of each bar.

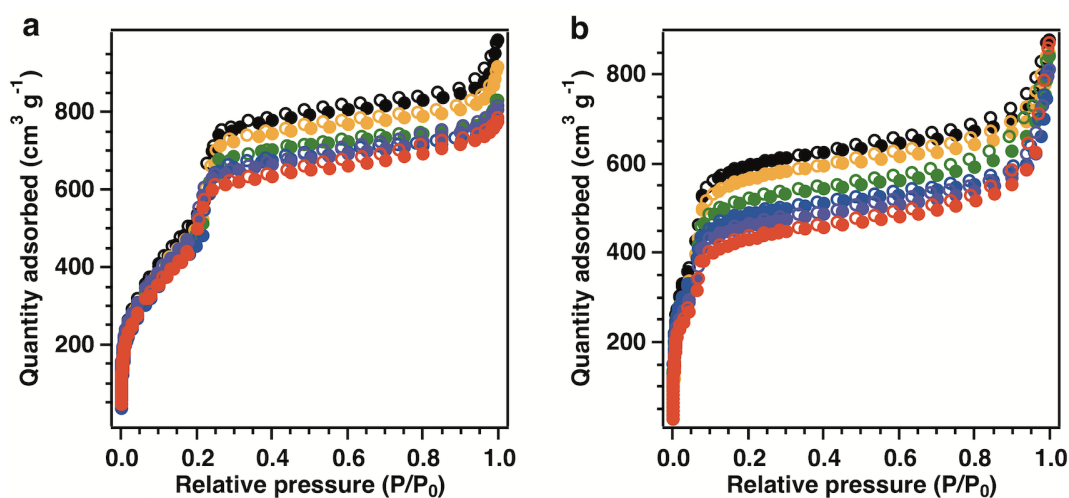


Figure 4.7 Nitrogen sorption isotherms of the (a) TPB-DMTP COF and (b) TTA-TTB

COF measured at 77 K after cycles of iodine capture. Black for the original sample, yellow for the 1st cycle, green for the 2nd cycle, blue for the 3rd cycle, purple for the 4th cycle and red for the 5th cycle.

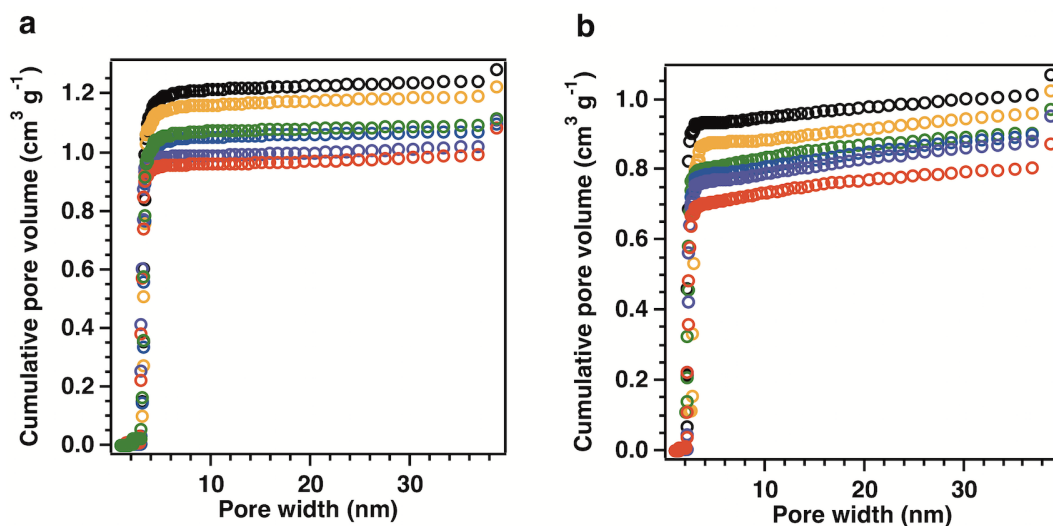


Figure 4.8 Pore volume profiles of the (a) TPB-DMTP COF and (b) TTA-TTB COF sample measured at 77 K after cycles of iodine capture. Black for the original sample, yellow for the 1st cycle, green for the 2nd cycle, blue for the 3rd cycle, purple for the 4th cycle and red for the 5th cycle.

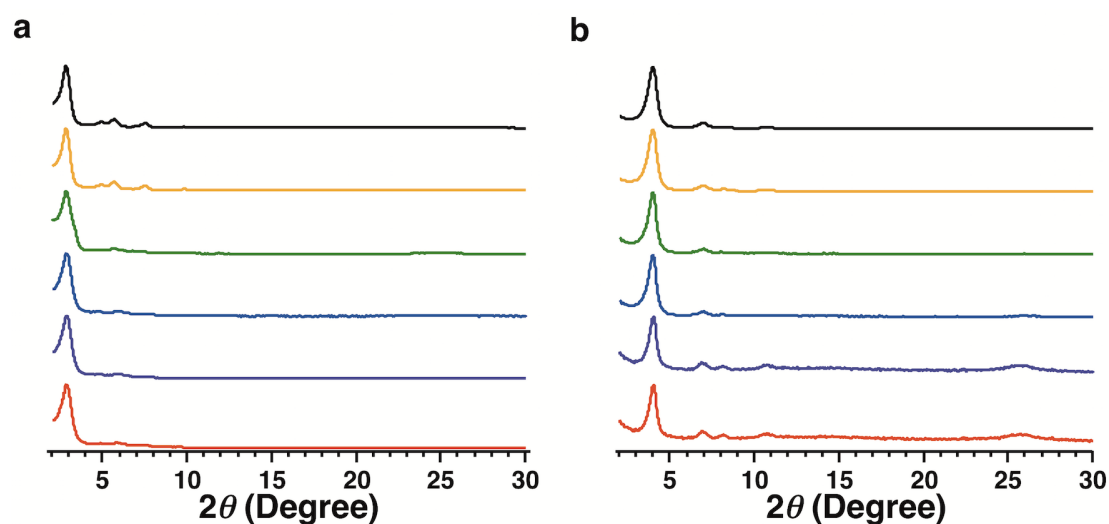


Figure 4.9 PXRD profiles of the (a) TPB-DMTP COF and (b) TTA-TTB COF. Black for the original sample, yellow for the 1st cycle, green for the 2nd cycle, blue for the 3rd cycle, purple for the 4th cycle and red for the 5th cycle.

To ensure the chemical integrity of these COFs after cycle use, I further investigated their infrared spectral changes. As shown in Figure 4.10, the C=N stretching bonds at 1620 cm^{-1} for the TPB-DMTP COF and the TTA-TTB COF were retained even after five cycles, indicating the robustness of the imine linkages. Moreover, the C=C bonds at around 1600 cm^{-1} assigned to the phenyl groups of these COFs keep intact upon cycles of iodine capture.

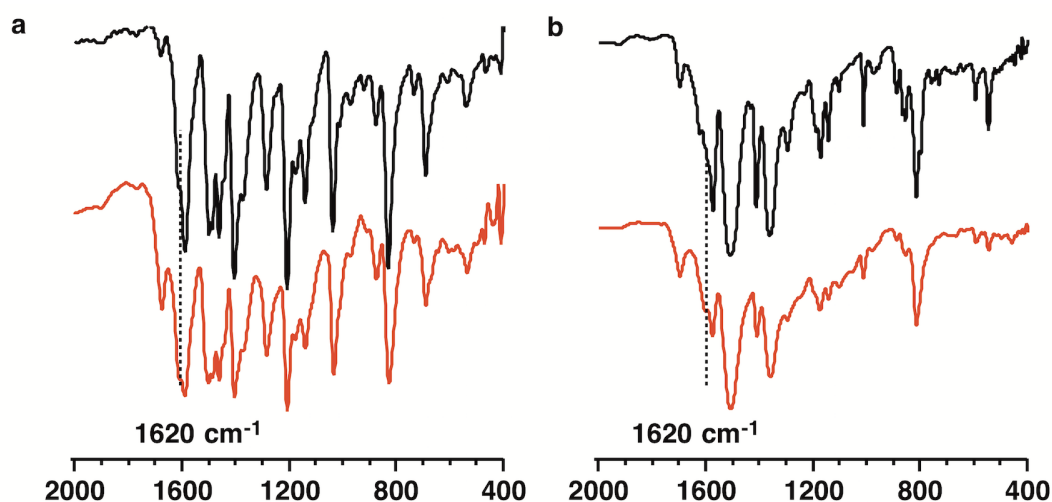


Figure 4.10 Infrared spectra of (a) the TPB-DMTP COF and (b) the TTA-TTB COF upon cycle use in vapor adsorption of iodine (black for pristine COFs, red for COFs after five cycles).

4.2.4 Iodine Capture from Iodine-Hexane Solution

The kinetics of the iodine uptake with the COFs was investigated by dispersing the COF solid samples (30 mg) into a hexane solution of iodine (2 mg mL^{-1}) at $25\text{ }^{\circ}\text{C}$. It is easy to monitor the uptake process by measuring the time-dependent UV-vis spectral change of the hexane solution, because iodine exhibits a strong absorbance at 523 nm. Surprisingly, the iodine uptake by the TPB-DMTP COF was very quick and in only 2 h it completed 92% of the saturated adsorption (Figure 4.11a). The adsorption was saturated within 8 h. Similarly, the TTA-TTB COF exhibited a sharp adsorption within the first 1 h and then saturated with 10 h (Figure 4.11b).

Notably, these two adsorption profiles can be fitted with the pseudo second order

model. In the case of the TPB-DMTP COF, the pseudo second order model yielded a linear plot with a coefficient of determination $R^2 = 0.9997$ (Figure 4.11c). The adsorption rate constant was evaluated to be $0.11 (\%h)^{-1}$. The TTA-TTB-COF also yielded a linear plot with $R^2 = 0.9998$. The adsorption rate constant of the TTA-TTB COF was estimated as $0.03 (\%h)^{-1}$ (Figure 4.11d). Under same conditions, the rate constant of the best-performed microporous material was $0.0126 (\%h)^{-1}$.¹⁴ Therefore, the mesoporous TPB-DMTP COF and TTA-TTB COF can uptake iodine from solution at a speed that is 8.7 and 2.5 fold as high as that of the microporous material.

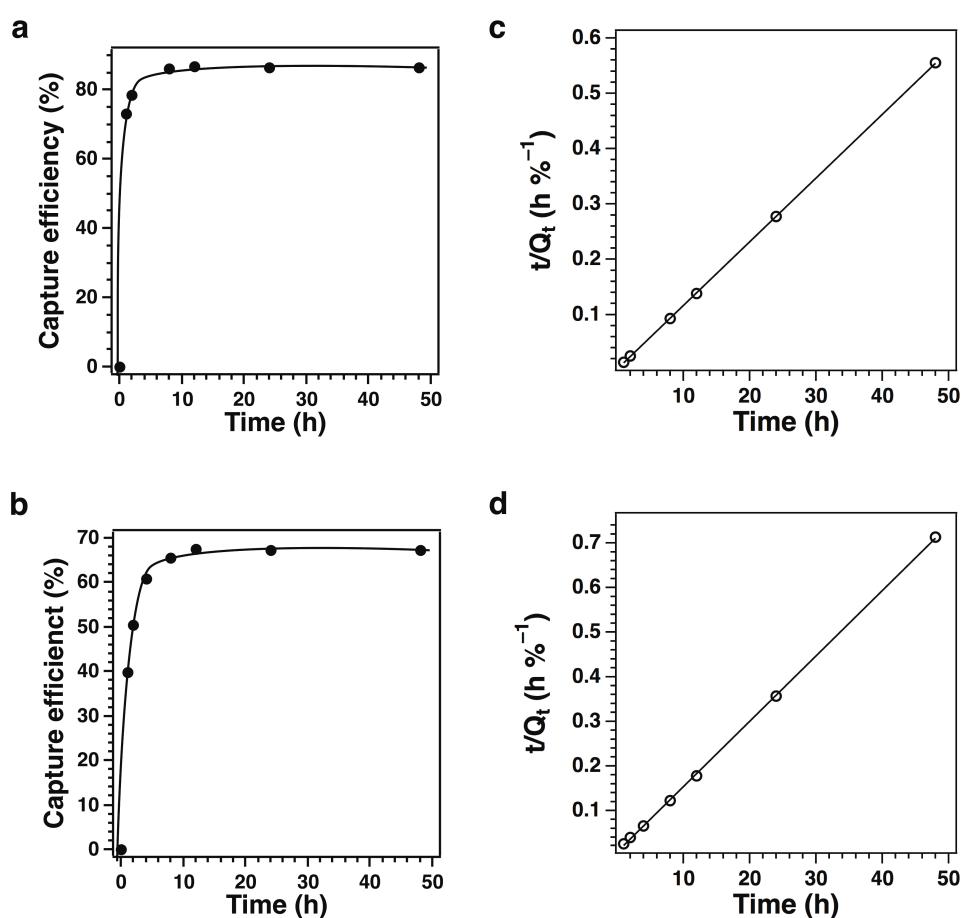


Figure 4.11 Adsorption kinetics of the (a) TPB-DMTP COF and (b) the TTA-TTB COF in the adsorption of iodine in a hexane solution (2 mg mL^{-1}). Pseudo-second order of adsorption rate constant of (c) the TPB-DMTP COF and (d) the TTA-TTB COF in the adsorption of iodine in a hexane solution (2 mg mL^{-1}).

Table 4.3 Summary of iodine sorption capacity of reported adsorbents

Porous Materials	Temp. (°C)	I ₂ uptake (g g ⁻¹)	Ref.
TPB-DMTP COF	75	6.26	This work
TTA-TTB COF	75	4.31	
SIOC-COF-7	75	4.81	62
COP ₁ ⁰	60	3.8	10
KOH-AC	77	3.76	61
HCMP-3(reduced)	85	3.36	13
AzoPPN	77	2.90	14
PAF-24	75	2.76	15
PAF-23	75	2.71	15
PAF-25	75	2.60	15
Azo-Trip	77	2.38	63
NiMoS chalcogels	60	2.25	6
CMP-E1	75	2.15	15
CMPN-3	75	2.08	18
NiP-CMP	75	2.02	19
NTP	75	1.80	17
Cu-BTC	75	1.75	64
PAF-21	75	1.52	15
ZIF-8	75	1.20	65
Ni(44pba) ₂	RT	1.1	66
HKUST-1	75	0.636	64
Polyurethane (PU1)	70	0.565	67
[Zn ₃ (DL-lac) ₂ (pybz) ₂] ₃ (I ₂)	25	0.497	68
3D Cd(II)-triazole MOF	25	0.460	69
[Cu(IN) ₂]IN:isonicotinato)	140	0.452	70
{[Cu ₆ (pybz) ₈ (OH) ₂]I ₅ ⁻ I ₇ ⁻ } _n	140	0.432	71
CC3	20	0.364	59
[WS ₄ Cu ₄ (4,4'-bpy) ₄][WS ₄ Cu ₄ I ₄ (4,4'-bpy) ₂]	25	0.329	72
[Fe ₃ (HCOO) ₆](I ₂) _{0.84}	25	0.328	73
Ag@Zeolite Mordenites	95	0.275	2
Ag@Mon-POF	70	0.250	74
Cg-5C	25	0.239	7
Macroporous resins	<50	0.200-1.000	3
AgX-silverexchanged faujasite	150	0.080-0.200	3
AgZ-silver exchanged mordenite	150	0.170	3
[Zn(C ₈ H ₈ O ₈)]•2H ₂ O	19	0.166	75
AC-6120-silver impregnated silica gel	130	0.135	3
AgA-silver impregnated alumina	150	0.100-0.235	3
Cg-5P	25	0.087	7
L-Leucyl-L-serine	25	0.038	76

4.3 Conclusion

I explored the high capability of mesoporous materials as a porous medium to remove iodine and demonstrated the unique features of COFs in the adsorption of iodine. The mesoporous COFs enable the full access of the porous space to iodine and achieve exceptional capacity. Moreover, the chemically and thermally stable skeletons endow the COFs with remarkable cycle performance. These results unambiguously revealed that mesoporous COFs offer a suitable platform for coping with volatile fission waste issues.

4.4 Experimental Sections

4.4.1 Methods

JEOL models JNM-LA400 NMR spectrometers were used to measure the ^1H nuclear magnetic resonance (NMR) spectra. Using the solvent residual proton peaks as reference, the chemical shifts (δ in ppm) of compounds are confirmed. A JASCO model FT-IR-6100 infrared spectrometer was used to determine the Fourier transform infrared (FT-IR) spectra. The Rigaku model RINT Ultima III diffractometer was used to confirm the crystallinity character by the Powder X-ray diffraction (PXRD) data. In detail, the sample powder was deposited on glass substrate and the measure starts from $2\theta = 2.5^\circ$ up to 30° with 0.02° increment. At 77 K created by liquid nitrogen, a Micromeritics Instrument Corporation model 3Flex surface characterization analyzer was used to measure the nitrogen sorption isotherms. The specific surface areas and the pore distribution was confirmed by the Brunauer-Emmett-Teller (BET) method and the non-local density functional theory (NLDFT) model, respectively. For the isotherm measurements, all the samples were degassed in vacuum at 120°C for more than 10 h. A Mettler-Toledo model TGA/SDTA851e was used to measure the TGA curves in nitrogen atmosphere at a rate of $10^\circ\text{C min}^{-1}$. The JEOL model JSM-6700 was used for field-emission scanning electron microscopy (FE-SEM). The operation is conducted at an accelerating voltage of 5.0 kV. Before measurement, the sample was coated by gold after drop-casting its acetone suspension on mica substrate.

Cyclic voltammetry (CV) was performed using a standard one compartment, three-electrode electrochemical cell attached to an ALS/CHI 610C Electrochemical Workstation. The Ag/Ag⁺ nonaqueous electrode was used as reference electrode. Glass-carbon was used as the working electrode, and Pt was used as the counter electrode. Tetrabutylammonium hexafluorophosphate (0.1 M) in acetonitrile was used as electrolyte solution. The potential range was set between 0 V and 1.5 V and the scan rate was 100 mV s⁻¹.

The efficiency of the TPB-DMTP COF and TTA-TTB COF as iodine adsorbent for removing iodine from hexane solutions has been examined by investigating the iodine adsorption kinetics of COFs (30.0 mg) in an iodine-hexane solution (2 mg g⁻¹; 3 mL). The experimental data were fitted with the pseudo-second-order kinetic model using the following equation: $t/Q_t = 1/(kQ_e^2) + t/Q_e$, whereas k ((%h)⁻¹) is the rate constant of pseudo-second-order adsorption, Q_t (%) is the capture efficiency of iodine adsorbed at time t (h), and Q_e (%) is the capture efficiency of iodine adsorbed at equilibrium.

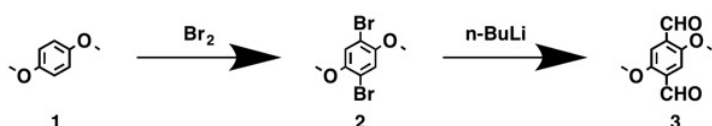
General Procedure for Iodine Vapor Sorption Kinetics. An open small vial (2 mL) containing the TPB-DMTP COF or TTA-TTB COF (50.0 mg) sample was deposited into a large vial (10 mL) containing iodine (2 g). The large vial was sealed to avoid iodine escape and kept in an oven at 75 °C. After a certain period, the large vial was taken out from the oven and cooled down at room temperature. The small vial containing the COF sample was sealed and put back to the iodine-containing large vial. The large vial was sealed and put back in the oven at 75 °C to continue the adsorption till the mass of small vial containing the COF sample did not change.

General Procedure for Recycling. Iodine-loaded TPB-DMTP COF or TTA-TTB COF sample was added to MeOH (20 mL) and kept at room temperature. Replacing MeOH every 2 h till there was no more color change. The COF sample was collected by filtration on a filter paper, washed with MeOH, dried under vacuum at 120 °C overnight and reused for the next cycle.

General Procedure for Iodine Sorption Kinetics in Solution. The TPB-DMTP

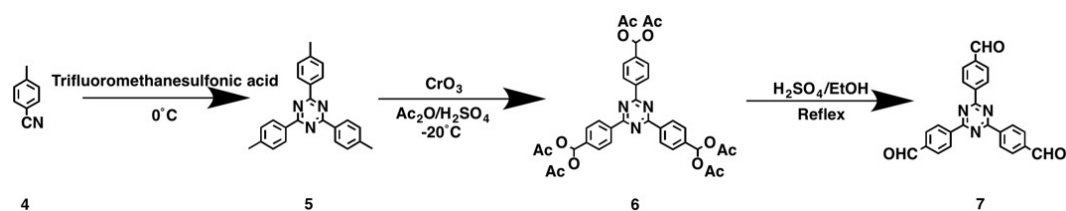
COF or TTA-TTB COF (30.0 mg) was added to a vial containing iodine-hexane solution (2 mg mL^{-1} , 3 mL) and kept at room temperature in dark for a certain period. To avoid the escape of iodine, the vial was sealed. The iodine sample (50 μL) was diluted with hexane (1.45 mL). The diluted solution was subjected to UV-vis spectroscopy for the determination of iodine concentration of the hexane solution, based on the iodine extinction coefficient ($\epsilon = 3.5481 \text{ g mg}^{-1} \text{ cm}^{-1}$ at $\lambda_{\text{max}} = 523 \text{ nm}$).

4.4.2 Synthetic Procedures



1,4-Dibromo-2,5-dimethoxybenzene (2).⁷⁷ Bromine (16.8 mL) was slowly added into a solution containing 1,4-dimethoxybenzene (1, 20 g, 0.149 mol) and acetic acid (40 mL) at 0°C . After stirred at 0°C overnight, the mixture was poured into a diluted Na_2SO_3 solution (0.1 M, 100 mL). The solid product was collected by filtration, washed with water and recrystallized from methanol. The obtained white crystal was dried under vacuum. Yield: 88%. $^1\text{H NMR}$ (CDCl_3 , 400 MHz): δ (ppm) = 7.092 (s, 2H, ArH), 3.837 (s, 6H, OCH_3).

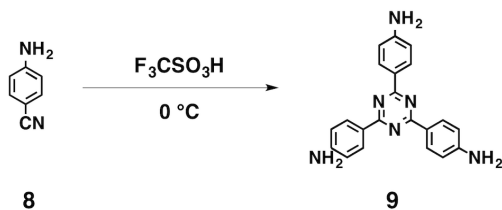
2,5-Dimethoxyterephthalaldehyde (3, DMTA).⁷⁸ To a degassed solution of 1,4-dibromo-2,5-dimethoxybenzene (2, 10 g, 30 mmol) in anhydrous THF (200 mL) was added with n-butyllithium-hexane solution (1.6 M, 125 mL) under Ar at -78°C . The resulting solution was stirred for 2 h at -78°C . DMF (30 mL) was added to the mixture and the resulting system was kept under stirring overnight. The mixture was added with an aqueous HCl solution (1 N, 100 mL) and stirred for 30 min to yield yellow crystals. The crystals were collected by filtration and washed by water and cold methanol. The organic layer was washed with water (50 mL), dried over anhydrous MgSO_4 , and concentrated under vacuum to yield yellow crystals. Yield: 56%. $^1\text{H NMR}$ (400 Hz, CDCl_3) δ (ppm) = 10.491 (s, 2H, CHO), 7.447 (s, 2H, ArH), 3.934 (s, 6H, OCH_3).



1,3,5-Tris-(4-methyl-phenyl)triazine (5).⁷⁹ Trifluoromethanesulfonic acid (5.0 mL, 53.8 mmol) was cooled at $-20\text{ }^{\circ}\text{C}$ by NaCl/ice bath under stirring. *p*-Tolunitrile (3.1 mL, 25.0 mmol) was added dropwise over 1 h. The mixture turned into a slurry solid and was kept for 24 h. The mixture was poured into ice water under stirring. The resulting mixture was neutralized with aqueous ammonia solution (25%). The off-white precipitate was collected by filtration, washed with acetone ($3 \times 5\text{ mL}$) and dried under vacuum. Yield: 88%. $^1\text{H NMR}$ (400 Hz, CDCl_3) δ (ppm) = 8.691-8.641 (d, 6H, ArH), 7.372-7.353 (d, 6H, ArH), 2.474 (s, 9H, CH_3).

[4,4',4''-(1,3,5-Triazine-2,4,6-triyl)tris(4,1-phenylene)]-tris(methanetriyl)hexa acetate (6).⁷⁹ 4 (2 g, 5.7 mmol) was dissolved in acetic anhydride (20 mL). The solution was cooled down at $-20\text{ }^{\circ}\text{C}$ by NaCl/ice bath under stirring. After sulfuric acid (4 mL, 98%) was added, chromium(VI) oxide (5 g, 50 mmol) in acetic anhydride (25 mL) was dropwise added to the mixture over a period of 3.5 h under stirring, while the temperature was kept below $0\text{ }^{\circ}\text{C}$. The greenish solution was stirred for another one hour and then added dropwise to water (125 mL) at $0\text{ }^{\circ}\text{C}$. The yellowish precipitate was collected by filtration, washed with water until neutral, dried under vacuum and purified by column chromatography (50:1 DCM/EtOAc) on silica gel. Yield: 38%. $^1\text{H NMR}$ (400 Hz, CDCl_3) δ (ppm) = 8.789-8.769 (d, 6H, ArH), 7.784 (s, 3H, $\text{CH}(\text{OAc})_2$) 7.733-7.712 (d, 6H, ArH), 2.169 (s, 6H, OAc).

4,4',4''-(1,3,5-Triazine-2,4,6-triyl)tribenzaldehyde (7, TTB).⁷⁹ 6 (460 mg) was dispersed in a mixture of H_2O and EtOH (5 mL/5 mL) and added with sulfuric acid (0.5 mL, 98%). The system was refluxing overnight. After cooling to room temperature, the white precipitate was collected by filtration, washed with water and dried under vacuum. Yield: 89%. $^1\text{H NMR}$ (400 Hz, CDCl_3) δ (ppm) = 10.171 (s, 3H, CHO), 8.963-8.942 (d, 6H, ArH), 8.131-8.105 (d, 6H, ArH).



4,4',4''-(1,3,5-Triazine-2,4,6-triyl)trianiline (9, TTA).⁸⁰ 4-Aminobenzonitrile (8) (1.65 g, 13.97 mmol) was cooled down to 0 °C by ice bath and was added with trifluoromethanesulfonic acid dropwise (4.3 mL, 48.6 mmol) over 60 min at 0 °C. The resulting mixture was stirred for 24 h at room temperature in nitrogen. Water (20 mL) was added and the mixture was neutralized using ammonia solution (25%). The pale yellow precipitate was collected by filtration, washed with water and dried under vacuum. Yield: 88%. ¹H NMR (400 Hz, DMSO-d₆) δ (ppm) = 8.323-8.302 (d, 6H, ArH), 6.657 -6.636 (d, 6H, ArH), 5.874 (s, 6H, NH₂).

TPB-DMTP COF. An *o*-DCB/*n*-BuOH/6 M AcOH (5/5/1 by vol.; 1.1 mL) mixture of 1,3,5-tris(4-aminophenyl)benzene (28.1 mg, 0.08 mmol) and DMTA (23.3 mg, 0.12 mmol) was added into a Pyrex tube (10 mL) and the tube was degassed by three freeze-pump-thaw cycles. The tube was sealed and stored at still at 120 °C for 3 days. The precipitate was collected by centrifugation, and washed with anhydrous THF five times and acetone twice. The powder was dried at 120 °C under vacuum overnight to yield the TPB-DMTP COF in an isolated yield of 81%.

TTA-TTB COF. A mesitylene/dioxane/6 M AcOH (5/5/1 by vol.; 1.1 mL) mixture of TTA (15.0 mg, 0.042 mmol) and TTB (16.6 mg, 0.042 mmol) was added into a Pyrex tube (10 mL) and the tube degassed by three freeze-pump-thaw cycles. The tube was sealed and stored as still at 120 °C for 3 days. The precipitate was collected by centrifugation, and washed with anhydrous THF five times and acetone twice. The powder was dried at 120 °C under vacuum overnight to yield the TTA-TTB COF in an isolated yield of 78%.

4.5 References

1. Mushkacheva G., *et al.* Thyroid abnormalities associated with protracted childhood exposure to ¹³¹I from atmospheric emissions from the mayak weapons

- facility in Russia. *Radiat. Res.* **166**, 715-722 (2006).
2. Chapman K. W., Chupas P. J., Nenoff T. M. Radioactive iodine capture in silver-containing mordenites through nanoscale silver iodide formation. *J. Am. Chem. Soc.* **132**, 8897-8899 (2010).
 3. Haefner D. *Methods of Gas Phase Capture of Iodine from Fuel Reprocessing Off-Gas: A Literature Survey* (Idaho National Laboratory, 2007).
 4. Clement B., *et al.* *State of The Art Report on Iodine Chemistry* (Nuclear Energy Agency of the OECD, 2007).
 5. *Treatment, Conditioning and Disposal of Iodine-129* (International Atomic Energy Agency, 1987).
 6. Subrahmanyam K. S., *et al.* Chalcogenide aerogels as sorbents for radioactive iodine. *Chem. Mater.* **27**, 2619-2626 (2015).
 7. Riley B. J., *et al.* Chalcogen-based aerogels as a multifunctional platform for remediation of radioactive iodine. *RSC Adv.* **1**, 1704-1715 (2011).
 8. Subrahmanyam K. S., Malliakas C. D., Sarma D., Armatas G. S., Wu J., Kanatzidis M. G. Ion-exchangeable molybdenum sulfide porous chalcogel: Gas adsorption and capture of iodine and mercury. *J. Am. Chem. Soc.* **137**, 13943-13948 (2015).
 9. Riley B. J., *et al.* Polyacrylonitrile-chalcogel hybrid sorbents for radioiodine capture. *Environ. Sci. & Technol.* **48**, 5832-5839 (2014).
 10. Das G., *et al.* Multifunctional redox-tuned viologen-based covalent organic polymers. *J. Mater. Chem. A* **4**, 15361-15369 (2016).
 11. Xu Y., Jin S., Xu H., Nagai A., Jiang D. Conjugated microporous polymers: Design, synthesis and application. *Chem. Soc. Rev.* **42**, 8012-8031 (2013).
 12. Ben T., *et al.* Targeted synthesis of a porous aromatic framework with high stability and exceptionally high surface area. *Angew. Chem. Int. Ed.* **48**, 9457-9460 (2009).
 13. Liao Y., Weber J., Mills B. M., Ren Z., Faul C. F. J. Highly efficient and reversible iodine capture in hexaphenylbenzene-based conjugated microporous

- polymers. *Macromolecules* **49**, 6322-6333 (2016).
14. Li H., Ding X., Han B. Porous azo-bridged porphyrin–phthalocyanine network with high iodine capture capability. *Chem. Eur. J.* **22**, 11863-11868 (2016).
 15. Yan Z., Yuan Y., Tian Y., Zhang D., Zhu G. Highly efficient enrichment of volatile iodine by charged porous aromatic frameworks with three sorption sites. *Angew. Chem. Int. Ed.* **54**, 12733-12737 (2015).
 16. Pei C., Ben T., Xu S., Qiu S. Ultrahigh iodine adsorption in porous organic frameworks. *J. Mater. Chem. A* **2**, 7179-7187 (2014).
 17. Ma H., *et al.* Nitrogen-rich triptycene-based porous polymer for gas storage and iodine enrichment. *ACS Macro Lett.* **5**, 1039-1043 (2016).
 18. Chen Y., *et al.* Synthesis of conjugated microporous polymer nanotubes with large surface areas as absorbents for iodine and CO₂ uptake. *J. Mater. Chem. A* **3**, 87-91 (2015).
 19. A S., *et al.* Highly efficient and reversible iodine capture using a metalloporphyrin-based conjugated microporous polymer. *Chem. Comm.* **50**, 8495-8498 (2014).
 20. Krishna R. Describing the diffusion of guest molecules inside porous structures. *J. Phys. Chem. C* **113**, 19756-19781 (2009).
 21. Bhatia S. K., Nicholson D. Some pitfalls in the use of the knudsen equation in modelling diffusion in nanoporous materials. *Chem. Eng. Sci.* **66**, 284-293 (2011).
 22. Beerdsen E., Dubbeldam D., Smit B. Understanding diffusion in nanoporous materials. *Phys. Rev. Lett.* **96**, 044501 (2006).
 23. Chmelik C., *et al.* Inflection in the loading dependence of the maxwell–stefan diffusivity of iso-butane in mfi zeolite. *Chem. Phy. Lett.* **459**, 141-145 (2008).
 24. Krishna R. Diffusion in porous crystalline materials. *Chem. Soc. Rev.* **41**, 3099-3118 (2012).
 25. Hertzsch T., Budde F., Weber E., Hulliger J. Supramolecular-wire confinement of I₂ molecules in channels of the organic zeolite

- tris(*o*-phenylenedioxy)cyclotriphosphazene. *Angew. Chem. Int. Ed.* **41**, 2281-2284 (2002).
26. Feng X., Ding X., Jiang D. Covalent organic frameworks. *Chem. Soc. Rev.* **41**, 6010-6022 (2012).
 27. Ding S., Wang W. Covalent organic frameworks (COFs): From design to applications. *Chem. Soc. Rev.* **42**, 548-568 (2013).
 28. Dogru M., Bein T. On the road towards electroactive covalent organic frameworks. *Chem. Comm.* **50**, 5531-5546 (2014).
 29. Huang N., Wang P., Jiang D. Covalent organic frameworks: A materials platform for structural and functional designs. *Nat. Rev. Mater.* **1**, 16068 (2016).
 30. Waller P. J., Gándara F., Yaghi O. M. Chemistry of covalent organic frameworks. *Acc. Chem. Res.* **48**, 3053-3063 (2015).
 31. DeBlase C. R., Dichtel W. R. Moving beyond boron: The emergence of new linkage chemistries in covalent organic frameworks. *Macromolecules* **49**, 5297-5305 (2016).
 32. Diercks C. S., Yaghi O. M. The atom, the molecule, and the covalent organic framework. *Science* **355**, (2017).
 33. Côté A. P., Benin A. I., Ockwig N. W., O'Keeffe M., Matzger A. J., Yaghi O. M. Porous, crystalline, covalent organic frameworks. *Science* **310**, 1166-1170 (2005).
 34. Chen L., *et al.* Photoelectric covalent organic frameworks: Converting open lattices into ordered donor-acceptor heterojunctions. *J. Am. Chem. Soc.* **136**, 9806-9809 (2014).
 35. Dogru M., *et al.* A photoconductive thienothiophene-based covalent organic framework showing charge transfer towards included fullerene. *Angew. Chem. Int. Ed.* **52**, 2920-2924 (2013).
 36. Wan S., Guo J., Kim J., Ihee H., Jiang D. A photoconductive covalent organic framework: Self-condensed arene cubes composed of eclipsed 2D polypyrene sheets for photocurrent generation. *Angew. Chem. Int. Ed.* **48**, 5439-5442 (2009).

37. Wan S., Guo J., Kim J., Ihee H., Jiang D. A belt-shaped, blue luminescent, and semiconducting covalent organic framework. *Angew. Chem. Int. Ed.* **47**, 8826-8830 (2008).
38. Ding S. Y., et al. Thioether-based fluorescent covalent organic framework for selective detection and facile removal of mercury (II). *J. Am. Chem. Soc.* **138**, 3031-3037 (2016).
39. Huang N., Zhai L., Xu H., Jiang D. Stable covalent organic frameworks for exceptional mercury removal from aqueous solutions. *J. Am. Chem. Soc.* **139**, 2428-2434 (2017).
40. Sun Q., et al. Postsynthetically modified covalent organic frameworks for efficient and effective mercury removal. *J. Am. Chem. Soc.* **139**, 2786-2793 (2017).
41. Chandra S., Kundu T., Dey K., Addicoat M., Heine T., Banerjee R. Interplaying intrinsic and extrinsic proton conductivities in covalent organic frameworks. *Chem. Mater.* **28**, 1489-1494 (2016).
42. Xu H., Tao S., Jiang D. Proton conduction in crystalline and porous covalent organic frameworks. *Nat. Mater.* **15**, 722-726 (2016).
43. Ma H., et al. Cationic covalent organic frameworks: A simple platform of anionic exchange for porosity tuning and proton conduction. *J. Am. Chem. Soc.* **138**, 5897-5903 (2016).
44. Huang N., Chen X., Krishna R., Jiang D. Two-dimensional covalent organic frameworks for carbon dioxide capture through channel-wall functionalization. *Angew. Chem. Int. Ed.* **54**, 2986-2990 (2015).
45. Huang N., Krishna R., Jiang D. Tailor-made pore surface engineering in covalent organic frameworks: Systematic functionalization for performance screening. *J. Am. Chem. Soc.* **137**, 7079-7082 (2015).
46. Qian H. L., Yang C. X., Yan X. P. Bottom-up synthesis of chiral covalent organic frameworks and their bound capillaries for chiral separation. *Nat. Commun.*, **7**, 12104 (2016).

47. Ding S. Y., *et al.* Construction of covalent organic framework for catalysis: Pd/COF-LZU1 in Suzuki-Miyaura coupling reaction. *J. Am. Chem. Soc.* **133**, 19816-19822 (2011).
48. Xu H., Gao J., Jiang D. Stable, crystalline, porous, covalent organic frameworks as a platform for chiral organocatalysts. *Nat. Chem.* **7**, 905-912 (2015).
49. Vyas V. S., *et al.* A tunable azine covalent organic framework platform for visible light-induced hydrogen generation. *Nat. Comm.* **6**, 8508 (2015).
50. Xu H. S., Ding S. Y., An W. K., Wu H., Wang W. Constructing crystalline covalent organic frameworks from chiral building blocks. *J. Am. Chem. Soc.* **138**, 11489-11492 (2016).
51. Wang X., Han X., Zhang J., Wu X., Liu Y., Cui Y. Homochiral 2D porous covalent organic frameworks for heterogeneous asymmetric catalysis. *J. Am. Chem. Soc.* **138**, 12332-12335 (2016).
52. Xu F., *et al.* Radical covalent organic frameworks: A general strategy to immobilize open-accessible polyradicals for high-performance capacitive energy storage. *Angew. Chem. Int. Ed.* **54**, 6814-6818 (2015).
53. DeBlase C. R., Silberstein K. E., Truong T. T., Abruna H. D., Dichtel W. R. β -ketoenamine-linked covalent organic frameworks capable of pseudocapacitive energy storage. *J. Am. Chem. Soc.* **135**, 16821-16824 (2013).
54. Zhu Y., Wan S., Jin Y., Zhang W. Desymmetrized vertex design for the synthesis of covalent organic frameworks with periodically heterogeneous pore structures. *J. Am. Chem. Soc.* **137**, 13772-13775 (2015).
55. Huang N., *et al.* Multiple-component covalent organic frameworks. *Nat. Commun.* **7**, 12325 (2016).
56. Qian C., Qi Q.-Y., Jiang G.-F., Cui F.-Z., Tian Y., Zhao X. Toward covalent organic frameworks bearing three different kinds of pores: The strategy for construction and COF-to-COF transformation via heterogeneous linker exchange. *J. Am. Chem. Soc.* **139**, 6736-6743 (2017).
57. Haase F., *et al.* Tuning the stacking behaviour of a 2D covalent organic

- framework through non-covalent interactions. *Mater. Chem. Front.* **1**, 1354-1361 (2017).
58. Vyas V. S., *et al.* Exploiting noncovalent interactions in an imine-based covalent organic framework for quercetin delivery. *Adv. Mater.* **28**, 8749-8754 (2016).
 59. Hasell T., Schmidtman M., Cooper A. I. Molecular doping of porous organic cages. *J. Am. Chem. Soc.* **133**, 14920-14923 (2011).
 60. Sava D. F., *et al.* Capture of volatile iodine, a gaseous fission product, by zeolitic imidazolate framework-8. *J. Am. Chem. Soc.* **133**, 12398-12401 (2011).
 61. Sun H., La P., Zhu Z., Liang W., Yang B., Li A. Capture and reversible storage of volatile iodine by porous carbon with high capacity. *J. Mater. Sci.* **50**, 7326-7332 (2015).
 62. Yin Z., Xu S., Zhan T., Qi Q., Wu Z., Zhao X. Ultrahigh volatile iodine uptake by hollow microspheres formed from a heteropore covalent organic framework. *Chem. Comm.* **53**, 7266-7269 (2017).
 63. Dang Q.-Q., Wang X.-M., Zhan Y.-F., Zhang X.-M. An azo-linked porous triptycene network as an absorbent for CO₂ and iodine uptake. *Polym. Chem.* **7**, 643-647 (2016).
 64. Sava D. F., *et al.* Competitive I₂ sorption by Cu-BTC from humid gas streams. *Chem. Mater.* **25**, 2591-2596 (2013).
 65. Sava D. F., Garino T. J., Nenoff T. M. Iodine confinement into metal–organic frameworks (MOFs): Low-temperature sintering glasses to form novel glass composite material (GCM) alternative waste forms. *Ind. Eng. Chem. Res.* **51**, 614-620 (2012).
 66. Mehlana G., Ramon G., Bourne S. A. A 4-fold interpenetrated diamondoid metal-organic framework with large channels exhibiting solvent sorption properties and high iodine capture. *Microporous Mesoporous Mater.* **231**, 21-30 (2016).
 67. Wang Y., Sotzing G. A., Weiss R. A. Sorption of iodine by polyurethane and melamine-formaldehyde foams using iodine sublimation and iodine solutions.

- Polymer* **47**, 2728-2740 (2006).
68. Zeng M.-H., et al. Rigid pillars and double walls in a porous metal-organic framework: Single-crystal to single-crystal, controlled uptake and release of iodine and electrical conductivity. *J. Am. Chem. Soc.* **132**, 2561-2563 (2010).
 69. Liu Q.-K., Ma J.-P., Dong Y.-B. Highly efficient iodine species enriching and guest-driven tunable luminescent properties based on a cadmium(II)-triazole MOF. *Chem. Comm.* **47**, 7185-7187 (2011).
 70. Lu J. Y., Babb A. M. A unique eclipsed 2-D coordination polymer with removable iodine molecules in the open-channel structure. *Chem. Comm.* **0**, 1346-1347 (2003).
 71. Yin Z., Wang Q.-X., Zeng M.-H. Iodine release and recovery, influence of polyiodide anions on electrical conductivity and nonlinear optical activity in an interdigitated and interpenetrated bipillared-bilayer metal-organic framework. *J. Am. Chem. Soc.* **134**, 4857-4863 (2012).
 72. Lang J.-P., Xu Q.-F., Yuan R.-X., Abrahams B. F. {[WS₄Cu₄(4,4'-bpy)₄][WS₄Cu₄I₄(4,4'-bpy)₂]}_∞—an unusual 3D porous coordination polymer formed from the preformed cluster [Et₄N]₄[WS₄Cu₄I₆]. *Angew. Chem. Int. Ed.* **43**, 4741-4745 (2004).
 73. Wang Z. M., Zhang Y. J., Liu T., Kurmoo M., Gao S. [Fe₃(HCOO)₆]: A permanent porous diamond framework displaying H₂/N₂ adsorption, guest inclusion, and guest-dependent magnetism. *Adv. Funct. Mater.* **17**, 1523-1536 (2007).
 74. Katsoulidis A. P., He J., Kanatzidis M. G. Functional monolithic polymeric organic framework aerogel as reducing and hosting media for Ag nanoparticles and application in capturing of iodine vapors. *Chem. Mater.* **24**, 1937-1943 (2012).
 75. Abrahams B. F., Moylan M., Orchard S. D., Robson R. Zinc saccharate: A robust, 3D coordination network with two types of isolated, parallel channels, one hydrophilic and the other hydrophobic. *Angew. Chem. Int. Ed.* **42**, 1848-1851

- (2003).
76. Gorbitz C. H., Nilsen M., Szeto K., Tangen L. W. Microporous organic crystals: An unusual case for l-leucyl-l-serine. *Chem. Comm.* **0**, 4288-4290 (2005).
 77. Palmgren A., Thorarensen A., Bäckvall J.-E. Efficient synthesis of symmetrical 2,5-disubstituted benzoquinones via palladium-catalyzed double negishi coupling. *J. Org. Chem.* **63**, 3764-3768 (1998).
 78. Kuhnert N., Rossignolo G. M., Lopez-Periago A. The synthesis of trianglimines: On the scope and limitations of the [3 + 3] cyclocondensation reaction between (1*R*,2*R*)-diaminocyclohexane and aromatic dicarboxaldehydes. *Org. Biomol. Chem.* **1**, 1157-1170 (2003).
 79. Stegbauer L., Schwinghammer K., Lotsch B. V. A hydrazone-based covalent organic framework for photocatalytic hydrogen production. *Chem. Sci.* **5**, 2789-2793 (2014).
 80. Gomes R., Bhanja P., Bhaumik A. A triazine-based covalent organic polymer for efficient CO₂ adsorption. *Chem. Comm.* **51**, 10050-10053 (2015).

**Chapter 5. Ionic Covalent Organic
Frameworks: Design of Charged Interface
Aligned on 1D Channel Walls and Its
Unusual Electric Functions**

Angew. Chem. Int. Ed. 2017, 56, 4982-4986

Ning Huang⁺, Ping Wang⁺, Matthew A. Addicoat, Thomas Heine,
and Donglin Jiang*

(+ These authors contributed equally to this work.)

Abstract Here I report a new ionic covalent organic framework (COF), which is constructed with benzimidazolium-functionalized edge units by formation of imine linkages. The COFs exhibit high surface area and adsorb a significant amount of CO₂ (up to 17.5 wt %, 273 K, 1 bar). Importantly, the materials show good thermal stabilities and excellent resistance to hydrolysis, remaining nearly intact after immersing in water or basic solution for 24 h. The presence of permanently immobilized ion centers in COFs enables the highly selective anionic dye adsorption ability. Our approach thus provides a convenient route to highly stable COFs with ionic linkers, which can potentially serve as absorbents for gas separation of N₂ and CO₂, and also for anionic dye capture.

5.1 Introduction

Covalent organic frameworks (COFs) are a fresh type of porous materials made from purely organic building blocks. The building units create periodically ordered nanoscopic pores through crystallization and are linked together by pure covalent bonds.¹⁻⁴ The periodically ordered monomer arrangement and aligned one-dimensional nanochannels characterize the two-dimensional (2D) COFs and make them different from other molecular architectures.⁵⁻¹⁰ These crystalline porous polymers are quite attractive for applications in various fields, including catalysis, gas adsorption, sensing, proton conduction and energy conversion and storage.¹¹⁻¹³ Although many kinds of COFs have been developed for corresponding functions, the ionic COFs have rarely been explored.¹⁴⁻¹⁷ The ionic nature could endow this kind of COFs with specific ion exchange property, which would greatly expand the applications of COFs in ion conduction, solid electrodes, and solid catalysis. Recently, two ionic COFs, ICOF-1 (REF. 14) and EB-COF:Br (REF. 15), were reported for high lithium and proton conduction, respectively. However, it still remains as a great challenge to develop a general strategy for the synthesis of high-crystalline and high-porosity ionic COFs. Herein, I reported the design and synthesis of a new benzimidazolium-based COF, which presented high porosity, excellent stability, high CO₂ uptake, and efficient capture of anionic dye pollutants.

5.2 Results and Discussion

5.2.1 COF Synthesis and Characterization

I demonstrated the concept by using imine-linked COFs as scaffolds, into which the benzimidazolium-functionalized edge units were introduced. I synthesized 4,4',4'',4'''-(pyrene-1,3,6,8-tetrayl) tetraaniline (PyTTA) bearing four amino groups as the vertices and 5,6-bis(4-formylbenzyl)-1,3-dimethyl-benzimidazolium bromide (BFBIm) as the edge units for the construction of ionic PyTTA-BFBIm-iCOF, in which the benzimidazolium docking sites were embedded in the channel walls. The condensation reaction was conducted in a mixed solvent of *n*-butanal and *o*-dichlorobenzene in the presence of acetic acid as catalyst under solvothermal

conditions at 120 °C. The resulting PyTTA-BFBI*m*-iCOF (Figure 5.1) was prepared as yellow powder with isolated yield of 82%. Various methods were employed for the characterization of the PyTTA-BFBI*m*-iCOF. Fourier-transform infrared (FT-IR) of PyTTA-BFBI*m*-iCOF showed the stretching vibration bands at 1624 cm⁻¹ that were assigned to the C=N bond (Figure 5.2). Elemental analysis of PyTTA-BFBI*m*-iCOF samples corroborated well with the theoretical values of infinite 2D sheet (Table 5.1). Field emission scanning electronic microscopy revealed that the PyTTA-BFBI*m*-iCOF adopted micrometer-scale spherical morphology (Figure 5.3a). High-resolution transmission electron microscopy allowed the direct visualization of quadrangular pores with widths of approximately 2.4 nm (Figure 5.3b). Thermal gravimetric analysis revealed that the PyTTA-BFBI*m*-iCOF was stable up to 450 °C under nitrogen (Figure 5.4).

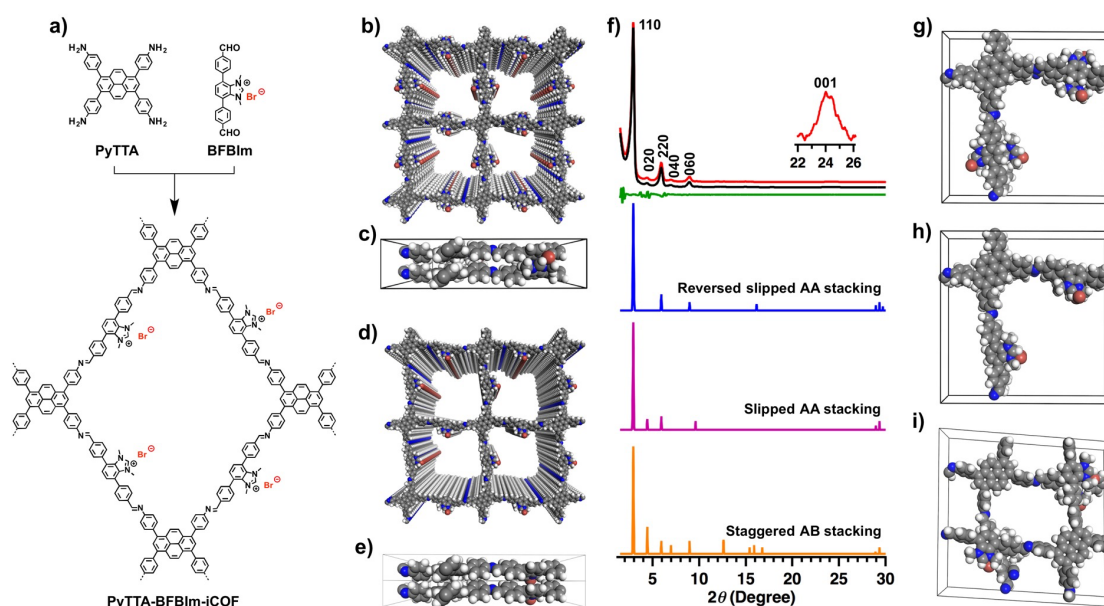


Figure 5.1¹ (a) Schematic representation of the synthesis of PyTTA-BFBI*m*-iCOF. (b) Top and (c) side views of the reversed slipped AA-stacking mode of PyTTA-BFBI*m*-iCOF (gray: C, orange: Br⁻, blue: N, white: H); (d) Top and (e) side views of slipped AA-stacking mode. (f) PXRD patterns of PyTTA-BFBI*m*-iCOF of experimentally observed (red), Pawley refined (black), their difference (green), simulated curves for reversed slipped AA-stacking mode (blue), slipped AA-stacking

mode (purple), and staggered AB-stacking mode (orange). Units cells of (g) reversed slipped AA, (h) slipped AA, and (i) staggered AB-stacking modes.

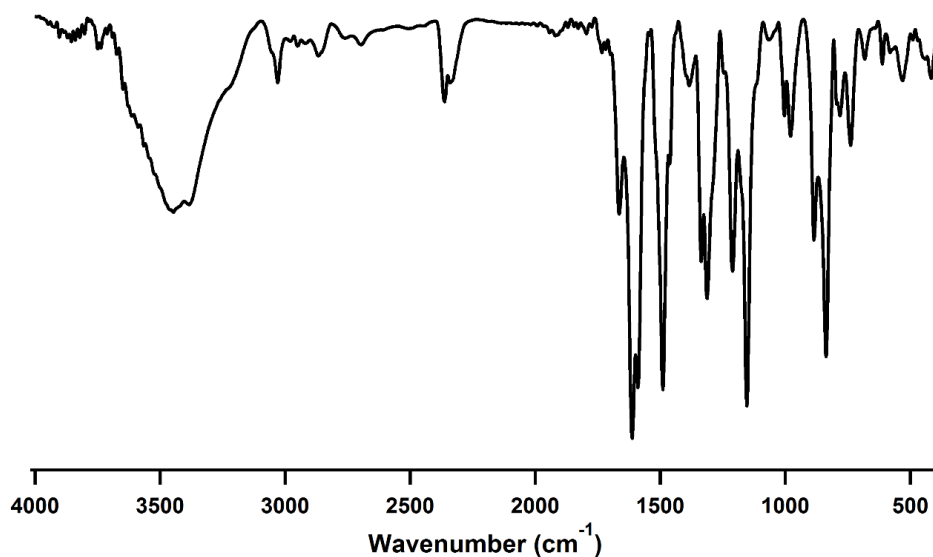


Figure 5.2¹ FT-IR spectra of PyTTA-BFBIIm-iCOF.

Table 5.1 Elemental analysis result of PyTTA-BFBIIm-iCOF.

COFs		C%	H%	N%
PyTTA-BFBIIm-iCOF	Calcd.	80.99	4.91	5.81
	Found	78.26	5.12	5.67

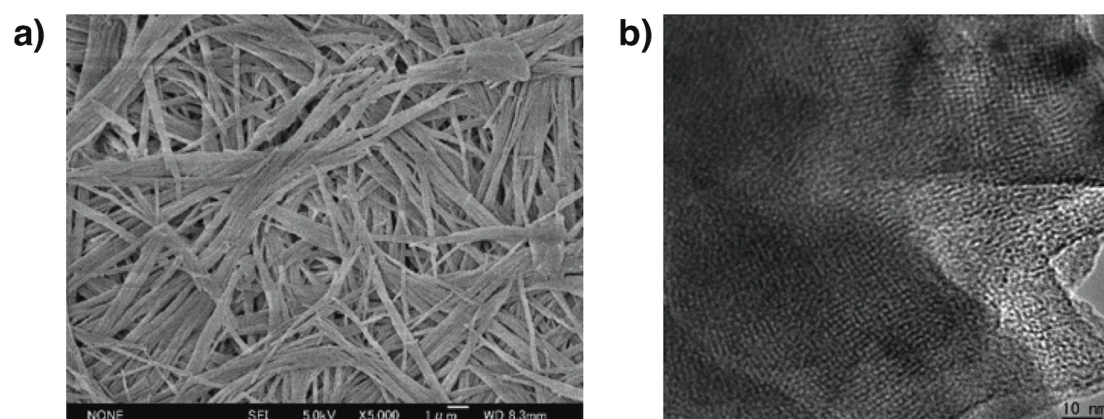


Figure 5.3¹ (a) FE-SEM and (b) HR-TEM image of PyTTA-BFBIIm-iCOF.

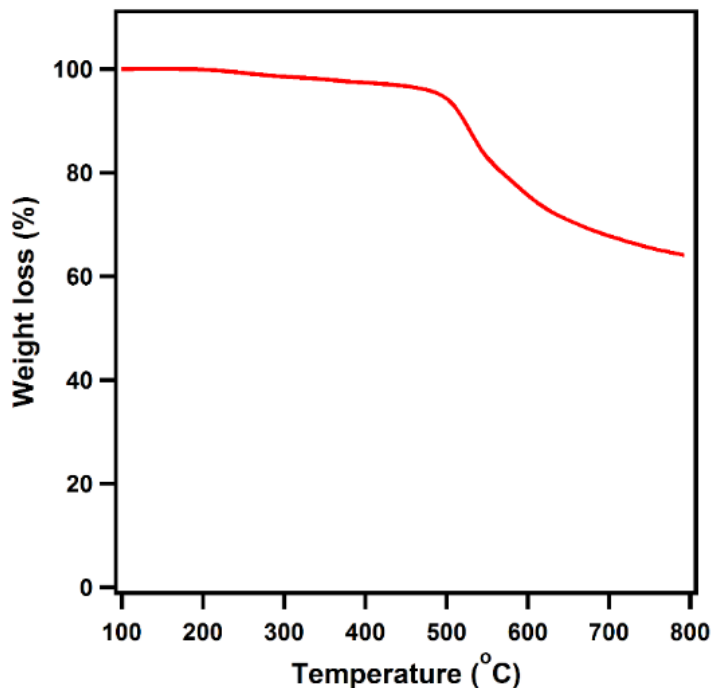


Figure 5.4¹ TGA curve of PyTTA-BFBIIm-iCOF.

The PyTTA-BFBIIm-iCOF samples are highly crystalline materials with strong powder X-ray diffraction (PXRD) signals. PyTTA-BFBIIm-iCOF exhibited diffraction peaks at 3.48, 5.14, 7.06, 10.60, 14.35, and 23.88, which were assignable to the (110), (020), (220), (040), (060), and (001) facets, respectively (Figure 5.1f, red curve). The presence of (001) facets indicates that the PyTTA-BFBIIm-iCOF has periodic orders in all three dimensions. The PXD peaks were assigned according to the Pawley-refined patterns (Figure 5.1f black curve) by minimizing the difference between the experimental and simulated data negligible (Figure 5.1f green curves). The starting structure was created by AuToGraFS. The model was firstly optimized by a topology-preserving force field to optimize the monolayer. In the next step, the simulation was further extended to layered frameworks in different stacking modes by the structural simulations using self-consistent charge density functional tight binding (SCC-DFTB) method. In the PyTTA-BFBIIm-iCOF, the reversed eclipsed AA stacking mode was the most stable structure among the various stacking modes, including slipped AA and staggered AB modes (Figures 5.1 b-e and Tables 5.2 and 5.3). The low total energy of the reversed AA stacking model may benefit from the slight slip

between layers avoiding cationic benzimidazolium centers directly on top of each other. I used the reversed slipped AA stacking mode to reconstruct the crystal structures of the PyTTA-BFBI*m*-iCOF (Figure 5.1g), and the resulting PXRD patterns (Figure 5.1f blue curve) were in agreement with the experimentally observed PXRD profiles. PyTTA-BFBI*m*-iCOF assumed the space group of *Pmm2* with $a = 24.46 \text{ \AA}$, $b = 28.61 \text{ \AA}$, $c = 7.44 \text{ \AA}$, and $\alpha = \beta = \gamma = 90^\circ$.

Table 5.2 The total DFTB energies, Lennard-Jones contributions (LJ), and the crystal stacking energies per monolayer as well as the corresponding HOMO-LUMO energy gap for the COF with ions directly stacked.

Stacking	c [Å]	Total DFTB Energy [a.u.]	LJ energy [a.u.]	Per unit crystal stacking energy [kcal.mol ⁻¹]	HOMO-LUMO gap [eV]
monolayer	–	-194.981502	0.8597	–	2.103
AA	4.22	-390.173951	1.4671	-66.19	1.604
slipAA-x	4.11	-390.209644	1.4543	-77.38	1.592
slipAA-y	4.10	-390.193766	1.4537	-72.40	1.591
AB	4.22	-390.0884799	1.5751	-39.37	1.896

Table 5.3 The total DFTB energies, Lennard-Jones contributions (LJ), and the crystal stacking energies per monolayer as well as the corresponding HOMO-LUMO energy gap for the COF with ions reverse stacked.

Stacking	c [Å]	Total DFTB Energy [a.u.]	LJ energy [a.u.]	Per unit crystal stacking energy [kcal.mol ⁻¹]	HOMO-LUMO gap [eV]
monolayer	–	-194.981502	0.8597	–	2.103
AA	3.93	-390.202981	1.4486	-75.29	1.515
slipAA-x	3.93	-390.199563	1.4484	-74.22	1.525
slipAA-y	4.06	-390.209507	1.4543	-77.34	1.612
AB	4.03	-389.9095654	1.5494	16.77	1.792

To investigate whether the 1D channels of the PyTTA-BFBI*m*-iCOF are accessible and their porosity, nitrogen sorption isotherm measurements at 77 K were conducted. The PyTTA-BFBI*m*-iCOF exhibited reversible type IV sorption curves (Figure 5.5a), which were characteristics of mesoporous materials. The Brunauer–Emmett–Teller (BET) surface areas were calculated to be as high as 1532 m² g⁻¹. This surface area is the highest for the ionic COFs reported based on N₂ sorption. The total pore volumes were estimated to be 0.7 cm³ g⁻¹. I evaluated the pore size distributions by using the nonlocal density function theory (NLDFT) method. The PyTTA-BFBI*m*-iCOF had one main peak centered at 2.3 nm (Figure 5.5b). These results indicate that the docking sites on the channel walls are accessible to guest molecules for supramolecular constructions.

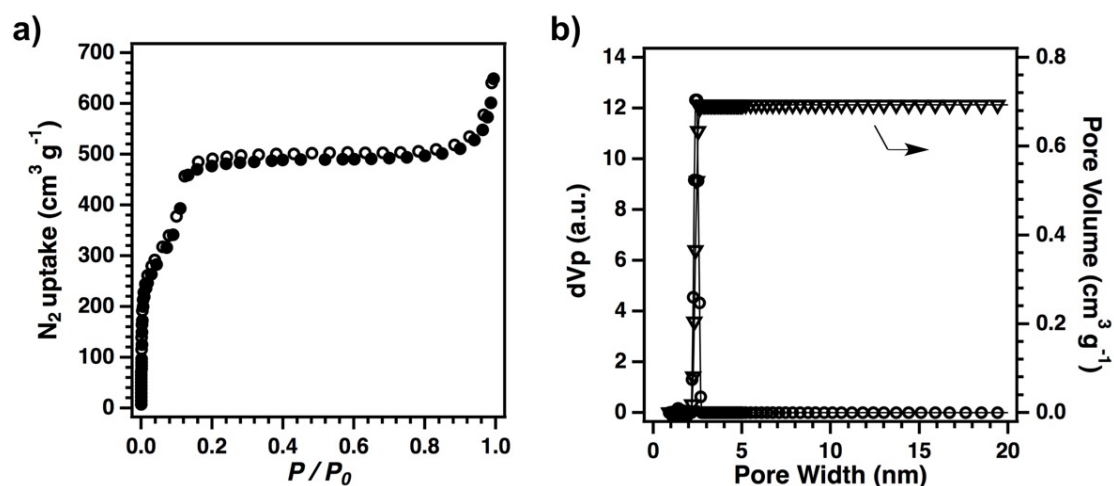


Figure 5.5¹ (a) Nitrogen sorption curves of PyTTA-BFBI*m*-iCOF at 77 K (filled circles for adsorption, open circles for desorption). (b) The pore size distribution and pore volume of PyTTA-BFBI*m*-iCOF.

To investigate the chemical stability of the PyTTA-BFBI*m*-iCOF, I dispersed the COF samples in different aqueous solutions, including N,N-dimethylformamide (DMF), boiling water, aqueous HCl (3 M) and NaOH (3 M) solutions at 25 °C for 24 h. The samples were collected, washed with water and THF, dried under vacuum at 120 °C for 12 h, and subjected to PXRD (Figure 5.6a) and N₂ sorption isotherm

measurements (Figure 5.6b). Surprisingly, all the samples exhibited intense PXRD patterns without any change in the peak position and intensity, indicating that the high crystallinity was retained under these harsh conditions (Figure 5.6a). Notably, the BET surface areas were also retained well upon the treatments under these harsh conditions (Figure 5.6b).

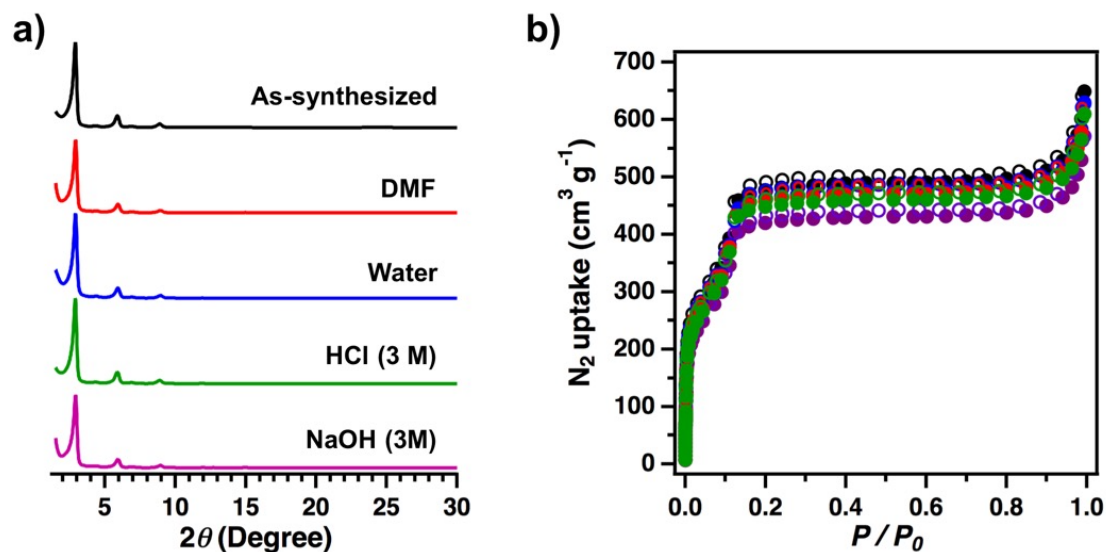


Figure 5.6¹ (a) PXRD patterns and (b) N₂ sorption curves of PyTTA-BFBIIm-iCOF upon 24-h treatment in different solvents (color in b is the same as that in a).

5.2.2 CO₂ Capture

For the sake of environment requirement, plenty porous materials are developed for CO₂ capture and separation. Other than porosity, chemical environment of the pores plays as another vital role for the determination of CO₂ uptake amount. For the COF related adsorbents, increasing the CO₂ affinity of COF nanochannels by deliberate pore functionalization has been proven a practical strategy.¹⁸⁻²¹ Ionic interfaces are supposed capable to enhance CO₂ uptake by exerting dipole-quadruple interactions towards CO₂ molecules. However, there is still no attempt being conducted using ionic COF as CO₂ adsorbents.

At 1.0 bar, the PyTTA-BFBIIm-iCOF uptooke CO₂ with high values of 93 mg g⁻¹ at 298 K and 177 mg g⁻¹ at 273 K (Figure 5.7a). The uptake capacity makes

PyTTA-BFBIm-iCOF a top COF material for CO₂ uptake reported to date, exceeding COF-5 (5.9 wt%),²² COF-102 (1.21 wt%),²² COF-103 (7.6 wt%),²² ILCOF-1 (6.0 wt%),²³ TDCOF-5 (9.2 wt%),²⁴ and is comparable to [HO₂C]_{100%}-H₂P-COF (17.4 wt%),¹⁹ TpPa-1 (15.6 wt%)²⁵ at 273 K and 1 bar. The Q_{st} curve was calculated from the isotherms and yielded a value of 30.2 kJ mol⁻¹ at low coverage (Figure 5.7b). By contrast, the PyTTA-TPhA-COF with no polar functional groups in the pores, exhibited a BET surface area of 1754 m² g⁻¹ and CO₂ capacity of 65 and 36 mg g⁻¹ at 273 K and 298 K (Figure 5.8). For CO₂ capture, the CO₂/N₂ separation is very important in flue gas separation. The N₂ uptake of PyTTA-BFBIm-iCOF at 273 K and 1 bar was 5.34 mg g⁻¹.

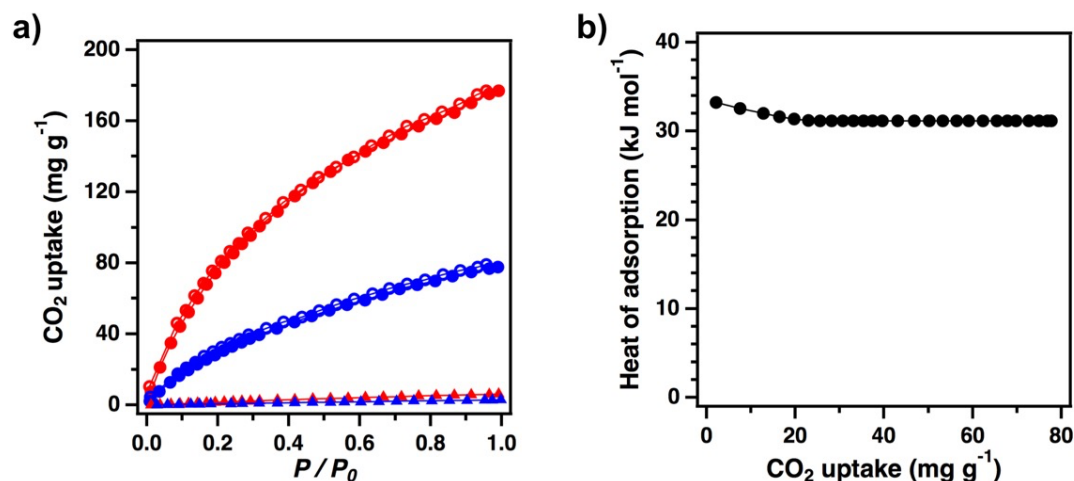


Figure 5.7¹ (a) CO₂ (circles) and N₂ (triangles) adsorptions at 273 K (red) and 298 K (blue). (b) Q_{st} value for CO₂ adsorption at low coverage.

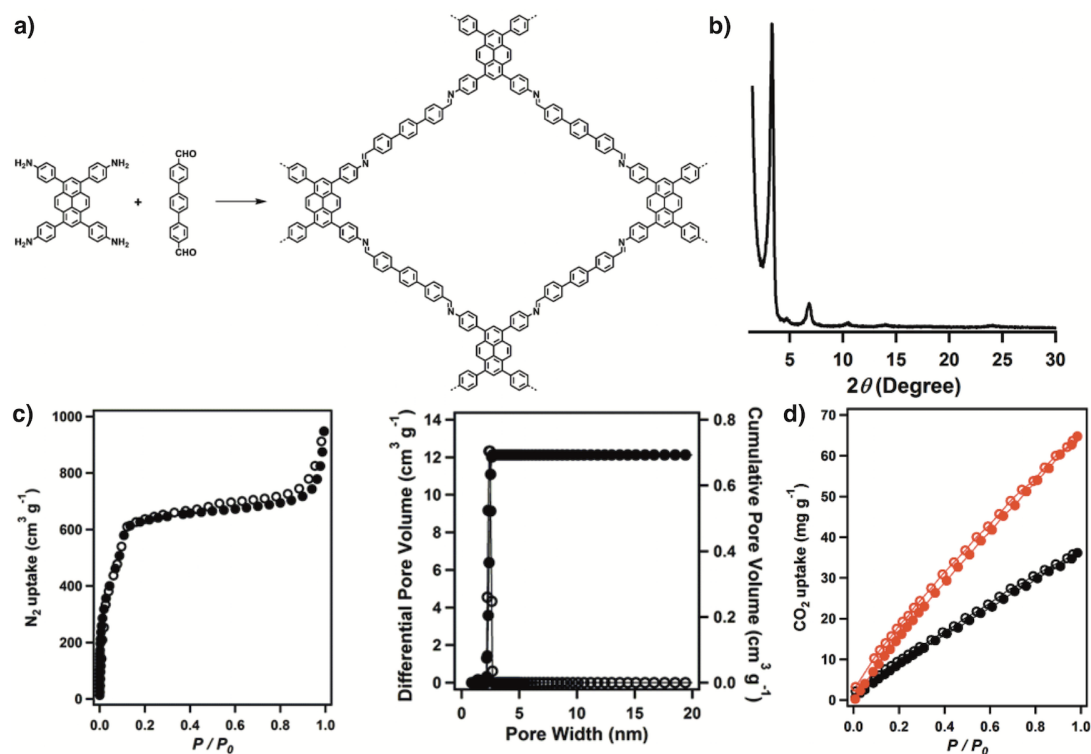


Figure 5.8¹ (a) Schematic representation of the PyTTA-TPhA-COF. (b) Powder XRD pattern of PyTTA-TPhA-COF. (c) N₂ adsorption isotherm (left) and pore size distribution (right) of PyTTA-TPhA-COF. (d) CO₂ sorption curves of of PyTTA-TPhA-COF at 273 K and 298 K (1 bar).

5.2.3 Ionic Pollutants Capture

In addition to the excellent CO₂ adsorption performance, the PyTTA-BFBIm-iCOF framework offers charged channels that are promising for the anionic dye pollutants capture. I found that the benzimidazolium units located at the edges provide open docking sites for ion exchange interactions with charged guest molecules. I investigated its capacity for capturing anionic dye pollutants of low concentrations from water by collecting the adsorption isotherms. The dye concentrations can be determined by measuring the UV spectra of the solution. Firstly, the anionic dye pollutant methyl orange (MO) was chosen as a model guest molecule, which was expected to replace the bromide ion on the skeleton of PyTTA-BFBIm-iCOF via ion exchange. The saturated MO removal capacity of the PyTTA-BFBIm-iCOF was calculated to be 553 mg g⁻¹ (Figure 5.9a and b). This

capacity is equivalent to 0.81 MO ion per benzimidazolium group in the PyTTA-BFBI*m*-iCOF, suggesting the high accessibility of the benzimidazolium groups to the MO ions. To the best of our knowledge, the maximum MO uptake capacity of PyTTA-BFBI*m*-iCOF is the highest among adsorbent materials reported thus far for MO adsorption, and is significantly higher than that of some benchmark porous materials, for example, nano-size SiO₂-Al₂O₃ mixed oxides (381 mg g⁻¹),²⁶ nanostructured proton-containing H- δ -MnO₂ nanoparticles (427 mg g⁻¹),²⁷ alkali-activated multiwalled carbon nanotube CNTs-A (149 mg g⁻¹),²⁸ and NH₂-MIL-101(Al) (199 mg g⁻¹).²⁹ The resulting equilibrium adsorption isotherm was well fitted with Langmuir model that yielded a high correlation coefficient ($R^2 > 0.999$) (Figure 5.9c). The effect of contact time on the adsorption of MO over PyTTA-BFBI*m*-iCOF was investigated and the changes of adsorbed amount with time are treated with the pseudo-second-order kinetic model (Figure 5.9d, e). According to pseudo-second-order kinetic model, the calculated kinetic constant (k) and correlation coefficient (R) were $9.32 \times 10^{-4} \text{ g mg}^{-1} \text{ min}^{-1}$ and 0.998, respectively. The adsorption kinetic constant for MO adsorption over PyTTA-BFBI*m*-iCOF is larger than the constants over other porous materials, including activated carbon ($2.17 \times 10^{-4} \text{ g mg}^{-1} \text{ min}^{-1}$),³⁰ MOF-235 ($7.67 \times 10^{-4} \text{ g mg}^{-1} \text{ min}^{-1}$),³¹ and PED-MIL-101 ($2.75 \times 10^{-3} \text{ g mg}^{-1} \text{ min}^{-1}$).³⁰

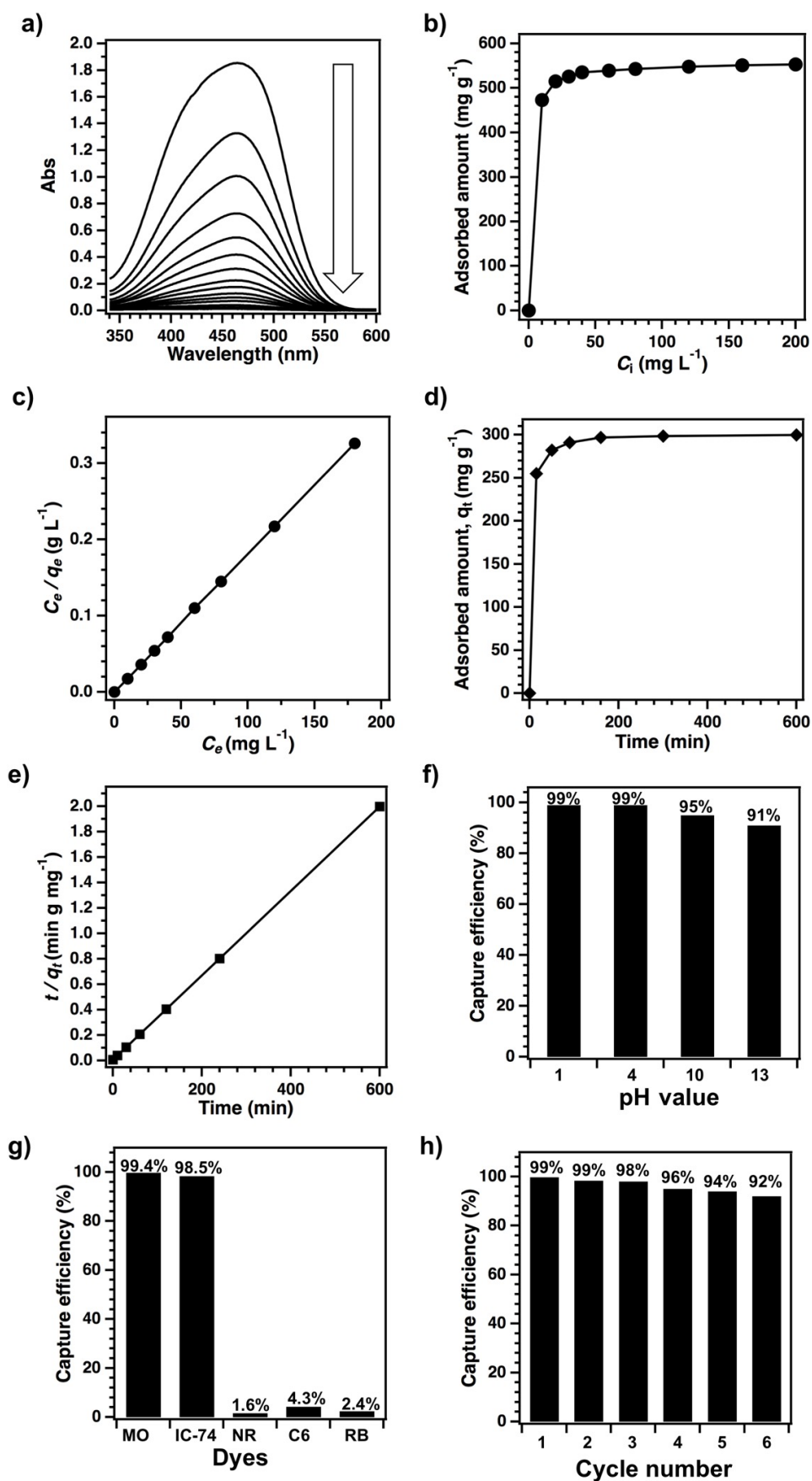


Figure 5.9¹ (a) Time-dependent electronic adsorption spectral change (from top: 0

min, 1 min, 2 min, 3 min, 5 min, 10 min, 12 min, 15 min, 20 min, 30 min, 1 h, 2 h, 3 h, 5 h, 10 h) of an ethanol/water solution (1/1 by vol., 15 mL) of MO at initial concentration of 200 mg L^{-1} upon addition of PyTTA-BFBI*m*-iCOF (5 mg). (b) Adsorption isotherm of MO. (c) Linear regression using Langmuir adsorption model. (d) Effect of contact time on the MO adsorption at initial concentration of 30 mg L^{-1} . (e) Pseudo-second-order kinetics of MO adsorption. (f) Capture efficiency of MO at different pH values. (g) Capture efficiency of different dyes. (h) Cycle performance.

The chemical stability under various harsh conditions was also verified for the PyTTA-BFBI*m*-iCOF. This stability feature is an important advantage over silica- or MOFs-based adsorbents that easily suffer from the loss of porous structures under such harsh conditions. The PyTTA-BFBI*m*-iCOF retained outstanding removal efficiency at acidic conditions, whereas the MO concentrations could be captured with same efficiency of 99% at the pH values of 1 and 4 (Figure 5.9f). Under basic conditions, the removal efficiencies were 95% and 91% at pH values of 10 and 13, respectively (Figure 5.9f). The amounts of adsorbed MO decreased slightly with increasing the pH of the MO solution, which might be due to the fact that the enhanced negative charged hydroxyl competed with anionic dyes in ion exchange process. Structure instability under harsh conditions and deteriorated capacity over a broad pH range have been the barrier for other porous materials. As shown above, these challenging issues have been well addressed by designing a suitable ionic COF structure. Therefore, the PyTTA-BFBI*m*-iCOF represents an innovative porous material with outstanding performance in removing MO from aqueous solutions.

The PyTTA-BFBI*m*-iCOF can selectively adsorb anionic dyes rather than the neutral and cationic dyes. As shown in Figure 5.9g, the PyTTA-BFBI*m*-iCOF could effectively adsorb anionic MO and dianionic indigo carmine acid blue 74 (IC) with efficiency of 99.4% and 98.5%, respectively. However, the PyTTA-BFBI*m*-iCOF was not active for removal of neutral and cationic dyes, such as Nile Red (NR), Coumarin 6 (C6), and Rhodamine B (RB), with 1.6%, 4.3% and 2.4% efficiencies, respectively.

Therefore, decorating the pore walls with benzimidazolium units renders the COF able to trap anionic dye ions in a highly selective manner. Notably, the MO-captured PyTTA-BFBI*m*-iCOF was easily regenerated upon soaking with an aqueous NaBr solution (1.0 M) after 48 h, which resulted in nearly quantitatively (97%) desorbed PyTTA-BFBI*m*-iCOF. The regenerated COF was then subjected to the next round MO removal. Notably, the PyTTA-BFBI*m*-iCOF retained 92% of the original capacity even after six cycles (Figure 5.9h).

5.3 Conclusion

In summary, I have designed and synthesized a charged COF for challenging important environmental issues, in particular the CO₂ adsorption and removal of anionic pollutants from aqueous solutions. Through the systematic design of the skeletons, pore size, and pore walls, the resulting COF exhibits high surface areas, excellent chemical stability and uniform positively charged frameworks. The charged pore walls contribute to the enhanced CO₂ capacity via dipole–quadrupole interactions between CO₂ and charged frameworks. In addition, the high surface area, chemical stability together with mesoporosity render the charged COF outstanding platform for efficient adsorption of anionic pollutants. These properties suggest the cationic open COF framework can be an effective platform for CO₂ adsorption and ion exchange. These elaborate controls over the COF structures lead to the generation of an innovative system for the CO₂ and anionic pollutants capture. The outstanding ion exchange performance sets a benchmark material based on COFs for the anionic dye removal from water and suggests the great potential of COFs for challenging environment issue.

5.4 Experimental Sections

5.4.1 Methods

JEOL models JNM-LA400 NMR spectrometers were used to measure the ¹H nuclear magnetic resonance (NMR) spectra. Using the solvent residual proton peaks as reference, the chemical shifts (δ in ppm) of compounds are confirmed. A JASCO model FT-IR-6100 infrared spectrometer was used to determine the Fourier transform

infrared (FT-IR) spectra. The Rigaku model RINT Ultima III diffractometer was used to confirm the crystallinity character by the Powder X-ray diffraction (PXRD) data. In detail, the sample powder was deposited on glass substrate and the measure starts from $2\theta = 2.5^\circ$ up to 30° with 0.02° increment. At 77 K created by liquid nitrogen, a Micromeritics Instrument Corporation model 3Flex surface characterization analyzer was used to measure the nitrogen sorption isotherms. The specific surface areas and the pore distribution was confirmed by the Brunauer-Emmett-Teller (BET) method and the non-local density functional theory (NLDFT) model, respectively. A Bel Japan Inc. model BELSORP-mini II analyzer was used to confirm the carbon dioxide sorption isotherms. For the isotherm measurements, all the samples were degassed in vacuum at 120°C for more than 10 h. A Mettler-Toledo model TGA/SDTA851e was used to measure the TGA curves in nitrogen atmosphere at a rate of $10^\circ\text{C min}^{-1}$. The JEOL model JSM-6700 was used for field-emission scanning electron microscopy (FE-SEM). The operation is conducted at an accelerating voltage of 5.0 kV. To improved sample conductivity, before measure, the sample was coated by gold after drop-casting its acetone suspension on mica substrate.

The crystalline structures of COFs were determined using the density-functional tight-binding (DFTB⁺) method including Lennard-Jones (LJ) dispersion. The DFTB⁺ program package version 1.2 was uses for the structure simulation and calculation. The Coulombic interaction between partial atomic charges was determined using the self-consistent charge (SCC) formalism. The van der Waals (vdW) was described by the Lennard-Jones type dispersion. AuToGraFS was used initially to create the π -stacking interactions and the simulation was further optimized by a topology-preserving force field. The monolayer structure was then extended to layered frameworks with different stacking modes. The lattice dimensions were optimized simultaneously with the geometry. Standard DFTB parameters for X-Y element pair (X, Y = C, H, N, and Br) interactions were employed from the mio-0-1 set10. The Monte Carlo integration technique was used to calculate the surface areas were calculated by using nitrogen as probe molecule (diameter = 3.68 \AA) and the

guest molecules are allowed to roll over the framework surface. The layers are stacking in the interval of 0.25 Å. The XRD pattern was simulated using the MS modeling version 4.4 (Accelrys Inc.). The lattice parameter optimization was performed until the R_p and R_{WP} values of Pawley refinement converge with the final R_{WP} and R_p values were 7.23% and 5.57%, respectively. The pseudo-Voigt profile function was used for whole profile fitting and Berrar-Baldinozzi function was used for asymmetry correction during the refinement processes.

The equilibrium adsorption capacity q_e is calculated according to the following equation: $q_e = (C_i - C_e) V/m$, in which C_i and C_e (mg L^{-1}) are the initial and equilibrium concentration of dyes, respectively, V (L) is the volume of the solution, and m (g) is the mass of adsorbent.

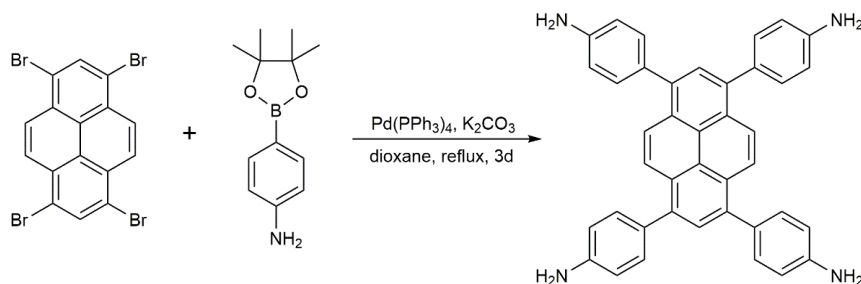
The experimental data is fitted with the Langmuir model using the following equation: $C_e/q_e = 1/(q_m K) + C_e/q_m$, in which q_e (mg g^{-1}) is the amount of dye adsorbed per unit mass of the adsorbent at the equilibrium point, C_e (mg L^{-1}) is the solute equilibrium concentration, q_m (mg g^{-1}) is the maximum adsorption amount at equilibrium and K (L mg^{-1}) is the Langmuir constant.

The efficiency of PyTTA-BFBIm-iCOF as adsorbent for removing dyes from aqueous solutions has been examined by investigating the adsorption kinetics of PyTTA-BFBIm-iCOF (5.0 mg) in 30 p.p.m. solutions of various dyes (50.0 mL). The experimental data is fitted with the pseudo-second-order kinetic model using the following equation: $t/q_t = t/q_e + 1/(k q_e^2)$, in which k ($\text{g mg}^{-1} \text{min}^{-1}$) is the rate constant of pseudo-second-order adsorption, q_t (mg g^{-1}) is the amount of dyes adsorbed at time t (min), and q_e (mg g^{-1}) is the amount of dyes adsorbed at equilibrium.

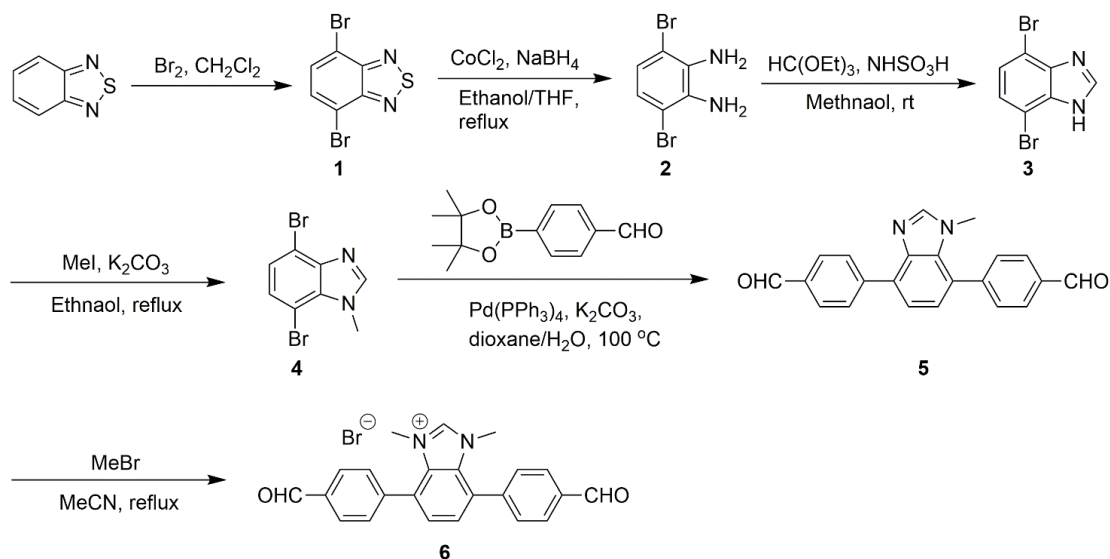
Adsorption experiments. In a typical experiment, PyTTA-BFBIm-iCOF was dispersed into an ethanol/water (1/1 by vol.) solution of different dyes at fixed concentration. The UV-vis spectra of the solution were recorded after stirring for 2 min and standing for 10 min at room temperature. The adsorption of dyes was then recorded and used to calculate the amount of dyes that was adsorbed by PyTTA-BFBIm-iCOF.

Desorption experiments. In a typical experiment, dye-adsorbed PyTTA-BFBI*m*-iCOF (5 mg) was immersed and dispersed into an aqueous solution of NaBr (1M, 10 mL) after sonication for 10 min. The dispersed dye-adsorbed PyTTA-BFBI*m*-iCOF was stirred at room temperature for 48 h. The UV-Vis spectra of the solution were recorded after stirring for 2 min and then standing for 10 min. The sorption of the released dyes was recorded and used to calculate the amount of released dyes absorbed PyTTA-BFBI*m*-iCOF.

5.4.2 Synthetic Procedures



4,4',4'',4'''-(Pyrene-1,3,6,8-tetrayl) tetraaniline (PyTTA). PyTTA was synthesized according to a literature method with modification.³² 1,3,6,8-Tetrabromopyrene (500 mg, 0.96 mmol), 4-(4,4,5,5-tetramethyl-1,3,2-dioxaborolan-2-yl)aniline (1.27 g, 5.8 mmol), palladium tetrakis(triphenylphosphine) (0.06 g, 0.05 mmol), and potassium carbonate (1.05 g, 7.6 mmol) in dioxane (15 mL) were stirred under reflux in N₂ for 3 days. After cooling to room temperature, the solid was removed by filtration, and washed with THF for 3 times. The organic phase was evaporated and the crude product was purified by column chromatography over silica gel with chloroform/acetone (9/1 by vol. to pure acetone) eluent. The obtained solid was further purified by recrystallization from chloroform/acetone to afford PyTTA in 75% yield. ¹H NMR (DMSO-d₆, 400 MHz): δ (ppm) 8.09 (s, 4H), 7.75 (s, 2H), 7.32-7.29 (d, 8H), 6.74-6.72 (d, 8H), 5.28 (s, 8H).



4,7-Dibromobenzothiadiazole (1). The compound 1 was synthesized according to a modified literature method.³³ To a 500 mL two-necked round-bottomed flask were added benzothiadiazole (10.0 g, 73.4 mmol) and HBr (150 mL, 48 %). A solution containing Br₂ (35.2 g, 220.3 mmol) in HBr (100 mL) was added very slowly. If necessary, an additional 100 mL of HBr can be added to the solution. After the total addition of Br₂, the solution was heated at reflux for 6 h. Precipitation of a dark orange solid was noted. The mixture was cooled to room temperature, and a sufficient amount of a saturated solution of NaHSO₃ was added to completely consume any excess Br₂. The mixture was filtered under vacuum and washed exhaustively with water. The solid was then washed once with cold Et₂O and dried under vacuum for ca. 20 h to afford 1 in 97 % yield (20.5 g, 69.8 mmol). ¹H NMR (400 MHz, CDCl₃/DMSO-d₆, 8:2): δ = 7.73 (s, 2 H) ppm.

4,5-Dibromo-1,2-benzenediamine (2). To a 2000 mL flask were added 1 (20.5 g, 70 mmol), CoCl₂ (91 mg, 0.7 mmol), THF (200 mL) and EtOH (450 mL). The mixture was refluxed. NaBH₄ (2.65 g, 70 mmol for each portion) was added three times (total 8.0 g) every hour. (Be careful! Add slowly. Exothermic nature of the reaction tends to cause bumping. Gas evolution was also observed.) After consumption of 1 was confirmed by TLC analysis, the mixture was cooled to room temperature. After addition of water (300 mL) and vigorous stirring for 10 min, gummy precipitate was filtered off using Celite. Organic solvent was evaporated and

product was extracted with dichloromethane three times. Combined organic layer was washed with water and brine and dried over MgSO_4 . The extract was filtered off, evaporated, and the crude mixture was purified with short pad silica gel chromatography (eluent: hexane/acetone = 5/1). Combined solution was evaporated to give 2 as an orange solid.

5,6-Dibromobenzimidazole (3). Obtained diamine 2 was immediately used for the next step. To the diamine dissolved in MeOH (350 mL) were added $\text{HC}(\text{OEt})_3$ (13.9 mL, 84 mmol) and sulfamic acid (340 mg, 3.5 mmol). The mixture was stirred overnight and powder precipitate formed. Solvent was evaporated and the residue was rinsed with ether. Drying under air gave 3 as a yellow powder (10.1 g, 55% yield for 2 steps). ^1H NMR (400 MHz, DMSO-d_6): δ = 7.35 (s, 2H), 8.36 (s, 1 H), 13.2 (brs, 1H); ^{13}C NMR (100 MHz, DMSO-d_6): δ = 113.75, 126.21, 132.75, 144.05; IR (KBr, cm^{-1}) ν = 630, 792, 912, 956, 1163, 1217, 1259, 1284, 1340, 1381, 1433, 1489, 1616, 2823, 3062; $[\text{M}]^+$ $\text{C}_7\text{H}_4\text{Br}_2\text{N}_2^+$ m/z = 276.

5,6-Dibromo-1-methyl-1H-Benzimidazole (4). To a 1000 mL flask were added 3 (19.7 g, 71.4 mmol), K_2CO_3 (29.6 g, 214 mmol) and EtOH (500 mL). The mixture was heated at reflux. To the hot mixture, MeI (8.8 mL, 142.8 mmol) was added dropwise and the mixture was maintained at reflux for 1 h. After consumption of 3 was confirmed by TLC analysis, the mixture was cooled to room temperature. After addition of water (200 mL) and evaporation of EtOH, the powdered precipitate was collected, washed with water and hexane/ Et_2O (1/1), and dried to give 4 as a brown powder (21.0 g, 100% yield). ^1H NMR (400 MHz, DMSO-d_6): δ = 4.05 (s, 3H), 7.34 (s, 2H), 8.32 (s, 1H).

5,6-Bis(4-formylbenzyl)-1-methyl-1H-benzimidazole (5). The stirred solution of 4 (1.93 g, 6.67 mmol), 4-(4,4,5,5-tetramethyl-1,3,2-dioxaborolan-2-yl)benzaldehyde (4.67 g, 15.35 mmol), $\text{Pd}(\text{PPh}_3)_4$ (385 mg, 0.33 mmol) and K_2CO_3 (2.76 g, 20 mmol) in 50 mL of 1,4-dioxane and 12 mL of water was heated to 100 °C under nitrogen atmosphere. Stirring was continued overnight, and then the mixture was cooled to room

temperature. Water was added and organic compounds were extracted with ethyl acetate three times. The combined organic layer was washed with brine and dried over MgSO_4 . The extract was filtered through short pad basic aluminum oxide and evaporated. The obtained residue was rinsed with hexane/ Et_2O (2/1) to give 5 as a brown powder (2.0 g, 72% yield). ^1H NMR (400 MHz, CDCl_3): δ = 1.62 (s, 9H), 1.64 (s, 9H), 3.42 (s, 3H), 7.23 (d, J = 7.6 Hz, 1H), 7.49 (d, J = 7.6 Hz, 1H), 7.52 (d, J = 8.1 Hz, 2H), 7.87 (s, 1H), 8.05-8.16 (m, 6H).

5,6-Bis(4-formylbenzyl)-1,3-dimethyl-benzimidazolium bromide (6). A solution of 5 (570 mg, 1.17 mmol) and MeBr (0.73 mL, 11.7 mmol) in 12 mL of acetonitrile was heated to reflux and stirred overnight. After cooling the mixture to room temperature, volatiles were evaporated. The obtained residue was rinsed with hexane/ethyl acetate (2/1) to give 6 as a brown powder (689 mg, 93% yield). ^1H NMR (400 MHz, CDCl_3): δ = 3.67 (s, 6H), 7.41 (s, 2H), 7.53 (d, J = 6.6 Hz, 4H), 8.10 (d, J = 6.6 Hz, 4H), 9.86 (s, 2H), 10.64 (s, 1H).

PyTTA-BFBIm-iCOF. An *o*-DCB/*n*-BuOH (0.5 mL/0.5 mL) mixture of 4,4',4'',4'''-(pyrene-1,3,6,8-tetrayl) tetraaniline (0.02 mmol, 11.3 mg) and 5,6-bis(4-formylbenzyl)-1,3-dimethyl-benzimidazolium bromide (0.04 mmol, 7.8 mg) was added into a Pyrex tube (10 mL) and the tube was degassed by three freeze-pump-thaw cycles. The tube was sealed and stored at 120 °C for 3 days. The precipitate was collected by centrifugation, and washed by THF. The powder sample was dried at 120 °C under vacuum for 12 h to give the yellow PyTTA-BFBIm-iCOF in an isolated yield of 82%.

5.5 References

1. This chapter is from my paper: Huang N.⁺, Wang P.⁺, Addicoat M., Heine T. and Jiang D. *Angew. Chem. Int. Ed.* 2017, **56**, 4982-4986.
2. Feng X., Ding X., Jiang D. Covalent organic frameworks. *Chem. Soc. Rev.* **41**, 6010-6022 (2012).
3. Huang N., Wang P., Jiang D. Covalent organic frameworks: A materials platform for structural and functional designs. *Nat. Rev. Mater.* **1**, 16068 (2016).

4. Diercks C. S., Yaghi O. M. The atom, the molecule, and the covalent organic framework. *Science* **355**, 923-930 (2017).
5. Ascherl L., *et al.* Molecular docking sites designed for the generation of highly crystalline covalent organic frameworks. *Nat. Chem.* **8**, 310-316 (2016).
6. Mulzer C. R., *et al.* Superior charge storage and power density of a conducting polymer-modified covalent organic framework. *ACS. Cent. Sci.* **2**, 667-673 (2016).
7. Dalapati S., Jin E., Addicoat M., Heine T., Jiang D. Highly emissive covalent organic frameworks. *J. Am. Chem. Soc.* **138**, 5797-5800 (2016).
8. Zhu Y., Wan S., Jin Y., Zhang W. Desymmetrized vertex design for the synthesis of covalent organic frameworks with periodically heterogeneous pore structures. *J. Am. Chem. Soc.* **137**, 13772-13775 (2015).
9. Huang N., Ding X., Kim J., Ihee H., Jiang D. A photoresponsive smart covalent organic framework. *Angew. Chem. Int. Ed.* **54**, 8704-8707 (2015).
10. Vyas V. S., *et al.* A tunable azine covalent organic framework platform for visible light-induced hydrogen generation. *Nat. Commun.* **6**, 8508 (2015).
11. Huang N., *et al.* Multiple-component covalent organic frameworks. *Nat. Commun.* **7**, 12325 (2016).
12. Pang Z. F., Xu S. Q., Zhou T. Y., Liang R. R., Zhan T. G., Zhao X. Construction of covalent organic frameworks bearing three different kinds of pores through the heterostructural mixed linker strategy. *J. Am. Chem. Soc.* **138**, 4710-4713 (2016).
13. Crowe J. W., Baldwin L. A., McGrier P. L. Luminescent covalent organic frameworks containing a homogeneous and heterogeneous distribution of dehydrobenzoannulene vertex units. *J. Am. Chem. Soc.* **138**, 10120-10123 (2016).
14. Du Y., *et al.* Ionic covalent organic frameworks with spiroborate linkage. *Angew. Chem. Int. Ed.* **55**, 1737-1741 (2016).
15. Ma H., *et al.* Cationic covalent organic frameworks: A simple platform of

- anionic exchange for porosity tuning and proton conduction. *J. Am. Chem. Soc.* **138**, 5897-5903 (2016).
16. Yu S.-B., *et al.* A polycationic covalent organic framework: A robust adsorbent for anionic dye pollutants. *Polym. Chem.* **7**, 3392-3397 (2016).
 17. Oisaki K., Li Q., Furukawa H., Czaja A. U., Yaghi O. M. A metal-organic framework with covalently bound organometallic complexes. *J. Am. Chem. Soc.* **132**, 9262-9264 (2010).
 18. Zeng Y., Zou R., Zhao Y. Covalent organic frameworks for CO₂ capture. *Adv. Mater.* **28**, 2855-2873 (2016).
 19. Huang N., Chen X., Krishna R., Jiang D. Two-dimensional covalent organic frameworks for carbon dioxide capture through channel-wall functionalization. *Angew. Chem. Int. Ed.* **54**, 2986-2990 (2015).
 20. Huang N., Krishna R., Jiang D. Tailor-made pore surface engineering in covalent organic frameworks: Systematic functionalization for performance screening. *J. Am. Chem. Soc.* **137**, 7079-7082 (2015).
 21. Stegbauer L., *et al.* Tunable water and CO₂ sorption properties in isostructural azine-based covalent organic frameworks through polarity engineering. *Chem. Mater.* **27**, 7874-7881 (2015).
 22. Furukawa H., Yaghi O. M. Storage of hydrogen, methane, and carbon dioxide in highly porous covalent organic frameworks for clean energy applications. *J. Am. Chem. Soc.* **131**, 8875-8883 (2009).
 23. Rabbani M. G., Sekizkardes A. K., Kahveci Z., Reich T. E., Ding R., El-Kaderi H. M. A 2D mesoporous imine-linked covalent organic framework for high pressure gas storage applications. *Chem. Eur. J.* **19**, 3324-3328 (2013).
 24. Kahveci Z., Islamoglu T., Shar G. A., Ding R., El-Kaderi H. M. Targeted synthesis of a mesoporous triptycene-derived covalent organic framework. *CrystEngComm* **15**, 1524-1527 (2013).
 25. Kandambeth S., Mallick A., Lukose B., Mane M. V., Heine T., Banerjee R. Construction of crystalline 2D covalent organic frameworks with remarkable

- chemical (acid/base) stability via a combined reversible and irreversible route. *J. Am. Chem. Soc.* **134**, 19524-19527 (2012).
26. Arshadi M., Salimi Vahid F., Salvacion J. W. L., Soleymanzadeh M. A practical organometallic decorated nano-size $\text{SiO}_2\text{-Al}_2\text{O}_3$ mixed-oxides for methyl orange removal from aqueous solution. *Appl. Surf. Sci.* **280**, 726-736 (2013).
27. Liu Y., Luo C., Sun J., Li H., Sun Z., Yan S. Enhanced adsorption removal of methyl orange from aqueous solution by nanostructured proton-containing $\delta\text{-MnO}_2$. *J. Mater. Chem A* **3**, 5674-5682 (2015).
28. Ma J., *et al.* Enhanced adsorptive removal of methyl orange and methylene blue from aqueous solution by alkali-activated multiwalled carbon nanotubes. *ACS Appl. Mater. Interfaces* **4**, 5749-5760 (2012).
29. Haque E., Lo V., Minett A. I., Harris A. T., Church T. L. Dichotomous adsorption behaviour of dyes on an amino-functionalised metal-organic framework, amino-MIL-101(Al). *J. Mater. Chem. A* **2**, 193-203 (2014).
30. Haque E., *et al.* Adsorptive removal of methyl orange from aqueous solution with metal-organic frameworks, porous chromium-benzenedicarboxylates. *J. Hazard. Mater.* **181**, 535-542 (2010).
31. Haque E., Jun J. W., Jhung S. H. Adsorptive removal of methyl orange and methylene blue from aqueous solution with a metal-organic framework material, iron terephthalate (MOF-235). *J. Hazard. Mater.* **185**, 507-511 (2011).
32. Chen X., Huang N., Gao J., Xu H., Xu F., Jiang D. Towards covalent organic frameworks with predesignable and aligned open docking sites. *Chem. Commun.* **50**, 6161-6163 (2014).
33. Mancilha F. S., *et al.* Are molecular 5,8- π -extended quinoxaline derivatives good chromophores for photoluminescence applications? *Eur. J. Org. Chem.* 4924-4933 (2006).

Chapter 6. Summary and Perspectives

Covalent organic frameworks (COFs) have emerged as a tailor-made platform for designing two-dimensional polymers. Here, I summarized my research work in the three years on the design and synthesis of COFs for molecular adsorption and separation.

In chapter 1, I introduced the field by reviewing the general aspects of COFs. The significant feature of COFs is that their designability; that is, the geometry and dimension of building blocks can be controlled to direct the topological evolution of structural periodicity. The diversity of building blocks, covalent linkages and topology schemes make COFs an emerging materials platform for structural control and functional design. I summarized the major progress in the field of COFs and recent achievements in developing new design principles and synthetic strategies. The cutting-edge strategies for functional design were highlighted.

In chapter 2, I designed and synthesized a series of microporous COFs with triangular topology and dual-pore structure. These triangular COFs were synthesized by condensation of hexa-substituted triphenylene unit as the vertices with the di-substituted linkers as the edges. The resulting COFs provided dual-pore structures that feature supermicroporosity with variable pore parameters. I systematically designed the edge lengths to demonstrate the generality of this strategy. The result demonstrated that the triangular topology with the right choice of the vertices endowed the COFs with dual-pore structure, which could barely be achieved by other topologies. The COFs were unambiguously characterized by various methods and the one-dimensional dual-pore channel and unique trigonal topology were clearly demonstrated.

In chapter 3, I explored these trigonal dual-pore COFs as exclusive adsorbent for bulky neutral molecular mixtures. Coumarin 6 (C6), Nile Red (NR), and 7-(diethylamino)-3-phenylcoumarin (DAPC) are typical natural laser dyes with very similar skeleton structures. They are π -conjugated planar molecules and vary only on dimension. The pore sizes of HTP-BDA COF are 12.7 and 15.6 Å; the big pore is smaller than the dimension of C6 (16.8 Å) or of the same size of DAPC (15.5 Å) but

bigger than that of NR (15.0 Å). The COF achieved an exclusive discrimination at sub-angstrom level by including NR with size of 15.0 Å into the 15.6 Å triangular channels but excluding C6 and DAPC with size of 16.8 Å and 15.5 Å, respectively. The size exclusive adsorption behavior was confirmed by single compound adsorption experiment and energy calculation; the guest molecule accommodation within COF channels was confirmed by gas sorption measurements. These results demonstrated that COFs offer a predesignable platform for molecular discrimination, especially large and neutral molecules that are difficult to be accurately separated by other porous materials.

In chapter 4, I developed mesoporous materials as a novel porous media for iodine removal. I demonstrated the exceptional capture of iodine with crystalline mesoporous COFs. The COFs are designed to have stable imine-linked skeletons, hold mesopores and exhibit large pore volumes of 1.0 and 1.3 cm³ g⁻¹. Notably, the mesopores are entirely accessible to iodine, leading to a full accommodation of iodine within the nanochannels. Consequently, the COFs exhibit exceptional capacity as high as 6.26 g g⁻¹, which is far superior to the state-of-the-art microporous materials. Moreover, the COFs enable rapid uptake of iodine with a rate constant of one order of magnitude higher than those of microporous materials as a result of facilitated diffusion in the one-dimensional mesopores.

In chapter 5, I designed and synthesized ionic crystalline porous COFs with positively charged walls that enable the creation of well aligned yet spatially confined ionic interface. The unconventional reversed AA-stacking mode alternately orientates the cationic centers to both sides of the walls; the ionic interface endows COFs with unusual electric functions. Because all of the walls are decorated with electric dipoles, the uptake of CO₂ is enhanced by three fold compared to the neutral analogue. By virtue of sufficient open space between cations, the ionic interface exhibits exceptional accessibility, efficiency and selectivity in ion exchange to trap anionic pollutants. These findings suggest that construction of ionic interface of COFs offer a new way to the structural and functional designs.

Basing on the three-year work, the author unambiguously demonstrates the designable platform of COFs as versatile separation adsorbent materials. The COF design principle involves pore topology design, pore size control and channel surface modification. The pore size of the separating COFs ranges from micropore to mesopore. The deliberate molecule level design strategy demonstrates the versatile separation capability of COFs targeting not only to small gas and vapor molecules but also to bulky neutral organic dyes and ionic pollutants. The instinct chemical stability endows COFs ability to complete separation in various harsh conditions including oxidative vapor, organic solution and aqueous solution. The investigation results displayed in this thesis demonstrate COFs a new chemical platform as designable adsorptive separation media.

List of Publications

Papers

1. Ionic Covalent Organic Frameworks: Design of Charged Interface Aligned on 1D Channel Walls and Its Unusual Electric Functions, Ning Huang⁺, **Ping Wang**⁺, Matthew A. Addicoat, Thomas Heine, and Donglin Jiang, *Angew. Chem. Int. Ed.* **56**, 4982 (2017). [+], the authors contributed equally to this work.
2. Covalent Organic Frameworks: A Materials Platform for Structural and Functional Designs, Ning Huang, **Ping Wang**, and Donglin Jiang, *Nat. Rev. Mater.* **1**, 16068 (2016).
3. Exceptional Iodine Capture in Stable, Crystalline, Mesoporous Covalent Organic Frameworks, **Ping Wang**, Qing Xu, Qihong Chen, and Donglin Jiang. *Submitted*.
4. Sub-angstrom Molecular Discrimination in Crystalline Microporous Covalent Organic Frameworks, **Ping Wang**, Sasanka Dalapati, Matthew A. Addicoat, Thomas Heine, Qihong Chen and Donglin Jiang. *Submitted*.

Presentation in Conference

1. The 66th SPSJ Annual Meeting, May 2017, Chiba, Japan. “ Sub-angstrom Molecular Discrimination in Covalent Organic Frameworks” (Oral presentation).
2. The 97th Annual Meeting of CSJ, Mar. 2017, Yokohama, Japan. “ Sub-angstrom Molecular Discrimination in Covalent Organic Frameworks” (Oral presentation).
3. The 96th Annual Meeting of CSJ, Mar. 2016, Kyoto, Japan. “ Design and Synthesis of Dual-pore Triangular Covalent Organic Frameworks” (Oral presentations).
4. 2015 International Chemical Congress of Pacific Basin Societies [Pacifichem 2015], Dec. 2015, Hawaii, USA. Design and Synthesis of Triangular Covalent Organic Frameworks” (Poster presentation).

Acknowledgements

I wrote my thesis with a big thankful heart. During the past three years at Institute for Molecular Science and SOKENDAI, I received countless amounts of help and support from many people.

Firstly, I would like to show my appreciation to my supervisor, Prof. Donglin Jiang. Three years ago, I came to IMS as a student with little organic synthesis experience. The research project was really a huge challenge for me and I even lost the courage to start the research. At that time, Professor Jiang offered me plenty advice for both experiment and literature study. He even guided me to conduct organic synthesis though he was extremely busy with the academic research and laboratory management. Now as a Ph.D. candidate who is skillful at common organic synthesis and the confidence to conduct academic research independently, I have to show my acknowledgment to my supervisor for the training, the encouragement and the patience.

I also want to show my gratitude to Prof. Shigetoshi Aono. At April 2016, I moved to JAIST as special research student following Prof. Jiang to continue my PhD study. During this period, Prof. Aono patiently helped me with all the complicated issues required by two universities so that I can fully focused on my research work. In the doctoral thesis and defense process, Prof. Aono gave me a lot valuable instruction and advice. Without his kind help, it is impossible for me to finish my research work on time and come to the final defense.

The research work presented in this thesis would not been well completed without the collaboration, introduction and help from experts from various fields. Our group collaborates very closely with Prof. Thomas Heine and his team of Leipzig University. It is their excellent work that helps me to uncover the exact crystal structure of my COFs. Dr. Ning Huang and Dr. Sasanka Dalapati in our group contributed significantly to my research work on the aspects of organic synthesis and structural analysis. I really appreciate for their patient help and expert introduction. I also would like to show my respect to all the staff from the Instrument Center in IMS

for their kind helps in PXRD, FE-SEM, HR-TEM, EA and NMR measurements.

Finally, I prefer to show my thanks to my labmates Dr. Cheng Gu, Dr. Hong Xu, Dr. Yang Wu, Dr Jia Gao, Dr. Enquan Jin, Ms. Shanshan Tao, Mr. Lipeng Zhai, Mr. Qing Xu and our secretary Mrs. Sayuri Suzuki, who gave me their help and encouragements in not only research but also daily life.

Ping Wang

June 20, 2017